Impact of Neutral Backfill on Plasma Sheet Dynamics in Pulsed Inductive Thrusters

Gordon I. McCulloh

A thesis
submitted in partial fulfillment of the
requirements for the degree of

MASTER OF SCIENCE IN AERONAUTICS & ASTRONAUTICS

University of Washington

2022

Reading Committee:

Justin Little, Chair

Uri Shumlak

Program Authorized to Offer Degree:
College of Engineering,
William E. Boeing Department of Aeronautics and Astronautics

The views expressed in this thesis are those of the author and do not reflect the official policy or position of the United States Space Force, Air Force, Department of Defense, or U.S. Government.

University of Washington

Abstract

Impact of Neutral Backfill on Plasma Sheet Dynamics
in Pulsed Inductive Thrusters

Gordon I. McCulloh

Chair of the Supervisory Committee:
Assistant Professor Justin Little
Aeronautics & Astronautics

The time-dependent effects of operating a pulsed inductive thruster (PIT) in a finite neutral backfill are investigated analytically and experimentally. In principle, a PIT could offer an efficient, in-space propulsion alternative without the lifetime-limiting use of electrodes. However, its traditional design has relied on MW-class power regimes to reach competitive performances. Recent advancements in electrical switching mechanisms have enabled higher pulse frequencies in the range of $1 - 10$ kHz at lower discharge energies. Operation at these rates has been hypothesized to allow for efficient, quasi-steady operation while also improving reliability. A theoretical model was developed to capture how non-equilibrium ionization processes influence plasma formation and acceleration while including neutral entrainment via charge-exchange (CX) collisions and finite skin depth. An inter-pulse evolution of neutral density was also derived to model PIT operation across multiple pulses and allow for comparisons between different ambient conditions. It was determined that testing in a backfill yielded similar time-evolved state properties to steady-state operation with constant gas injection, but with substantial differences in sheet velocity, energy partitioning, and CX collision frequency. Benchtop backfill testing of a prototype unit yielded visual confirmation of predicted dynamic trends in the plasma exhaust and demonstrated the formation of secondary current sheets using steady gas injection.

TABLE OF CONTENTS

LIST OF FIGURES

LIST OF TABLES

LIST OF SYMBOLS

A_s current sheet area (m^2)

$\mathbf{B}$ magnetic field (T)

C_0 circuit capacitance (C)

$c_{s,f}$ fast-moving neutral sound speed (m/s)

$c_{s,n}$ slow-moving neutral sound speed (m/s)

D_a atomic weight (amu)

D_n neutral diffusivity coefficient (m^2/s)

D_p ambipolar plasma diffusivity coefficient (m^2/s)

$\mathbf{E}$ electric field (V/m)

E_0 initial circuit energy (J)

E_{cap} instantaneous capacitor energy (J)

E_f ionization energy of pre-ionized plasma (eV)

E_h energy deposited by Ohmic heating (J)

E_{ind} instantaneous inductor energy (J)

E_{ion} energy required to ionize the mass bit (J)

E_{ke} total current sheet kinetic energy (J)

E_{pi} initial energy of pre-ionized plasma (J)

e_c elementary charge (C)

f_c collisional forces on the plasma per unit area per unit atomic mass (s^{-2})

f_{rep} pulse repetition rate (s^{-1})

g_0 gravitational constant (m/s^2)

H Heaviside step function

I_{bit} impulse bit ($N \cdot s$)

I_c circuit current (A)

I_p plasma current (A)

I_{sp} specific impulse (s)

$\mathbf{J}$ current density (A/m^2)

k plasma coupling coefficient

k_B Boltzmann constant (J/K)

L_0 stray inductance (H)

L_c acceleration coil inductance (H)

L_{eff} effective circuit inductance (H)

M mutual inductance (H)

m_{bit} mass bit (kg)

m_e electron mass (kg)

m_i ion mass (kg)

n_{bf} backflow neutral particle number density (m^{-3})

n_f fast-moving neutral particle number density (m^{-3})

n_n slow-moving neutral particle number density (m^{-3})

$n_{n,0}$ characteristic ambient neutral particle number density (m^{-3})

$n_{n,inj}$ injected neutral particle number density (m^{-3})

N_p number of pulses

n_s current sheet number density (m^{-3})

P_0 ambient pressure (Torr)

P_{ei} power transferred from electrons to ions via Coulomb collisions (eV/s)

P_{inel} power lost to inelastic collisions (eV/s)

P_{ohm} power gained through Ohmic heating (eV/s)

q_s dynamic current sheet pressure (Torr)

R_c circuit resistance (Ω)

R_p plasma resistance (Ω)

r_i inner coil radius (m)

r_o outer coil radius (m)

S_{es} electron-neutral scattering reaction rate (m^3/s)

S_{ex} electron-neutral excitation reaction rate (m^3/s)

S_{ion} electron-impact ionization reaction rate (m^3/s)

T_e electron temperature (eV)

T_i ion temperature (eV)

T_n neutral gas temperature (eV)

t_{max} final simulation time (s)

t_{rep} pulse repetition period (s)

$\bar{u}_e$ average exhaust speed (m/s)

V_0 initial circuit voltage (V)

v_f fast-moving neutral velocity (m/s)

v_s current sheet velocity (m/s)

Δv_{sf} velocity difference between the current sheet and fast neutral population (m/s)

$v_{th,n}$ slow-moving neutral thermal velocity (m/s)

w_s current sheet width (m)

z_a coil offset from gas injection plane (m)

z_c lumped mutual coupling distance (m)

z_{max} maximum simulation boundary (m)

z_n characteristic ambient neutral length scale (m)

z_s current sheet position (m)

α dynamic impedance parameter

γ polytropic index

δ_s plasma skin depth (m)

ε_0 permittivity of free space (F/m)

ε_{ex} first excitation potential (eV)

ε^*_{ion} effective ionization energy (eV)

ε_{ion} first ionization potential (eV)

η_e electrical efficiency

η_m mass utilization efficiency

η_p classical plasma resistivity ($\Omega \cdot$ m)

η_R recapture efficiency

η_T thrust efficiency

Θ_e electromagnetic transparency of the current sheet

$\Theta_{m,cx}$ charge-exchange mass transparency of the current sheet

$\Theta_{m,ion}$ ionization mass transparency of the current sheet

$\ln(\Lambda)$ Coulomb logarithm

λ_{cx} charge-exchange mean free path (m)

μ_0 permeability of free space (H/m)

ν_{ei} electron-ion collision frequency (s^{-1})

ν_{en} electron-neutral collision frequency (s^{-1})

ρ_0 linear mass density distribution (kg/m^3)

σ_{cx} charge-exchange cross section (m^2)

σ_{en} electron-neutral cross section (m^2)

σ_{qm} ion-neutral momentum transfer cross section (m^2)

τ_{dc} decoupling time of the current sheet (s)

τ_{LC} LC-period of the circuit (s)

χ_0 ionization fraction driven by pre-ionization

ψ_1, ψ_2 critical resistance ratios

ω angular frequency of incident electromagnetic field (s^{-1})

Ω current sheet formation parameter

COMMON ACRONYMS

AC/DC: alternating/direct current

BC/IC: boundary/initial condition

CX: charge exchange

EM: electromagnetic

EP: electric propulsion

FARAD: Faraday accelerator with radio-frequency assisted discharge

HiPeR-PIT: high-pulse-rate pulsed inductive thruster

ICCD: intensified charge-coupled device

IPPT: inductive pulsed plasma thruster

MHD: magnetohydrodynamic

ODE/PDE: ordinary/partial differential equation

PI: pre-ionization

PIT: pulsed inductive thruster

PPU: power processing unit

RF: radio frequency

ACKNOWLEDGMENTS

First and foremost, I would like to acknowledge my advisor, Professor Justin Little. Thank you for taking me onto a project in the midst of the pandemic and for finding an interesting line of research despite newfound barriers. Your guidance in this work and careful, clear instruction of plasma physics has led me to a better understanding of both engineering and first principles. This thesis is entirely a product of your assistance and love of plasmas.

I would also like to thank the Space Force and the University of Washington for sponsoring my degree and allowing me to pursue an education in such a wonderful place. I look forward to applying my skillset in the defense and exploration of the space domain. Dr. Helen Meisenhelder of the U.S. Air Force Academy is deserving of special acknowledgement for her guidance and effort in clearing a path toward graduate studies.

I have been fortunate to have shared my time at UW with a great group of labmates. To Peter, thank you for sharing your technical expertise intermixed with German beer, Belizean hot sauces, and beautiful skiing lines. To Charlie, thank you for reaching out first and for encouraging me to find a greater variety of work. To Anna and Bennett, thank you for sharing in my quirky parallel study of dinosaurs. To Landon, Reed, Sari, and Tim, thank you all for walking through the same valley of the shadow of plasma coursework from the start, and for helping me understand a whacky state of matter. As for my project partners, Curtis, Arvindh, and Cameron, you have my heart-felt thanks for advancing what I find to be a fun experiment. To Curtis, in particular, thank you for your patient mentorship in the essence of engineering through your reasoned diagnoses of problems and solutions.

To all of the teachers who have inspired me to think, thank you for the gift of opportunity. It has been a privilege to grow through the Kennebunk public school system, Maine School of Science and Mathematics, U.S. Air Force Academy, and now the University of Washington. I would like to acknowledge those who ever wrote a letter of recommendation on my behalf. As for this degree, thank you to Colonel Luke Sauter and Professor Paul Vergez.

There are also those who deserve tremendous gratitude who I have never met before, but enabled this project and the results of this thesis years ahead of my time. To Lee Dailey, Ralph Lovberg, Kurt Polzin, Adam Martin, and everyone else who has offered a single insight into the operation of pulsed inductive thrusters, you have my utmost respect as developers of a technology that may one day have a curious footnote in the mosaic of human knowledge.

Last but not least, this thesis would not have been possible without the continued support of my family and friends. To my parents, Jeff and Heather, thank you for endowing me with confidence, diligence, and all of the tools for flourishing. My sister, Charlotte, and I are still discovering how lucky we truly have been.

DEDICATION

To my grandparents: Nancy, Mary, and the Pauls. You have been a source of professional inspiration, love, and support all my life.

Chapter 1
INTRODUCTION

The guiding incentive for the use of electric thrusters in spacecraft propulsion is efficiency of motion across great distances or stretches of time, not limited by the impulsive phase of liftoff. Savings in propellant mass balanced by rapid exhaust velocities allow for higher fractions of valuable payload and the exploration of novel mission trajectories. In addition to satellite station-keeping, attitude control, and orbital maneuvering, the future of in-space propulsion doubtlessly calls for better means of sending both man and machine further and faster into the outer reaches of the solar system.

Electric propulsion (EP) systems are primarily limited by three tradeoffs: (1) low thrust, and hence less immediate changes in orbit; (2) long durations required to reach a desired velocity; and (3) a power processing unit (PPU) mass penalty. It is therefore sensible to maximize the system lifespan and reliability of an electric thruster to best exploit its technological utility over conventional chemical propulsion systems for its many use-cases. There are a few novel EP solutions that naturally evade some of the lifetime-limiting mechanisms that challenge mainstream devices with greater flight legacy (e.g. gridded-ion and Hall effect thrusters). This thesis shall look into the physics of operation and laboratory development of one such technology in the inductive pulsed plasma thruster (IPPT).

The IPPT employs an electrodeless design to inductively accelerate sheets of plasma without making physical contact between the fast-moving propellant and the thruster to impart electromagnetic (EM) energy into the exhaust. This largely overcomes the constraint of erosion internal to the system and allows for a broader selection of fuels, but introduces difficulties in tracing the dynamic flow of energy from the PPU to the ejected plasma. A considerable body of work has been put forth in the last half-century to model and test the

efficacy of IPPTs as EP alternatives, but the literature is still thin in the area of facility effects, which aim to characterize the operating differences between propulsion systems in the laboratory setting and those in outer space. The scope of this work is to investigate the facility effect of a finite neutral backfill of propellant gas within the test chamber. We will analyze both numerical simulations and experimental observations for single-pulse dynamics and offer predicted impacts for steady-state operation via the mathematical model.

1.1 Advantages of Unsteady Electromagnetic Acceleration

Although steady-acceleration EP offers stability and simplicity from a design perspective, certain characteristics of unsteady discharges are attractive to the performance of inductive devices. Namely, there are three main advantages to pulsed modes [1]:

1. Thrust efficiency tends to scale with increasing discharge current density. Pulsing allows for increased transient current density, and thus increased efficiency.

2. Brief and intense pulsed operation overrides some of the physical limitations of accelerating an imperfect plasma which manifest as losses due to kinetic equilibrations (e.g. inelastic collisions and thermal radiation).

3. Unsteady field effects can produce desirable spatial non-uniformities in the discharge pattern, proffering better entrainment of ambient gas.

All thrusters that utilize electromagnetic fields to drive a current through an ionized propellant scale to better efficiencies with increased processed power [2]. Therefore, the energy cost associated with plasma ionization should be kept low relative to total system power. Pulsed operation offers a brute-force engineering appeal by enabling extremely high current levels to form uniform plasma discharges in the two-fluid domain [3]. This places strain on the PPU within the overall system architecture, but efficient formation of a cohesive plasma is paramount to fabricating a competitive electromagnetic accelerator.

Pulsed modes enable operation at high power levels for the modern state-of-the-art in spacecraft power busses. Larger satellites and interplanetary vehicles are presently limited to tens of killowatts, but with a bus compatible capacitor pulsed-power supply (CPPS) a PPU can step up the voltage to the multiple kilovolts required for IPPT functionality. Pulsed plasma thrusters have operated successfully and continuously at 60-70 Joules per pulse in space, taking less than 0.2 kW of input power at 7-13% efficiency [4, 5]. This has been expanded to 4.8 kJ per pulse in the laboratory setting [6] without stringent cubesat power constraints, depicting the ability to process tremendous levels of power with a single thruster element, especially at high pulse repetition rates in steady state.

Indeed, the power of a pulsed device scales directly with pulse rate. One of the primary advantages of IPPTs over steady accelerators, assuming other system parameters remain unchanged, is that constant specific impulse (I_{sp}) and thrust efficiency (η_T) can be achieved over a wide range of input power levels by maintaining a constant discharge energy per unit pulse [7]. Past studies have demonstrated the ability of a dynamically impedance-matched IPPT to operate in a regime of relatively constant η_T over a broad range of attractive I_{sp} values [8, 9]. Performance reliability is advantageous for long burns over extended mission trajectories, and lends more versatile output conditions to spacecraft PPUs.

Broadly speaking, the characterization of specific impulse and thrust efficiency forms the crux of qualifying any in-space propulsion device as a competitive thruster variant. I_{sp} is often thought of as a "gas mileage" metric for a rocket engine, whereas η_T is more meaningful to the investigation of EP specifically as it quantifies the conversion fraction of input power to thrust power. The conventional method of assessing the operating performance of an EP system is to measure the reaction force from the thruster with a mechanical thrust stand mounted inside a vacuum chamber [10]. In any laboratory setting, it is expected that facility effects will have some impact on the measurements gathered by the thrust stand, but reducing chamber pressure approaches the conditions of outer space and decreases the confounding influence of backpressure [11]. This method, in tandem with laser interferometry, has been successfully used to characterize both steady and unsteady EM thrusters [12], but is difficult

to adapt to inductive accelerators without introducing significant noise to the system. For the purposes of this study, we will be estimating performance parameters based on injected fuel mass bit rather than force acting on the thrust stand. The specific impulse (thrust per unit weight flow of propellant) of an IPPT is:

$$I_{sp} = \frac{\bar{u}_e}{g_0} = \frac{I_{bit}}{m_{bit} g_0} \tag{1.1}$$

where $\bar{u}_e$ is the average exhaust velocity of the total injected propellant population per pulse, g_0 is the gravitational acceleration constant of Earth, I_{bit} is the impulse bit or impulse per unit pulse, and m_{bit} is the mass bit. We subsequently define the thrust efficiency of an IPPT as the ratio of directed kinetic energy in the expelled plasma sheet to the initial stored electrical energy in the circuit E_0, given by

$$\eta_T = \frac{m_{bit} \bar{u}_e^2}{2E_0} = \frac{I_{bit}^2}{2 m_{bit} E_0}. \tag{1.2}$$

Interplanetary missions for which moderate- to high-power EP offers the most significant benefits call for an optimum I_{sp} in the range of $4000 - 8000$ seconds [8]. The performance parameters available to pulsed plasma thrusters are low for this regime, but contemporary advancement paths for IPPT technologies show promise in achieving formidable efficiencies using argon, xenon, and ammonia propellants [13]. Inductive acceleration is broadly fuel agnostic, which opens doors to the use of naturally-sourced propellants via in-situ resource utilization (ISRU) such as carbon dioxide from the Martian atmosphere [14].

1.2 Inductive Pulsed Plasma Thrusters

To refine our scope of study from unsteady magnetic accelerators to IPPTs, we must firmly establish the working principles of the latter to ultimately discuss plasma physics and facility effects. As aforementioned, an IPPT functions by charging a capacitor bank to an initial voltage and then rapidly discharging to drive high-current pulses through an inductive coil, thereby generating an opposing current in the plasma. The device generates thrust by ion-

izing a gaseous propellant and inductively accelerating the resulting plasma to high exhaust velocities ($\mathcal{O} \sim 10 - 100$ km/s) via the magnetic component of the Lorentz force [15].

Although there are multiple implementations and design variants with unique aspects to their physics, all IPPTs function through a combination of Ampère's and Faraday's laws with roughly the same operating sequence:

1. Electrical energy is accumulated at a high voltage ($V_0 \sim 1 - 100$ kV) on an external primary circuit with capacitance C_0. Many coil configurations have been tested to determine the best parallel circuitry scheme [16–18], but for the most part these rely on similar energy storage architectures.

2. Propellant is introduced to the face of the thruster coil by some manner of gas injection. The orthodox mechanism for doing so is via a rear-facing nozzle, but inter-coil injection could prove to be superior. The relative merits of both are briefly discussed below in this chapter, and we pursue modeling the latter in this study.

3. The switch connecting the capacitor bank to the inductive coil is closed, driving a high current I_c through the RLC circuit of some coil inductance L_c with initial inductance L_0. Control of L_c and L_0 as well as current rise rate ($dI_c/dt|_{t=0} = V_0/L_c$) is crucial within the study of IPPTs [7].

4. Current flowing azimuthally in the coil generates a radial magnetic field via the relationship in Ampère's law:

$$\nabla \times \mathbf{B} = \mu_0 \mathbf{J} \tag{1.3}$$

for a magnetic field $\mathbf{B} = B_r \hat{r}$, current density $\mathbf{J} = j_\theta \hat{\theta}$, and permeability of free space μ_0. The rapidly-growing magnetic field permeates the gas in close proximity with the coil face.

5. The time-dependent magnetic field $\mathbf{B}$ generates an opposing electric field $\mathbf{E} = -E_\theta \hat{\theta}$ in accordance with Faraday's induction equation:

$$\nabla \times \mathbf{E} = -\frac{\partial \mathbf{B}}{\partial t}. \tag{1.4}$$

6. Breakdown of the neutral gas occurs if the azimuthal electric field is sufficiently strong to overcome some threshold energy, catalyzing a state of high conductivity in the propellant. This logic follows the scaling relation

$$E_\theta \propto \frac{dj_\theta}{dt} \propto \frac{1}{\sqrt{L_c C}} V_0 \sqrt{\frac{C_0}{L_c}} \propto \frac{V_0}{L_c}.$$

   We can express this in terms of energy per pulse, $\frac{1}{2} C_0 V_0^2$,

$$E_\theta \propto \frac{1}{L_c} \sqrt{\frac{2(\frac{1}{2} C_0 V_0^2)}{C_0}}$$

   to depict that propellant breakdown requires large energies and small L_c, C_0.

7. The attempt of the primary magnetic field to penetrate the conducting zone forms a current sheet of plasma near the coil surface. This sheet carries a high current density, opposite but in phase with the primary external coil.

8. It is traditionally posited that the induced current density and radial magnetic field accelerate the current sheet via the Lorentz body force, $\mathbf{J} \times \mathbf{B}$. A more precise explanation of this physical phenomenon is that the counter-rotating currents in the coil and the plasma electromagnetically repel each other to create axial thrust.

9. After the plasma sheet is impulsively driven from the coil, the external circuit must recharge quickly within the pulse period afforded by the operating repetition rate. The switch must open to charge the capacitor.

It should be noted that the interaction between the induced current and the coil current generating it yields the salutary benefit of an IPPT; hence the inductive namesake. Any resistive current driven by the induced azimuthal electric field is 90° out of phase with $\mathbf{B}$, so the $\mathbf{J} \times \mathbf{B}$ force component reverses sign every half cycle of the capacitor ringdown [1].

Fig. 1.1(a) depicts the cross section a planar, open magnetic flux IPPT variant functioning as described by the operating sequence above. The coil produces a concentrated axisymmetric magnetic field in the $r - z$ plane between the thruster and the plasma to axially impel the current sheet. The plasma shown is exhausted at high velocities perpendicular to the coil face according to the Lorentz body force. Fig. 1.1(b) gives a discharge current waveform representative of a standard IPPT, with relative timescales and magnitudes to give context for the rise time required to create a plasma. Current rise time scales with the inductance of the coil, and is therefore an important metric to the performance of an IPPT as we will discuss in later chapters.

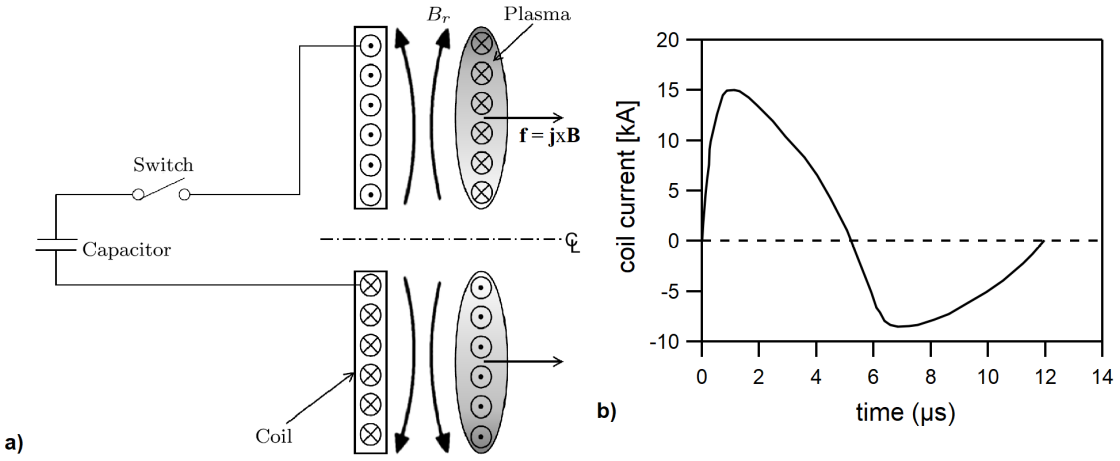

Figure 1.1: (a) Schematic showing the basic operation of a planar IPPT, where the Lorentz body force $\mathbf{f}$ in the axial $(+\hat{z})$ direction arises from the interaction between the azimuthal plasma current density $\mathbf{J} = -j_\theta\hat{\theta}$ and the radial magnetic field $\mathbf{B} = B_r\hat{r}$. (b) Sample discharge current of one of the nine parallel coils of the PIT MkVa (after [13, 19]).

Across the total spectrum of rocket engines, IPPTs offer a fairly novel concept for generating thrust, but they also introduce unique physical difficulties inherent to ionization and acceleration. The inductive approach must overcome several loss mechanisms to achieve high thrust efficiencies. Jahn [1] has highlighted these challenges in his seminal work:

> ... any delay in breakdown of the gas after application of the primary field pulse results in energy being dissipated in the external circuit, which, unlike that of the direct electrode devices, is complete without the gas loop ... Equally troublesome is the need to accomplish all the energy input to the gas before much motion of it has occurred. The current induced in the gas-loop "secondary" depends on its mutual inductance with the external primary, and thus is a strong function of the physical separation between these two current paths.

Indeed, coupling electrical energy from the circuit to the plasma exhaust is a famously tricky engineering and modeling problem in the development of IPPTs. The electrodynamic coupling between the two elements of the lumped system dissipates quickly as the current sheet propagates from the coil face, so the pulse must deliver a great amount of electromagnetic work quickly to the propellant in order to generate any sizeable reaction force. The inductance of the circuit increases as a function of time once the switch is closed, which is representative of the amount of work that the RLC circuit is capable of transferring into the plasma. Efficient acceleration is only possible when the coil inductance L_c, defined here as the amount by which the circuit inductance increases for a given pulse, greatly exceeds the initial inductance L_0 (also referred to as stray or parasitic inductance, attributable to circuit imperfections). That is, their ratio must greatly exceed unity ($L_c/L_0 \gg 1$) in order to create a profitable plasma sheet.

A few engineering solutions exist to overcome these inherent challenges which could prove to be technology-enabling improvements to thrust efficiency. As Jahn [1] has pointed out, energy dissipation caused by a delay in gas breakdown at the beginning of a pulse "might be relieved by providing a separate pre-ionization mechanism or by operation at a sufficiently

rapid repetition rate." The idea behind pre-ionizing the injected propellant would be to form a plasma prior to the rapid increase in coil current, bypassing the brief timescale required to break down the neutral gas and allowing for greater work transfer at the beginning of a pulse. This mechanism has been tested for many pulsed inductive devices across space propulsion and nuclear fusion applications. Pre-ionization (PI) has been most commonly implemented to create a radio-frequency (RF) plasma [20–23], send an initial lower-energy pulse through the inductive coil [24–27], and strike a glow discharge between two electrodes in [28–30]. The experimental work in this thesis will utilize RF PI, which somewhat limits the comparisons drawn between results and legacy data.

The pulse repetition rate is also a key feature of this study, particularly with respect to performance in ambient fill conditions. Faster pulsing shortens the timespan over which the neutral gas is able to diffuse away from the coil plane for an inter-coil injection scheme, but places challenging erosion demands on the switches within the primary circuit. This is an ongoing area of IPPT development that takes place in parallel with this research, but is not the focus of this project.

1.3 Review of Previous Work

Research and development of the IPPT has occurred in intermittent bursts since the early 1960s, beginning with a substantial portfolio of work from Dailey and Lovberg of TRW Space Systems (later acquired by Northrop Grumman Corporation) [15]. Their efforts compiled studies of plasma physics [20, 31–35], electrical hardware [36], and the performance of large-diameter prototypes [8,9,16,18,37]. In recent years, the IPPT has been primarily advanced by researchers at NASA-Marshall, American universities, and Chinese defense agencies. Below, we discuss the relevant background to the investigation of finite neutral backfill effects and further limit the scope of the thesis.

1.3.1 Planar Thrusters

IPPTs encompass many design variants of both open and closed magnetic flux modes. It was originally thought that a conical inductive coil angled radially inward would contain and vector the ejected plasma more efficiently along the axial centerline of the device, giving rise to the conical theta-pinch (CTP) thruster. Hallock *et al.* [2, 38] performed proof-of-concept testing at several cone angles to investigate the effect of coil geometry on CTP performance, but Martin [39] has since used a magnetic field solver to predict that a cone angle of 90° (i.e. a planar design) would give the highest theoretical thrust efficiency. The engineering and modeling of a flat coil as depicted by Fig. 1.1(a) is much simpler because current sheet action can be generalized to the axial direction, so we henceforth limit our study to the planar IPPT, also known as the pulsed inductive thruster (PIT).

Early prototyping by Dailey and Lovberg iterated through seven base designs of varying circuitry and coil geometry, designated by MkI through MkVII symbols in order of construction. These systems have yielded several robust test campaigns in the 15-24 kV range, using short electrical discharge timescales to compensate for relatively slow propellant fill mechanisms. The issue of gas injection was addressed by installing a conical pylon structure along the centerline of the thruster. Fig. 1.2 depicts the rear-facing nozzle in series with a magnetic pulsed valve as it injects neutral gas toward the coil face where it spreads radially outward in between pulses to give a quasi-uniform propellant distribution. This scheme, of course, physically obstructs the downstream ejection of the plasma exhaust and is only marginally effective for slower pulse repetition rates. Even so, rear-facing gas injection was maintained across all early PIT variants as well as many later designs such as the Faraday accelerator with radio-frequency assisted discharge (FARAD) [22, 23, 40].

The prevailing opinion in PIT development until recently has been that the technology is only suited for the high-power regime subject to larger geometries. This is because the distance over which the drive coil electromagnetically couples with the plasma is a fixed first-order fraction of the overall coil diameter (assuming an annular disk) [13]. Improved

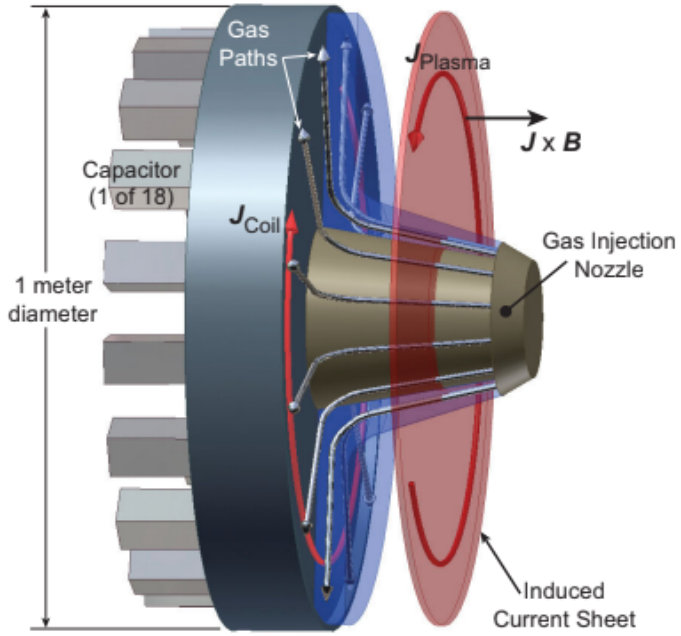

Figure 1.2: Schematic of the downstream injection mechanism in the original PIT design and subsequent FARAD prototypes (from [23]).

coupling proffers greater inductive energy transfer and better efficiencies. Hence, Dailey and Lovberg were motivated to expand from 20-30 cm outer diameters [16, 20] to sizeable multi-turn coils of 1 meter [8, 37]. Propulsion systems of this scale, however, would heavily tax the mass budget of a spacecraft, so small, low-power variants are attractive. This is especially true within the evolutionary outlook of PIT testing since thrusters operating in the 100s of kW or MW regimes, pumping considerable gas loads to lower pressures in larger chambers, would place significant strain on research facilities.

To this end, pre-ionization and faster pulsing have become pivotal to PIT advancement. Early findings on the 30 cm thruster variant demonstrated that sending an independent, low-energy current pulse through the acceleration coil prior to a main discharge was an inefficient means of PI because it impelled the gas beyond the coupling region before the majority of work could be transferred [20]. More promising methods for increasing the primary discharge

ionization rate have been implemented, like that of the FARAD device, which employed a helicon/RF antenna to ionize the injected gas before directing it to the coil face with an applied radial magnetic field [22]. The FARAD proof-of-concept showed that PI could lessen the main discharge energy threshold for propellant breakdown [23,40], lightening demands on the system PPU. Even more recently, a low jet power ($P_{jet} \sim 1-5$ kW) 27 cm PIT was built to test pulsed gas valves and solid-state switches on a small-scale integrated architecture [41].

Formidable progress has been made in the theoretical modeling of PIT operation as well. Simplified one-dimensional (1D) formulations that aim to condense plasma sheet dynamics in the axial $\hat{z}$-direction offer enticing means for predicting system performance trends without the computational burden of two- (2D) and three-dimensional (3D) magnetohydrodynamic (MHD) simulations. Early 1D models coupled a set of circuit equations with a plasma momentum equation to numerically solve for I_{sp} and η_T using controllable input variables [8, 37]. However, these efforts were severely limited because they assumed constant plasma temperature, divorcing the physics and state properties from a temporal description of sheet energy. Adjustments to the original model have since captured more information and better approximated experimental data for different propellants and configurations by incorporating electrodynamic coupling [42] and evolving plasma pressure [43]. Emphasis has also been laid on the nondimensionalization of state variables to define scaling parameters that elucidate loss mechanisms in the system on shorter timescales [2, 7, 23, 39].

Each of these projects have elevated the planar family of IPPTs by working toward a feasible EP solution and bolstering the basic understanding of energy flow and partitioning within such an engine. The literature is extensive on the evolution of research and development since the 1960s, but we attempt to summarize the major insights below [15, 23]:

- PIT performance is generally maximized when a uniform current sheet is produced, resulting from a high current rise rate (i.e. high V_0, low L_c) and even gas density distribution over the coil face. Scaling up $dI_c/dt|_{t=0}$ favors higher power regimes.

- The current in the inductive plasma is primarily conducted by electrons.

- Increasing the ratio L_c/L_0, known as the Lovberg criteria, increases η_T. This improves the specific power of the overall system.

- For an in-space mission, the switches and capacitors in the primary circuit would need to provide $10^9 - 10^{11}$ pulses at $1 - 100$ Hz over the lifetime of the thruster [13]. This estimate, compounded with the high bank voltages and discharge currents required for unsteady acceleration, could transfer the active constraint to the spacecraft PPU and nullify the electrodeless advantage of IPPT function.

- Larger diameter drive coils lengthen the EM coupling distance between the circuit and the plasma armature and are therefore capable of imparting more work to greater amounts of gas in a traditional PIT configuration. This may not necessarily improve the electrical efficiency of the thruster, and levies a programmatic hurdle for smaller test facilities.

- PIT performance was maximized on the MkI, MkV, and MkVa prototypes when operating on NH_3 propellant, but Ar, Xe, and N_2H_4 fuels also yield high efficiencies. Variance between propellants is attributable to complex, microscopic energy modes involved in the breakdown and ionization of gases. It is thought that NH_3 is particularly potent due to the lack of a significant radiation energy sink.

- A weak antecedent pulse through the inductive coil is a poor means of pre-ionization if there is any sizeable time delay ahead of the main discharge. We note that this finding is still under present consideration.

- The nondimensionalization of modeling parameters can be a valuable method for uncovering obscure plasma processes that have notable consequences for system performance. We can optimize operating conditions by examining numerical trends, such as by aligning the acceleration and circuit response timescales to maximize η_T [44].

1.3.2 State-of-the-Art

The current state-of-the-art in PIT performance was demonstrated on the MkV (4.5 μF bank capacitance) and MkVa (9 μF bank capacitance) variants during a two-year test campaign from 1991 to 1993 [15]. These experiments have published a majority of data on single-pulse operation for an assortment of fuels, to include: He, CO_2, Ar, Xe, NH_3, and simulated hydrazine ($N_2 + 4NH_3$) [9]. The MkVa gave particularly impressive specific impulses ($\mathcal{O} \sim 2000 - 8000$ s) and thrust efficiencies ($\mathcal{O} \sim 30 - 55\%$) for higher specific energies, E_0/m_{bit} ($\mathcal{O} \sim 1 - 5$ kJ/mg) [8]. The performance boost from the MkV to the MkVa was attributed to higher dI_c/dt, as alluded to in the previous section. Fig. 1.3(a) shows the PIT MkV outside the test chamber with capacitors installed on the back for a full sense of system scale. The follow-on MkVI variant pictured in Fig. 1.3(b) used the same Marx-generator coil topology as its predecessor, but instead of Litz wire, the coil was engineered with hollow copper tubing to enable active cooling during high-pulse-rate operation [45]. A fault in one of the spark-gap triggers was discovered post-testing, which may have led to the decreased efficiency measurements observed for similar mass bits and charging voltages.

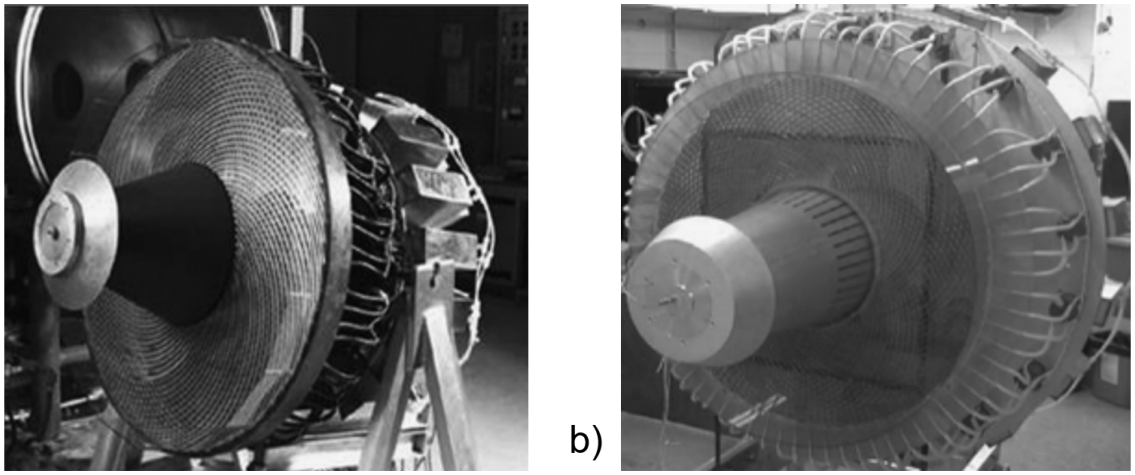

Figure 1.3: (a) Photograph of the PIT MkV prototype with rear-facing gas injection scheme (from [9]). (b) MkVI counterpart with longer pylon and copper coil material (from [46]).

Other programs and findings at the cutting-edge of PIT development are worth mentioning to contextualize the methods and parameter spaces used in this thesis. Northrup Grumman Space Technology's Nuclear-Electric PIT (NuPIT) [47] has been building attention as a high-energy follow-on to the TRW series of prototypes, but more concerted effort has been directed to lower discharge voltage concepts [41] and high-pulse-rate PPUs [45, 48]. Coupling distances reported in literature [7, 42] have indicated that the required pulse rate for competitive alternatives is expected to be on the order of $1 - 10$ kHz using noble gas propellants. Simulations have predicted that higher pulse rates could yield efficiencies in excess of 60% when operating in an inductive recapture mode [39]. This would entail shutting off the primary switch one half-cycle after capacitor ringdown when I_c crosses zero, latching the capacitor with a non-zero voltage to save energy. We examine the effects of recapture on high-pulse-rate designs in our modeling efforts.

1.3.3 Facility Effect Studies

The primary undertaking of this thesis is to explore dynamic effects on PIT operation due to the inevitable presence of ambient neutral gas pressure in terrestrial vacuums. To date, significantly larger bodies of test data and analysis exist for EP devices with flight validation, such as the Hall effect thruster (HET). Two major consequences of ground testing have demonstrated differences in HET performance between the chamber and flight environments: the grounded chamber walls [49] and the finite background pressure [11]. The physical mechanisms underpinning the latter are poorly understood, but have definitive effects on thrust efficiency, including: neutral ingestion, stability, cathode coupling, and divergence angle [50]. Most of these do not apply to our research given the dissimilarities between IPPTs and HETs, but neutral ingestion (or entrainment) is a key process for propellant mass utilization during current sheet formation and acceleration. The stability of a PIT plasma is also critical as it affects inductive coupling and magnetic permeability [13]. Thus, the validity of experimental comparisons made between data sets taken in different facilities with varying vacuum pressures, especially at 10^{-4} Torr and higher, is suspect [51].

Dailey and Lovberg have previously investigated possible facility effects on their PIT variants, predicting that a backpressure could add mass to the coil insulator surface that would be desorbed by a discharge, and a gas layer ejected from the end of the test chamber might impart momentum to the thruster [8]. Regression analysis of raw input data from the MkV 16 kV ammonia test campaign indicated that neither effect introduced substantial error to mass bit or impulse measurements at a 0.2 micron base vacuum. However, these findings were contingent on a large-diameter PIT setup, and they captured only a narrow portion of neutral interactions. We aim to model the time-evolution of cumulative entrainment per pulse as well as energy and momentum transfer in the plasma exhaust.

We note, for the sake of completeness, that Polzin and Reneau [52] have modeled the facility effect of conductive walls on PIT performance for varying chamber dimensions. Grounded, conductive chamber walls have a unique interaction with HETs because they impact cathode coupling with the plasma plume [49], but the same is not true for electrodeless IPPTs. Instead, the magnetic field of the acceleration coil will interact with the conductive walls as well as the injected neutral gas, reducing the overall amount of EM work imparted to the plasma. Polzin and Reneau employed a magnetostatic solver to simulate different field configurations for varying chamber wall positions, and found that lower radii compressed the magnetic field lines from the coil, thereby reducing the current sheet flux surface and subsequent coil inductance [52]. Extending their model to space conditions predicted relative increases in I_{sp} and η_T of 4% and 7.5%, respectively. Fig. 1.4 visualizes their magnetostatic model as the current sheet propagates away from the coil, showing different levels of field compression. We study the facility effects of varying static fill pressures to illuminate similar gaps for a wide range of laboratory capabilities.

1.4 Project Motivation

PIT research is still in the relatively early stages of technological readiness, but could offer an enduring electric approach to spacecraft propulsion across multiple power regimes. The advancement of low-power designs is critical to the ultimate development of a competitive ac-

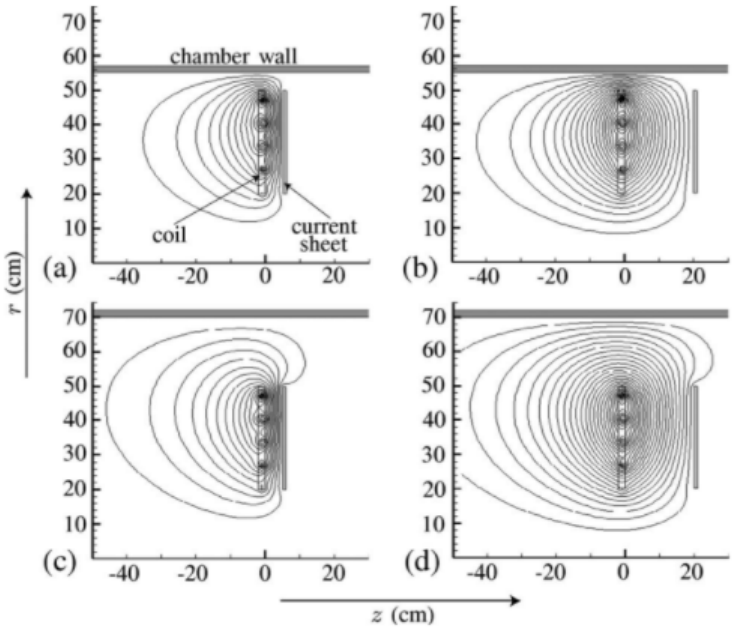

Figure 1.4: Magnetic flux contours simulating the effect of conductive test chamber walls on PIT operation for varying current sheet axial positions and wall radii (from [52]).

celerator, requiring continual examination of optimal operating conditions and current sheet phenomena. Most laboratory facilities in the world can only manage base vacuum pressures six orders of magnitude higher than those in low-earth orbit (LEO) [50], so for all programs, neutral backfill represents a significant and inescapable effect on the inductive acceleration of a plasma. We look to characterize the magnitude and mechanisms of inaccuracy introduced by the ground environment to explain performance gaps at critical timescales.

1.4.1 Theoretical Modeling

The understanding of first principles precludes applied engineering progress. Computationally inexpensive modeling techniques [7, 8, 27, 37, 42–44] and higher-dimensional MHD or magnetic field solvers [39, 53–57] have explicated plasma dynamics and scaling trends for numerous PIT designs to guide our work. The use of a numeral simulation to quickly iterate

through different chamber pressures and neutral distributions is imperative to our project. Furthermore, expanding previous models to account for propellant mass entrainment under non-equilibrium conditions is required for meaningful results in our endeavor, as any simplification thereof would bar the impact of our study. Our model accounts for key physics and requirements of current sheet formation while scaling to lower discharge energies per pulse to delineate between the acceleration phase with higher fidelity. We will emphasize the influence of fundamental plasma dynamics throughout our analysis to uncover facility effects in both efficient and inefficient regimes of thrust production.

1.4.2 High-Pulse-Rate Pulsed Inductive Thruster (HiPeR-PIT)

Previous PIT test articles have operated at nominal pulse rates between 1 and 100 Hz [13] using rapid pulse valves to prevent the escape of unaccelerated gas between coil discharges. It has been hypothesized, however, that high mass utilization can be achieved for the coupling distances found in literature with steady-state, inter-coil propellant injection [15]. This would potentially eliminate the pulse valve from the gas injection mechanism, which could simplify the system while bolstering reliability and extending lifetime. As we previously noted, steady-state injection would require much higher pulse rates, thereby taxing the spacecraft PPU. Downsizing to lower discharge energies per pulse would permit the transition from conventional switches (e.g. spark gap, thyratrons) to solid-state relays such as thyristors, silicon controlled rectifiers (SCRs), metal oxide semiconductor field effect transistors (MOSFETs), and insulated gate bipolar transistors (IGBTs). The University of Washington (UW) is researching a design using modern power electronics known as the high-pulse-rate pulsed inductive thruster (HiPeR-PIT) [48], which is the test platform found in this thesis.

The HiPeR-PIT employs a brassboard-fidelity PPU prototype with a steady-state injection scheme to reach nominal pulse rates of $1-10$ kHz in the multi-kW power class. It utilizes a two-step pre-ionization approach with central RF power and an antecedent pulse from a smaller capacitor bank, triggered only one to two cycles before the primary discharge. In this thesis, we attempt to model conditions available to the HiPeR-PIT in the single-pulse and

steady-state modes to identify system characteristics that drive better performance regimes. Smaller, low-discharge-energy IPPTs are especially susceptible to facility effects due to their reliance on efficient mass utilization. Therefore, the impact of this work shall be twofold: firstly, we explore the influence of finite neutral backfill on current sheet dynamics to evaluate general PIT function, and secondly, we mature the HiPeR-PIT concept by approximating physical processes relevant to lower pulse energies and shorter timescales.

1.5 Thesis Outline

We provide more rigorous theoretical modeling efforts and analyses upfront, followed by approximations produced by the HiPeR-PIT experiment as supplementary work. In the next chapter, the bulk of our 1D IPPT model is formulated in detail alongside previous simulation methods to highlight our departure from previous ideas. A method for extending the single-pulse thruster dynamics to steady-state operation is presented in Chapter 3. The predictions for ambient backfill and nominal in-space environments are compared and analyzed in Chapter 4, and an intermediate backflow condition is proposed in Chapter 5. The HiPeR-PIT setup and diagnostics employed to gather plasma sheet data at varying chamber conditions are described in Chapter 6. A summary of processing techniques and preliminary findings is found in Chapter 7 for the purpose of corroborating scaling trends in the single-pulse model for argon. Finally, we conclude with a comparison of theoretical and experimental analyses and offer possible error modes with the intent to demonstrate the future utility of testing high-pulse-rate PIT designs in a backfill.

Chapter 2

ONE-DIMENSIONAL MODEL OF SINGLE-PULSE CURRENT SHEET DYNAMICS

We expand the lumped-element circuit equations commonly used to analyze IPPT state and performance [8] to a one-dimensional model of pulsed inductive thruster sheet formation and acceleration that accounts for neutral gas entrainment via charge-exchange (CX) collisions and ionization reactions. It adds information to examine the latter under non-equilibrium conditions, and develops a description of plasma transparency to electromagnetic fields to explore the relationships between sheet permeability and propellant mass utilization. Dimensionless scaling parameters from previous works pair with our data to explicate transient behaviors that either enable or detract from profitable sheet formation.

The purpose of our model within the broader scope of IPPT research is to include the necessary physics for capturing more information about electromagnetic coupling, plasma resistivity, and particle interactions across the early evolution of a pulse. By examining sheet formation, ionization, and acceleration at microsecond timescales, a 1D model offers tremendous utility in locating efficient operating regimes and device requirements at a relatively low computational cost. The bulk of model complexity exists in the first few cycles of primary capacitor discharge due to the cursory effects of inductive gas breakdown. Hence, a single-pulse model with an adjustable gas distribution function input enables us to stitch together many pulses without much added effort to predict quasi-steady-state operation. We give the single-pulse formulation first to portray current sheet dynamics in detail with relevance to HiPeR-PIT experimentation, then offer the steady-state adjustment in the next chapter to preface our backfill study. Sections 2.1, 2.2, 2.4, and 2.6 are developed by Little *et al.* [58] ahead of this thesis.

2.1 Lumped-element Circuit Model

All former 1D modeling efforts of the planar IPPT have stemmed from a touchstone simulation code developed by Dailey and Lovberg [8, 37] that treated the thruster as an electrical transformer with the drive coil as the primary and the annular ring of plasma as the secondary load. The key insight of their original description was that mutual inductance between the elements decreased monotonically with increasing axial separation, approximated by an exponential decay function. Fig. 2.1 depicts the lumped-element circuit model in two equivalent forms with the thruster (left) inductively coupled to the plasma (right). Here, the mass-driver is modeled as a capacitive energy storage bank (capacitance C_0) connected in series with the coil winding (inductance L_c) via the PPU switching mechanism. The self-contained coil circuit carries some initial, parasitic inductance L_0 and an internal resistance R_c. The plasma sheet develops an opposing current when subject to the inductive force of the driver and coalesces with some resistance R_p, which is related to the resistivity and geometry of the loop. Fig. 2.1(b) emphasizes the schematic transformer concept which gives mutual inductance M, allowing for a 1D pulsed model.

We adopt the circuit models of Martin and Eskridge [42] as well as Polzin and Choueiri [44], which follow from the original semi-empirical work by Dailey and Lovberg. The mesh equations of the equivalent circuit in Fig. 2.1(b) from Kirchhoff's law are:

$$M\frac{dI_c}{dt} + L_0\frac{dI_p}{dt} - I_c\frac{dM}{dt} + I_pR_p = 0 \tag{2.1}$$

$$(L_0 + L_c)\frac{dI_c}{dt} - M\frac{dI_p}{dt} + I_cR_c - I_p\frac{dM}{dt} = V_0. \tag{2.2}$$

We express the voltage of the circuit as a function with respect to time, $V(t)$. Proceeding with dot-notation to denote time derivatives, we arrive at the coupled set of IPPT circuit equations:

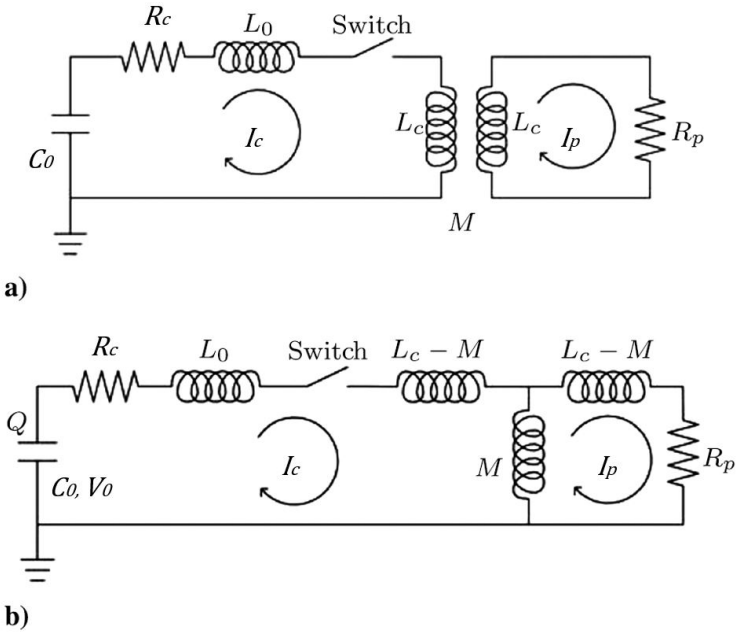

Figure 2.1: Circuit models: (a) general lumped-element representation of a pulsed inductive accelerator and (b) equivalent coil-plasma circuit (after [23, 37]). Here, initial capacitor discharge C_0 drives a current I_c through the accelerator coil with inductance gain L_c through a stray inductance of L_0. The plasma couples to the thruster with mutual inductance M, generating a current I_p with a bulk internal resistance R_p.

$$\dot{I}_c = \frac{L_c V - L_c R_c I_c - M R_p I_p + (L_c I_p + M I_c)\dot{M}}{L_c(L_0 + L_c) - M^2} \tag{2.3}$$

$$\dot{I}_p = \frac{M\dot{I}_c + I_c\dot{M} - R_p I_p}{L_c} \tag{2.4}$$

$$\dot{V} = -\frac{I_c}{C}. \tag{2.5}$$

Eqs. (2.3-5) represent a closed set if M and R_p are taken to be fixed quantities, but as we mentioned, this would be an inaccurate assumption and would tell us very little about the plasma and the system. We must therefore add equations of motion and conservation laws, as well as particle interactions and other various plasma processes.

2.2 Acceleration and Plasma Models

The circuit equations have traditionally been accompanied by a time-varying approximation of mutual inductance that relies on the coupling distance between the lumped elements (z_c) as well as a 1D momentum equation. By explicitly assuming a value for the electron temperature (T_e), previous simulations could forego the need for a plasma model by approximating R_p at low temperature regimes characteristic to EP thrusters. They assumed that current sheet formation was immediate (at $t = 0$) and complete, signifying that the induced magnetic field would not diffuse through the plasma for the duration of the pulse. Results of these efforts have been compared with experimental data to declare a sufficient degree of accuracy in the acceleration regime for ignoring transient effects, as seen in Fig. 2.2.

The waveform comparison is a symbolic vignette as it depicts promising overlap between observed and theoretical results, but also yields evidence that the idealized model misses key behaviors, such as the secondary "crowbar" discharge forming at the coil face around $t = 5\mu$s. The plasma model is the crux of our contribution to the prediction of sheet dynamics, as it attempts to capture both ionization and CX collisions. We detail the simplifications made by earlier models, then present equations that expand the formation physics.

2.2.1 Simplified Models

Mutual Inductance

Different approaches have been taken to find an expression for mutual inductance, relying on either the effective inductance of the coil (L_{eff}) or experimental measurements. The former, which we source from Martin and Eskridge [42], is written as

$$L_{eff} = L_c - \frac{M^2}{L_c} \tag{2.6}$$

provided the resistance of the slug is small compared to its inductive reactance. Eqn. 2.6 may be recast as

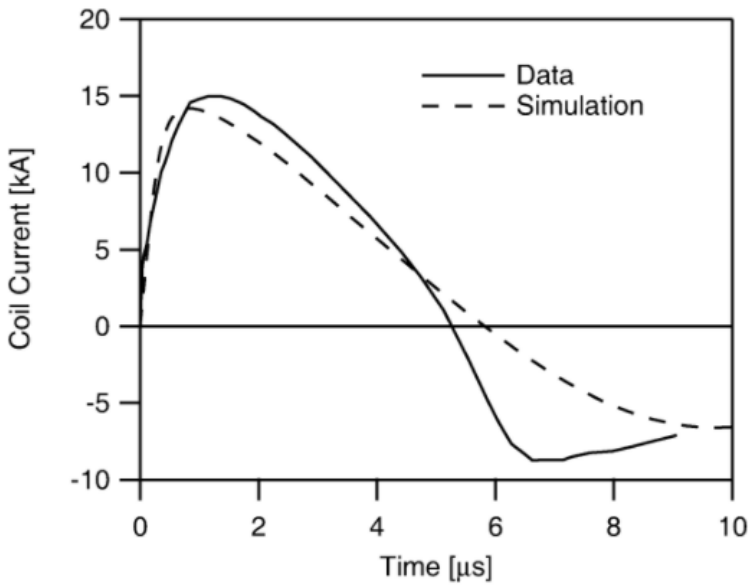

Figure 2.2: Comparison of experimentally acquired (from [19]) and numerically generated current traces in the PIT MkVI (after [44]). Data shown is the same as Fig. 1.1(b).

$$L_{eff} = L_c(1 - k^2) \tag{2.7}$$

where k is the transformer coupling coefficient, defined as

$$k = M/L_c. \tag{2.8}$$

The work by Dailey and Lovberg [8] determined that L_{eff} can be accurately modeled as a spatially-dependent function according to the form

$$L_{eff}(z) = L_c \left[1 - k_0^2 \exp\left(-\frac{2z}{z_c}\right)\right] \tag{2.9}$$

where k_0 is the coupling coefficient at $z = 0$. $M(z)$ then becomes

$$M(z) = k_0 L_c \exp\left(-\frac{z}{z_c}\right) \tag{2.10}$$

such that $k(z)$ also assumes an exponential decay of the form

$$k(z) = k_0 \exp\left(-\frac{z}{z_c}\right). \tag{2.11}$$

Deriving the 1D mutual inductance relation in terms of lumped-element system coupling emphasizes the dependence of current sheet dynamics on k and z_c. These parameters are also critical to our model as we assume similar exponential decays with respect to z, shown in Section 2.2.2.

Slug and Snowplow Models

Earlier 1D models have treated the plasma current sheet as a rigid 'slug' [2, 39, 42] or 'snowplow' [23, 43, 44] depending on the initial distribution of propellant gas and the pulse mode. The mass of the sheet is held at a fixed value in the slug model, whereas the snowplow is assumed to entrain all of the injected propellant in the downstream wake of the thruster. These formulations represent two extremes at the ends of a mass utilization spectrum, since it is predicted that partial entrainment will occur depending on the input conditions. The propellant mass in the sheet as a function of time for the slug and snowplow models respectively can be written as

$$m(t) = m_0, \tag{2.12}$$

$$m(t) = m_0 + \int_0^t \rho_0 v_s dt \tag{2.13}$$

where m_0 is the initial mass bit of injected gas, ρ_0 is the linear mass density distribution, and v_s is the sheet velocity [44]. The linearly decaying density function poorly represents the distribution of background neutrals in a real accelerator, which we amend in section 2.2.3. The momentum equation for the snowplow system follows from Eq. (2.13) as

$$\frac{L_c I_c^2}{2z_c} \exp\left(-\frac{z}{z_c}\right) = \rho_0 v_s^2 + m(t)\frac{dv_s}{dt}. \tag{2.14}$$

Here, the left-hand term represents the self-field electromagnetic force, balanced with entrained momentum and accelerated mass on the right. We adjust Eq. (2.14) to account for partial mass entrainment in Section 2.2.4.

Energy and State Properties

Polzin *et al.* [43] improved upon the initial models by including equations governing the temporal evolution of plasma temperature and energy partitioning. To do so, the current sheet was treated as a finite-volume snowplow element over which state properties could be integrated, permitting a time-varying energy flux to permeate through the gas and allowing for the calculation of plasma pressure. The revised model utilized a non-ideal, real-gas equation to close the system, thereby opening the possibility for tailoring the simulation to different propellants. The added equations were rederived from the general fluid model for self-consistency to include additional terms not found in previous work [42, 44]. Of note to our review, this included the general MHD momentum equation:

$$\rho\left(\frac{\partial \mathbf{v}}{\partial t} + \mathbf{v}\cdot\nabla\mathbf{v}\right) = -\nabla P + \mathbf{J}\times\mathbf{B} \tag{2.15}$$

where P is the plasma pressure. Integrating, Eq. (2.15) becomes

$$\frac{dv_s}{dt} = \left[\frac{L_c I_c^2}{2z_c}\exp\left(-\frac{z}{z_c}\right) - \rho_0(z)v_s^2 - P_0\pi(r_o^2 - r_i^2)\right]/m(t) \tag{2.16}$$

where r_o and r_i denote the outer and inner radii of an annular PIT coil design, respectively. By assuming a value for the ambient temperature (T_0) and assuming a triangular mass distribution profile ahead of the current sheet in the $\hat{z}$-direction, neutral gas pressure was calculated from the ideal gas equation of state:

$$P_0 = \frac{\rho_0}{\pi(r_o^2 - r_i^2)} \frac{k_B}{m_i} T_0 \tag{2.17}$$

where m_i refers to the atomic (or molecular) mass of the propellant. The total energy of the current sheet was calculated by integrating the MHD energy density equation for the plasma, expressed as

$$E = \frac{n_s k_B T_e}{\gamma - 1} w_s \pi (r_o^2 - r_i^2) + \frac{1}{2} m_s v_s^2 + \frac{1}{2} L_c I_c^2 \tag{2.18}$$

where n_s is the sheet density, γ is the ratio of specific heats, and w_s is the sheet width as estimated by resistive diffusion.

This model also assumed a multi-level ionization equilibrium and pressure-varying γ, which we do not account for in our study. These effects were seen in the numerical update of transport properties and the plasma equation of state, but were determined to be generally extraneous at lower temperatures. A few conclusions of this study have been relevant to our own:

- When operating with argon propellant, plasma properties exhibit dynamic behavior during the early cycles of a discharge. Once the sheet accelerates downstream and decouples from the coil, density and temperature level off to a constant value while the pressure continues to decrease from thermal expansion.

- Initial temperature choice has only a minor effect on PIT performance.

2.2.2 Mutual Inductance

We begin our own formulation with the adjustments to the coupling approach of simplified models. The mutual inductance between the planar coil and the disc conductor is still described to decrease exponentially with the ratio of the distance between the two elements, but we adjust Eq. (2.10) to be written as

$$M = (1 - \Theta_e) L_c \exp\left(-\frac{(z_s - z_a)}{z_c}\right) \tag{2.19}$$

where z_a is the distance between the acceleration coil and the gas injection plane as seen in Fig. 2.3. We adopt a simplified geometry where the origin ($z = 0$) corresponds to the plane at which neutral gas is injected in front of the thruster face, mirroring the HiPeR-PIT design. The width, location, and density of the sheet all evolve with time, but the plasma is assumed to posses an inner radius (r_i) and outer radius (r_o), just like the thruster. Radial expansion is ignored, thus $\dot{r_i} = \dot{r_o} = 0$.

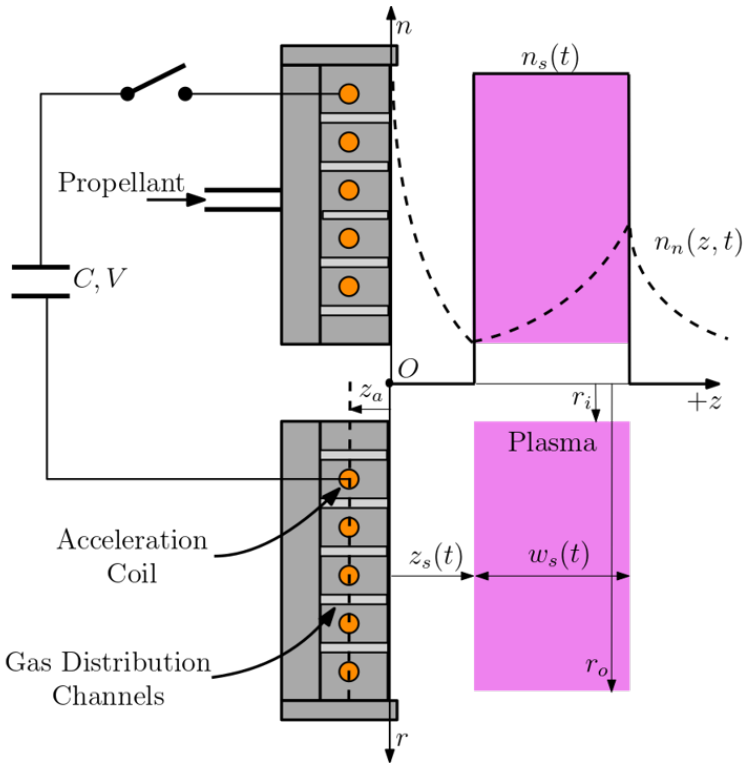

Figure 2.3: Simplified side-on view of the HiPeR-PIT showing the inter-coil gas injection scheme as well as sheet position (z_s), sheet width (w_s), and coil offset (z_a) as defined in the 1D model. The density axis depicts an exaggerated spatial distribution of the background neutrals (n_n) as a dashed curve and the current sheet density (n_s) as a solid step function.

We also note that we have introduced an additional factor $(1 - \Theta_e)$ to Eq. (2.19) to account for the transparency of the plasma to electromagnetic fields imposed by the thruster such that $\Theta_e \in [0, 1]$. In further analysis, we refer to Θ_e as the EM transparency of the current sheet. The limit $\Theta_e \to 0$ corresponds to the simplified assumption of a perfectly conducting plasma, whereas the opposite limit $\Theta_e \to 1$ denotes complete transparency or zero energy transfer between the lumped thruster elements. Conceptually, the value of this parameter depends on the presence and ability of charge carriers in the plasma to respond to the field fluctuations on timescales that are relatively short compared to the period of the current oscillation in the coil. We can quantify this by accounting for the collisionality and internal structure of the current sheet. Assuming that the plasma is a uniform conductor with skin depth δ_s we can simplify the transparency over total body of the sheet as

$$\Theta_e = \exp\left(-\frac{cw_s}{\delta_s}\right) \tag{2.20}$$

where c is a constant and δ_s depends on microscopic processes in the plasma responsible for the attenuation of low-frequency EM radiation, described in further detail in Section 2.2.7.

When the width far exceeds the skin depth of the current sheet ($w_s \gg \delta_s$), we see that $\Theta_e \to 0$, reflecting the favorable ability of the charge carriers to respond to incident AC fields and establish an induced current density that cancels out those fields. In the opposite limit where $w_s \ll \delta_s$, the incident fields are unaffected by the particle response in the plasma, and mutual inductance suffers accordingly.

We choose $c = 3$ in our analysis to give roughly 5% transparency when $w_s = \delta_s$. This is consistent with experimental measurements by Dailey and Lovberg [17,32] that demonstrated the magnetic field in the current sheet penetrates a distance that is roughly three times the width of the high density region in the PIT exhaust. For the purposes of this model, the use of a semi-empirical penetration constant is sufficient to examine efficiency scaling for different background conditions at short timescales. Higher-dimensional models would be required to further diagnose internal current sheet microstructure and field impacts.

2.2.3 Conservation of Mass

We utilize a multi-fluid model that is volume-integrated to average the equations over the dimensions of the plasma, permitting the expression of the properties within the current sheet using a single set of terms in 1D. Propellant mass entrainment is modeled using the non-equilibrium continuity equation for neutral particles in the presence of electron impact ionization and charge-exchange collisions. We assume three-body and dielectric recombination effects to be negligible. Convective transport of neutral particles generally occurs on timescales much slower than the LC-period of the discharge circuit allowing neutral continuity to be expressed as

$$\dot{n}_n = \begin{cases} 0 & z < z_s \\ -\left(S_{ion} + \sigma_{cx} v_s\right) n_n n_s & z_s \leq z \leq z_s + w_s \\ 0 & z > z_s + w_s. \end{cases} \tag{2.21}$$

Above, n_n is the number density of neutral particles, S_{ion} is the ionization reaction rate, and σ_{cx} is the charge-exchange cross section. S_{ion} and σ_{cx} are both dependent on the propellant type, and are more difficult to ascertain analytically for molecular species. We also note that $n_n(z,t)$ is the only spatiotemporal variable in our model, which is necessary because z-dependence allows us to understand how the gas density evolves as the plasma sheet grows and accelerates. Eq. (2.21) is piecewise-defined so that particle entrainment is limited to the current sheet volume, $z \in [z_s, z_s + w_s]$.

Conservation of mass calls for a closed system in which the neutral gas particles that are consumed by the plasma via ionization and CX collisions appear elsewhere in the model. For ionizing collisions, the neutral particle becomes an ion, yielding a source term in the ion continuity equation to balance the loss term in Eq. (2.21). CX collisions do not create ions but instead transfer momentum from a fast-moving ion to a slow-moving neutral particle. The result is a neutral particle of higher kinetic energy than the injected background neutrals, which we separate into constituent species. "Fast" neutral density (n_f) is treated as a distinct

fluid among the "slow" background distribution.

Volume-integration of the plasma (ion or electron) continuity equation across the uniform sheet yields

$$\frac{d(w_s n_s)}{dt} = n_s w_s S_{ion}(\bar{n}_n + n_f) \tag{2.22}$$

where

$$\bar{n}_n = \frac{1}{w_s}\int_{z_s}^{z_s+w_s} n_n dz \tag{2.23}$$

is the average density of slow neutrals within the current sheet. The two source terms on the right-hand side of Eq. (2.22) represent the creation of ion-electron pairs via ionization of slow and fast neutrals, respectively.

Volume-integration of the fast neutral continuity equation gives

$$\frac{d(w_s n_f)}{dt} = n_s w_s \left(\sigma_{cx} v_s \bar{n}_n - S_{ion} n_f\right) - n_f \Delta v_{sf} H(\Delta v_{sf}). \tag{2.24}$$

Here, we define $\Delta v_{sf} = v_s - v_f$ as the velocity difference between the plasma sheet and the fast neutral fluid, and H denotes the Heaviside step function. The first term on the right-hand side of the equation represents the creation of fast neutrals by CX collisions. The second term captures the loss of fast neutrals via electron-impact ionization in a Fokker-Planck model. The third term describes the convective loss of fast neutral particles from the trailing boundary in the wake of the sheet. We refer to this de-entrainment process as neutral "slip".

In a similar line of analysis as the previous section, we can express the transparency of the current sheet to upstream propellant mass. Eq. (2.21) reveals that the frequency at which a neutral particle at a given 1D location in space is consumed by the uniform conductor is $n_s(S_{ion} + \sigma_{cx} v_s)$. The residence time of the current sheet in the vicinity of a particle location is given by w_s/v_s; hence, we can express the dimensionless probability that a given particle

is consumed via either ionization or a CX collision. We refer to this as the mass entrainment transparency, described by the product of separate processes as $\Theta_m = \Theta_{m,ion}\Theta_{m,cx}$, where

$$\Theta_{m,ion} = \exp\left(-\frac{n_s w_s S_{ion}}{v_s}\right) \tag{2.25}$$

and

$$\Theta_{m,cx} = \exp\left(-n_s w_s \sigma_{cx}\right). \tag{2.26}$$

As probabilities, $\Theta_{m,ion}$ and $\Theta_{m,cx}$ are a bit counterintuitive. The snowplow model (i.e. total entrainment) is valid in the limit $\Theta_m \to 0$. Alternatively, the slug model is transparent to neutral propellant mass in the limit $\Theta_m \to 1$, and conservation ensures that $\Theta_m \in [0, 1]$.

2.2.4 Conservation of Momentum

Volume-integration of the plasma fluid (ion and electron) momentum conservation equations provides an expression for the acceleration of the current sheet with evolving mass:

$$\frac{d(w_s n_s v_s)}{dt} = (1 - \Theta_e)\frac{L_c I_c I_p}{m_i A_s z_c}\exp\left(-\frac{(z_s - z_a)}{z_c}\right) - f_c. \tag{2.27}$$

Here, the first and second terms on the right-hand side of the equation represent the Lorentz and collisional forces on the plasma per unit area per unit atomic mass. $A_s = \pi(r_o^2 - r_i^2)$ is the cross-sectional area of the annular PIT, a term we condense from Eq. (2.16). Note that this formulation departs from self-consistent energy model by diversifying the particle interactions. The Lorentz force term, whose form is detailed by Martin and Eskridge [42] and expanded by Polzin *et al.* [43], is modified to include the finite transparency developed in Eq. (2.20). We have neglected the force due to the background neutral pressure gradient because it is found to be negligible in all cases - even for a backfill in the millitorr range. This is because the dynamic plasma pressure ($q_s = n_s m_i v_s^2/2$) is significantly higher than ambient chamber pressure for favorable sheet conditions.

The collisional force term tracks the momentum sapped from or added to the current sheet by entrainment processes. In the snowplow model, this effect scaled with v_s^2 [43]. To account for momentum transfer due to CX and ionizing collisions, we edit to get

$$f_c = \left(\bar{n}_n \sigma_{cx} v_s^2 + n_f \sigma_{cx} \left|\Delta v_{sf}\right| \Delta v_{sf} - n_f S_{ion} v_f\right) n_s w_s. \tag{2.28}$$

Noting the signs attached to each term, this equation accounts for momentum transfer away from the ions due to CX collisions as well as momentum transfer to the ions by the fast neutral population. Above, we assume the following: (1) slow neutral particles possess a much lower velocity than the plasma sheet and therefore do not add momentum via ionization; (2) ion-neutral collisions are dominated by charge-exchange; and (3) the momentum transfer cross section for electron-neutral collisions is negligible compared to σ_{cx}.

Volume-integration of the fast neutral fluid momentum conservation equation balances the collisional force according to

$$\frac{d(w_s n_f v_f)}{dt} = f_c - n_f v_f \Delta v_{sf} H(\Delta v_{sf}). \tag{2.29}$$

In this case, CX collisions are a source of momentum for the fast neutral population, whereas ionization reactions represent a momentum sink. The second term on the right-hand side captures the possible loss of momentum due to neutral slip at the trailing edge of the sheet. we again neglect the force due to ambient pressure gradients, which are still negligible compared to the dynamic pressure of the fast neutral fluid. This assumption is valid for

$$\left(\frac{\lambda_f}{w_s}\right)\left(\frac{c_{s,f}}{v_s}\right)^2 \ll 1 \tag{2.30}$$

where $c_{s,f} = \sqrt{e_c T_f / m_i}$ is the fast neutral sound speed and $\lambda_f = (n_s \sigma_{cx})^{-1}$ is the charge-exchange mean free path. Since the ion kinetic energy is the only source of fast neutral thermal energy, $(c_{s,f}/v_s) < 1$. We assume $(\lambda_f / w_s) \ll 1$ for an abundance of fast neutrals from the entrainment process across a pulse, so Eq. (2.30) is well-founded.

Lastly, the location of the current sheet evolves according to the straightforward kinematic equation of motion

$$\dot{z_s} = v_s \tag{2.31}$$

which is consistent with [8] and closes the conservation of momentum.

2.2.5 Conservation of Energy

As with the simplified models, the equations presented thus far form a closed system for the inductive acceleration of a current sheet assuming fixed values of R_p, δ_s, and S_{ion}. By including the particle interactions for neutral entrainment, however, we acknowledge that these quantities depend on microscopic processes in the plasma which are strongly influenced by the temperature of electrons in the conductive body. We therefore examine the energetics of inductive acceleration and mass entrainment through the heating and cooling of the electron population. To offer some examples, currents induced within the plasma increase T_e via Ohmic heating (i.e. Joule heating), and electron-impact excitation and ionization of neutral particles decrease T_e. The timescales for these processes vary widely across the parameter spaces relevant to PIT plasmas, but some are especially dynamic after the first few cycles of capacitor discharge, meriting particular attention within the context of sheet formation.

The temporal evolution of T_e is derived by volume-integrating the electron energy equation [43] for a uniform plasma, neglecting electron kinetic energy terms due to insignificant mass and assuming zero heat flux from the volume. The latter simplification is ill-suited to conditions with greater ambient temperature gradients, but a closed thermodynamic system is sufficient for the scope of this model. This also allows us to neglect the pressure-varying ratio of specific heats. Thus,

$$\frac{d(n_s w_s T_e)}{dt} = \frac{2}{3A_s}(P_{ohm} - P_{inel} - P_{ei}), \tag{2.32}$$

where

$$P_{ohm} = \frac{R_p I_p^2}{e_c}, \tag{2.33}$$

$$P_{inel} = S_{ion} n_s w_s A_s (\bar{n}_n + n_f) \varepsilon^*_{ion}, \tag{2.34}$$

and

$$P_{ei} = \frac{3 m_e \nu_{ei}}{m_i} (T_e - T_i). \tag{2.35}$$

Here, ε^*_{ion} denotes the effective ionization energy and ν_{ei} is the electron-ion Coulomb collision frequency. We also introduce e_c as the elementary charge (implemented for unit consistency), m_e as electron mass, and T_i as ion temperature. Eq. (2.32) describes power gained by the sheet due to Ohmic heating and lost due to inelastic collisions and Coulomb collisions between the electron and ion populations.

Since Eq. (2.35) depends on the ion temperature, we must also account for time-evolving T_i in the model. Volume-integration of the ion energy equation [43] assuming a uniform plasma and zero heat flux at the boundaries yields

$$\frac{d(n_s w_s T_i)}{dt} = \frac{2}{3 A_s} (P_{ei} + S_{ion} n_s \bar{n}_n w_s A_s T_n). \tag{2.36}$$

We introduce T_n as the temperature of the background neutral gas and note from the right-hand side of the equation that only Coulomb collisions and thermal energy from the ionized neutrals act as heat sources for the ions. This is because Eq. (2.27) cancels terms associated with the rate of change of ion kinetic energy, work imparted to the current sheet via the Lorentz force, and the effects of momentum transfer and CX collisions. The electron collision rate dominates R_p and hence Ohmic heating, so Eq. (2.36) is sufficient. We acknowledge that the background neutral gas does not have a great effect on the thermal energy of the ions, so we do not explore this parameter space in our backfill study. Since this model is in 1D, no attempt is made to track energy conversion from radial current sheet motion to axial

momentum due to expansion in the chamber.

2.2.6 Sheet Width

We close our 1D model by identifying the time-evolution of current sheet width, which naturally changes on a scale of $\mathcal{O} \sim 0.1 - 10$ mm as the entrainment and slip processes take effect. Previous models either assume a constant sheet width [2, 7, 8, 42, 44] or one that changes in time due to resistive diffusion of the magnetic field [43]. Since our model aims to understand how ionization impacts the early formation of the plasma sheet from a pre-ionized state, we take the rate of change of sheet width as

$$\dot{w}_s = \frac{D_p}{w_s} + (\dot{w}_s)_f \tag{2.37}$$

where the first term on the right-hand side represents width increase from plasma diffusion with diffusivity D_p, and the second term encapsulates changes that occur during the formation process.

The second formation term can assume a great deal of complexity with the inclusion of current sheet microstructure and EM field composition. Early work attempting to understand the former [17, 32] discovered layered effects within the plasma beyond the scope of the lumped-element circuit description. Instead, we rely on phenomenological arguments to approximate $(\dot{w}_s)_f$ on shorter timescales.

First, we assume that newly formed plasma particles accumulate within a span of $z \in [z_s, z_s + \delta_s]$ for cases where $w_s \geq \delta_s$. This is because the azimuthal plasma current density is strongest in the skin depth layer facing the thruster, as this region will also possess the highest local electron temperature and ionization rate. Consequently, the entrainment process will preferentially deposit new plasma particles in the skin depth layer of the sheet, trending w_s toward δ_s at a rate directly proportional to the relative rate of density gain. Oppositely, when $w_s < \delta_s$, newly created sheet particles accumulate within $z \in [z_s, z_s + w_s]$, implying that $(\dot{w}_s)_f = 0$. We therefore model the formational width change using the Heaviside function

as

$$(\dot{w}_s)_f = (\delta_s - w_s)H(w_s - \delta_s)\frac{\dot{N}_s}{N_s}. \tag{2.38}$$

Here, $N_s = w_s n_s A_s$ is the total number of ions in the current sheet - a value that evolves with time according to our elementary state variables. Using the chain rule to expand $\dot{N}_s/N_s$, we recast Eq. (2.38) to arrive at a final equation for the rate of change of sheet width

$$\dot{w}_s = \frac{D_p}{w_s} + (\delta_s - w_s)\left(\frac{\dot{w}_s}{w_s} + \frac{\dot{n}_s}{n_s}\right)H(w_s - \delta_s). \tag{2.39}$$

Looking at the groupings in the above equation, we emphasize that $w_s \to \delta_s$ in the limit $D_p \to 0$ and $w_s > \delta_s$ provided $\dot{n}_s/n_s \gg 1$. This makes intuitive sense because when $\dot{n}_s/n_s \ll 1$, neutral gas entrainment is insignificant and $\dot{w}_s \to 0$, approaching the slug model.

2.2.7 Microscopic Processes and Transport Properties

Our multi-fluid model is built on a platform of parameters that are derived from a statistical averaging of the microscopic (particle scale) processes in the plasma current sheet. Exhaust interactions with neutral background particles through ionization and CX collisions are critical to the study of facility effects since they alter the current density in the conducting element [51]. In particular, we summarize the equations for R_p, D_p, δ_s, and ε^*_{ion} mentioned in previous sections.

In a 1D model, the resistance of the plasma is a geometric property, where we treat the current sheet as a conducting annular disc with uniform resistivity η_p,

$$R_p = \frac{\pi\eta_p}{\min(w_s, \delta_s)}\left(\frac{r_o + r_i}{r_o - r_i}\right). \tag{2.40}$$

We utilize the min function in the denominator to identify the region in which the current is distributed across the temporal evolution of a pulse. The plasma resistivity is calculated from classical kinetic theory

$$\eta_p = \frac{m_e(\nu_{ei} + \nu_{en})}{n_s e_c^2} \tag{2.41}$$

where ν_{en} is the electron-neutral collision rate, which is not previously accounted for in the electron energy equation. We model the collision rate equations using temperature-dependent statistical models for atomic propellants

$$\nu_{ei} = 2.91 \times 10^{-12} n_s T_e^{-3/2} \ln \Lambda \tag{2.42}$$

$$\nu_{en} = n_n \sigma_{en} \sqrt{\frac{8 e_c T_e}{\pi m_e}} \tag{2.43}$$

where σ_{en} is the electron-neutral collision cross section for IPPT-relevant regimes, and

$$\ln \Lambda = \begin{cases} 23 - \ln\left(T_e^{-3/2}\sqrt{n_{s,\mathrm{cm}^{-3}}}\right) & T_e < 7.389 \text{ eV} \\ 24 - \ln\left(T_e^{-1}\sqrt{n_{s,\mathrm{cm}^{-3}}}\right) & T_e \geq 7.389 \text{ eV} \end{cases} \tag{2.44}$$

is the Coulomb logarithm. We use the ambipolar diffusivity coefficient to describe the time-evolution of sheet width, which depends on the electron-ion collision rate (ν_{ei})

$$D_p = \frac{e_c T_e}{m_i \nu_{ei}} \tag{2.45}$$

such that we maintain quasineutrality in the plasma. Skin depth develops according to a resistive diffusion model seen in

$$\delta_s = \sqrt{\frac{2\eta_p}{\mu_0 \omega}} \tag{2.46}$$

where μ_0 is the vacuum permeability and $\omega = 1/\sqrt{L_{eff} C_0}$ is the angular frequency of the incident EM field. We source the effective inductance from Eq. (2.9) such that the coupling coefficient evolves with time.

To model effective ionization energy, we look to Lieberman and Lichtenberg's work on

plasma discharges [59]. This term tracks the electron energy lost to ionization, line radiation, and elastic polarization scattering

$$\varepsilon^*_{ion} = \varepsilon_{ion} + \frac{1}{S_{ion}} \left(\sum_j \left(S_{ex,j} \varepsilon_{ex,j} \right) + \frac{3 m_e T_e S_{es}}{m_i} \right) \tag{2.47}$$

where ε_{ion} is the first ionization energy of the propellant gas, $S_{ex,j}$ and $\varepsilon_{ex,j}$ are the electron-impact excitation reaction rate and energy for the j^{th} line transition, and S_{es} is the scattering reaction rate. We neglect losses from elastic polarization scattering of electrons off neutrals, which are insignificant above $T_e \approx 2$ eV. Higher-temperature radiation losses are assumed to be negligible as well since we only examine $T_e < 50$ eV regimes.

Collision and reaction rates involving electrons (i.e. S_{ion}, $S_{ex,j}$, S_{es}, ν_{ei}, and ν_{en}) are modeled assuming a Maxwellian electron energy distribution. This is due to the faster electron thermalization times in the current sheet relative to the impulse-carrying ions. Statistical rates for ion collisions (i.e. σ_{cx}) assume a cold ion population. That is, $v_s \gg \sqrt{e_c T_i / m_i}$, which is a fair assumption in EP applications.

2.3 Propellant Models

Our fluid model assumes a heterogeneous population of ions, electrons, and neutrals to segregate the composition of the plasma sheet. We present noble gas models for the use of argon and xenon propellants, which are advantageous in EP applications due to their high ionization energies. In the trade space between thrust and efficiency, lighter propellants achieve higher average exhaust velocities at the cost of poor input power utilization. Argon has lighter atoms and is hypohesized to reach favorable specific impulses. Xenon is attractive as due to its low critical temperature and pressure, allowing for high-density storage.

2.3.1 Argon and Xenon

We approximate the ion mass of a given propellant using the standard value for a mass of a proton as

$$m_i = 1.67 \times 10^{-27} D_a \tag{2.48}$$

where D_a is the atomic weight. We implement $D_a = 39.948$ for argon and $D_a = 131.293$ for xenon, depicting a wide difference in m_i. This will be apparent in the results, particularly with respect to mass utilization and the steady-state migration of neutral density.

Approximate collisional cross sections (from [59, 60] for argon, [61, 62] for xenon) and first ionization and excitation potentials are provided in Table 2.1. We note that σ_{cx} is more rigorously a function of sheet velocity, but we apply a first-order approximation in the predicted ranges of v_s.

Table 2.1: Collisional cross sections and first ionization and excitation potentials for argon and xenon plasmas, averaged across $T_e \in [10, 40]$ eV.

	Argon (Ar)	Xenon (Xe)
σ_{cx} (m^2)	5×10^{-19}	7.5×10^{-19}
σ_{en} (m^2)	4×10^{-20}	5×10^{-20}
ε_{ion} (eV)	15.76	12.13
$\varepsilon_{ex,1}$ (eV)	12.14	8.84

As aforementioned, reaction rate coefficients assume a Maxwellian electron energy distribution and can be analytically fit using temperature-dependent statistical models. The argon model uses rate parameters given by [3] as

$$S_{ion} = 2.34 \times 10^{-14} T_e^{0.59} \exp\left(-17.44/T_e\right) \tag{2.49}$$

$$S_{ex,1} = 2.48 \times 10^{-14} T_e^{0.33} \exp\left(-12.78/T_e\right) \tag{2.50}$$

$$S_{es} = 2.336 \times 10^{-14} T_e^{1.609} \exp\left(0.0618(\ln T_e)^2 - 0.1171(\ln T_e)^3\right). \tag{2.51}$$

The rate coefficients in our xenon model appear differently since we source from the appendices in [4], but sample electron temperatures reveal similar orders of magnitude

$$S_{ion} = 10^{-20}\sqrt{\frac{8e_cT_e}{\pi m_e}}(-1.031\times10^{-4}T_e^2 + 6.386\exp\left(-12.127/T_e\right)) \tag{2.52}$$

$$S_{ex,1} = 1.93\times10^{-19}T_e^{-1/2}\sqrt{\frac{8e_cT_e}{\pi m_e}}\exp\left(-11.6/T_e\right) \tag{2.53}$$

$$S_{es} = 6.6\times10^{-19}\sqrt{\frac{8e_cT_e}{\pi m_e}}\left(\frac{Te/4-0.1}{1+(T_e/4)^{1.6}}\right). \tag{2.54}$$

2.3.2 Molecular Propellants

Molecular propellants (e.g. hydrazine, water vapor, carbon dioxide, etc.) burden the equations with a more complex plasma chemistry and composition, and are therefore beyond the scope of the model we present. However, they posses many desirable traits, not the least of which is better measured performance on legacy PIT prototypes [8, 9, 16, 31, 37]. They also open possibilities to higher-density storage, ISRU [14], and lower propellant costs for testing.

The development of a multi-species chemical kinetic IPPT model would be helpful in characterizing the scaling laws relevant to specific gases. Since our model neglects dissociative recombination, the presence of large temperature gradients, and the effects of asymmetric CX reactions, our model falls short and would need to be adjusted to place less emphasis on charge-exchange for neutral particle entrainment [63]. Still, a similar structure of equations could be expanded to reach a simplified understanding of molecular PIT propellant physics.

2.4 Initial Conditions and Model Inputs

Eqs. (2.3-5), (19), (21-22), (24), (27), (29), (31-32), (36), and (39) comprise a closed system of thirteen ordinary differential equations (ODEs) that consistently evolve the state variables: I_c, I_p, V, M, n_n, n_s, n_f, z_s, v_s, v_f, T_e, T_i, and w_s. These effectively diagnose the plasma across the time-duration of a pulse, but some are not representative of engineering design points used in thruster and PPU development. Instead, we reformulate the initial conditions (ICs) to agree with the design process and to explore current sheet formation and propellant mass entrainment for a pre-ionized plasma.

At $t = 0$, we presuppose the existence of a stationary pre-ionized sheet (i.e. $v_s(0) = v_f(0) = 0$) where we can control the initial width ($w_{s,0}$) and location ($z_{s,0}$) based on data in the literature. We establish a spatial pre-ionization function

$$\chi_i(z) = \frac{n_{i,pi}(z)}{n_{n,inj}(z)} = \chi_0 H(w_{s,0} - z) \tag{2.55}$$

where $n_{i,pi}(z)$ is the ion density profile following pre-ionization and $n_{n,inj}(z)$ is the injected neutral density profile. We generalize this proportion to an initial pre-ionization fraction, χ_0, distributed uniformly over some characteristic length scale immediately adjacent to the injection plane. For all cases in our analysis, this length scale is assumed to equal $w_{s,0}$ since the depth of PI is experimentally determined. Eq. (2.55) allows us to semi-empirically define the initial neutral and sheet density profiles as

$$n_n(z, 0) = [1 - \chi_i(z)] n_{n,inj}(z) \tag{2.56}$$

and

$$n_s(0) = \int_{z_{s,0}}^{z_{s,0}+w_{s,0}} \chi_i(z) n_{n,inj}(z) dz. \tag{2.57}$$

We assume that CX collisions take place solely within the timespan of a pulse, so there are no fast neutrals in the pre-ionized plasma fluid (i.e. $n_f(0) = 0$). Thus, only two input functions, $\chi_i(z)$ and $n_{n,inj}(z)$, contribute to the initial neutral density profile, $n_n(z, 0)$. The distribution function of background neutrals is central to our model efficacy and backfill comparison. To simulate the injected neutral density of a thruster in space, or in near-perfect vacuum, we assume an exponential profile

$$n_{n,inj}(z) = n_{n,0} \exp\left(-z/z_n\right) \tag{2.58}$$

with a maximum value $n_{n,0}$ at the gas injection plane. This function can be manipulated to mirror different background pressures and conditions.

As for the circuitry, we follow the PIT operating principles and assume that a primary bank with capacitance C_0 is charged to an initial voltage V_0, and discharged once the switch closes at $t = 0$. Hence, there is no initial current in either the coil or the plasma (i.e. $I_c(0) = I_p(0) = 0$), which is maintained by rapid switching in steady state. Initial mutual inductance can be ascertained from the transcendental equation for the initial coupling coefficient via Eq. (2.8)

$$k_0 = \exp\left(-\frac{(z_{s,0} - z_a)}{z_c}\right)\left[1 - \exp\left(-\frac{3w_{s,0}}{\delta_{s,0}k_0}\right)\right]. \tag{2.59}$$

This is a necessary computational burden because the initial skin depth ($\delta_{s,0}$) should be consistent with $M(0)$ through L_{eff} [43]. We also take $T_{e,0}$, $T_{i,0}$, and T_n as model inputs because even though temperature evolves with time in our formulation, we must still specify a starting energy for each species. We note that the neutrals are assumed to maintain room temperature for the duration of the pulse.

In summary, we are able to control the design of the PIT circuit (C_0, V_0, R_c, L_c, L_0), coil geometry (r_i, r_o, z_a, z_c), propellant properties (m_i, σ_{cx}, σ_{en}, ε_{ion}, $\varepsilon_{ex,1}$, S_{ion}, $S_{ex,1}$, S_{es}), neutral gas profile ($n_{n,0}$, T_n), and pre-ionized plasma characteristics ($z_{s,0}$, $w_{s,0}$, $T_{e,0}$,$T_{i,0}$, χ_0). Adjusting these inputs allows us to explore performance scaling and understand how tweaking the thruster design and test conditions affect the plasma physics. More inputs are required to complete the steady-state, multi-pulse model which will be discussed in the next chapter.

2.5 Numerical Methods and Simulation Mechanics

We can also adjust the spatiotemporal zone of interest for the simulation such that we develop the state variables over a closed domain, $(z, t) \in ([0, z_{max}], [0, t_{max}])$, where z_{max} and t_{max} are the axial distance and time boundaries of the solution. It naturally follows that z_{max} is determined by the distance at which the current sheet ceases to interact considerably with either the thruster or ambient neutral gas, which can be the downstream chamber wall for

limited test configurations. We regularly set t_{max} equal to the LC-period of the circuit since this limits the dynamic timescales of the electromagnetically-coupled elements, given by

$$\tau_{LC} = 2\pi\sqrt{L_c C_0}. \tag{2.60}$$

In our code, we establish a numerical grid using constant spacing in z and exponentially decreasing spacing in t to collect more data points near the beginning of a pulse. This allows us to better understand regions of highly dynamic behavior. We numerically integrate using a nested Gauss-Kronrod quadrature method and output the state variables as interpolation functions fitted to discrete points collected in time.

2.5.1 Computational Cost

We emphasize the appeal of 1D modeling by reducing computational burden compared to finite-volume multi-dimensional simulations. In contrast with a 2D MHD model [53, 55, 57], ours offers $\mathcal{O}(N)$ versus $\mathcal{O}(N^2)$ computational cost advantage per time step. Over hundreds to thousands of discrete steps, this improvement is massive. We neglect any plasma physics in the radial and azimuthal directions, but in return, we can observe trends at a high enough fidelity for optimization. The 1D model could one day become the real-time, in-space adjustment algorithm for a spacecraft computer. We can also determine with a fair confidence across the majority of PIT regimes whether or not it is worth the experimental effort to test in a backfill.

2.6 Propulsion Performance Metrics

While testing in a backfill will obfuscate the true performance metrics of PIT operation, our model will also characterize these differences in meaningful and nonmeaningful ways. The traditional model outputs of interest are discussed to contextualize our theoretical predictions against a wider body of legacy data, but as they are defined, some metrics will not yield direct predictions for backfill performance - nor should they. The space environment is the

sole set of operating conditions relevant to performance optimization.

Our model is unique in its ability to resolve early dynamics of plasma sheet formation and mass entrainment during acceleration, which strongly influence the performance of the thruster regardless of the operating environment. We present the equations used for analysis here to exhibit the efficacy of our model and later analyze the effects of certain input parameters on system efficiencies.

To start, we introduced I_{sp} and η_T in Eqs. (1.1) and (1.2) earlier in the thesis as the cornerstones of EP performance trade studies. To do so, we made reference to the impulse bit, which refers to the total impulse per unit pulse, or the integral of thrust over the time-duration of a discharge evolution. Consistent with the terminology given in our plasma model, this is

$$I_{bit} = m_i A_s \left[w_s(n_s v_s + n_f v_f) + \int_0^t n_f v_f \Delta v_{sf} H(\Delta v_{sf}) dt' \right] \tag{2.61}$$

where the three terms on the right-hand side of the equation represent contributions from ions, fast neutrals, and slipped neutrals, respectively. Since the constituent state variables that contribute to impulse are each either fixed values or functions with respect to time, we can resolve the temporal evolution of I_{bit} as well to demarcate the acceleration phase of a pulse. The mass bit contributing to I_{sp} and η_T is simply

$$m_{bit} = m_i A_s \int_0^{z_{max}} n_{n,inj} dz. \tag{2.62}$$

We briefly discussed the use of inductive recapture in the current PIT state-of-the-art to raise the system efficiencies by latching the primary capacitor with a non-zero voltage, saving the residual energy for subsequent pulses. This is executed in our model by opening the switch once I_c crosses zero at a particular time step and nullifying the coil current in the circuit equations. We recast the thrust efficiency as the recapture efficiency

$$\eta_R = \frac{m_{bit}(g_0 I_{sp})^2}{2(E_0 + E_{pi} - E_{cap})} \tag{2.63}$$

where

$$E_{pi} = n_{s,0} w_{s,0} A_s e_c \left[5/2(T_{e,0} + T_{i,0}) + \varepsilon^*_{ion}(T_{e,0})\right] \tag{2.64}$$

and

$$E_{cap} = C_0 V^2/2 \tag{2.65}$$

are the initial energy of the pre-ionized plasma and the instantaneous capacitor energy, respectively. As before, $E_0 = C_0 V_0^2/2$ is the total initial circuit energy. We report η_R in the place of η_T in the analysis, since this value is unanimously higher than for zero recapture.

The mass utilization efficiency (η_m) describes the fraction of total propellant bit that is profitably accelerated to the final velocity of the current sheet. Inter-coil gas injection will always produce some minuscule amount of thrust, but only the exhausted plasma will produce any measure of appreciable acceleration. From our model, we calculate this efficiency measure as a time-dependent function

$$\eta_m = \frac{g_0 I_{sp}}{v_s} = \frac{I_{bit}}{m_{bit} v_s}. \tag{2.66}$$

Electrical efficiency (η_e) is a more nebulous metric within PIT theory depending on the scale of analysis. We opt for a lumped-element definition that finds the ratio between the total kinetic energy in the accelerated propellant to the total input energy from the circuit. At an overhead level, this captures the fraction of energy imparted as work to the exhaust by the thruster. Using our formalism, we can write

$$\eta_e = \frac{m_i A_s \left[w_s(n_s v_s^2 + n_f v_f^2) + \int_0^t n_f v_f^2 \Delta v_{sf} H(\Delta v_{sf}) dt'\right]}{2(E_0 + E_{pi} + E_{cap})}, \tag{2.67}$$

where again the terms in the numerator, which we condense to a kinetic energy term E_{ke}, represent contributions from ions, fast neutrals, and slipped fast neutrals, respectively. We note that $\eta_R \approx \eta_m \eta_e$ in the limit $n_s \gg n_f$.

2.7 Results

We offer outputs from the single-pulse 1D model to build an intuition for simulation fidelity within the context of past PIT modeling efforts. Moreover, the HiPeR-PIT test article only produces plasma sheets for individual discharges in its current stage of development, so we also provide a foundation for theoretical and experimental comparisons in later chapters. By investigating the state variables that undergird current sheet dynamics seen below, we are able to closely consider how non-equilibrium ionization, a finite skin depth, and heating of the plasma electron population contribute to the formation and acceleration phases of inductive propulsion. Much of the analysis draws from Little *et al.* [58], where we derive a design criterion for sheet formation according to mass utilization scaling. This parameter appears again in steady-state and backfill modeling to understand whether the same nondimensional analysis can inform future test campaigns for multi-kW class PITs.

2.7.1 Model Outputs for a Single Case Study

We begin our analysis by commenting on the time-dynamic trends of a single set of results observed for a tractable set of design parameters at a high peak pressure. These conditions are listed in Table 2.2 and are referred to in this chapter as the baseline inputs for the single-pulse model. We consider an initial capacitor energy of 25 J ($C_0 = 2$ μF, $V_0 = 5$ kV) and an acceleration coil with inductance $L_c = 1$ μH, located 2 mm behind the gas injection plane. Throughout this thesis, we choose a coupling distance of $z_c = 4$ cm, consistent with measurements by Polzin [23]. This could be an optimistic metric given early estimations for HiPeR-PIT as we discuss later in Chapters 6 and 7. The injected neutral gas is assumed to have a peak value of $n_{n,0} = 4 \times 10^{20}$ m^{-3} and characteristic decay length of $z_n = 1$ cm. For the pre-ionized plasma, we set a low PI fraction of $\chi_0 = 0.01$ with $T_{e,0} = 20$ eV and $w_{s,0} = 2$ mm. In all results, we assume a recapture circuit architecture where the primary switch is closed at the first zero-crossing of I_c and the residual energy is totally recovered.

Fig. 2.4 provides the time-evolved state variables in the solution to our model for the

Table 2.2: Baseline input conditions for PIT case studies using the 1D single-pulse model.

Input	Value	Input	Value	Input	Value
V_0	5 kV	$T_{e,0}$	20 eV	$z_{s,0}$	0 m
C_0	2 μF	$T_{i,0}$	0.1 eV	$w_{s,0}$	2 mm
R_c	5 mΩ	T_n	0.026 eV	$n_{n,0}$	4×10^{20} m^{-3}
L_0	50 nH	r_o	10 cm	z_a	-2 mm
L_c	1 μH	r_i	3 cm	z_c	4 cm
χ_0	0.01	z_n	1 cm		

baseline input conditions. The horizontal axis shows time (t) normalized by the characteristic LC-period of the coil ($\tau_{LC} \approx 8.9$ μs) according to Eq. (2.60). Panels (a) and (b) confirm the expected behavior of an RLC circuit such that voltage decreases and coil current increases following switch closure and main bank discharge. Voltage and current are 90 degrees out of phase subject to Eq. (2.5), where the zero-crossing in V corresponds to a maximum value in I_c at $t/\tau_{LC} \approx 0.25$. We observe the subtle effect that neither V nor I_c are perfectly sinusoidal due to the presence of the plasma secondary, and confirm recapture at $t/\tau_{LC} \approx 0.5$ via the temporally truncated waveforms.

Azimuthal plasma currents arise from the mutual inductance between the elements of the lumped circuit model, characterized by Eq. (2.19). We observe a skewed rise rate in I_p due to a low initial M from the fact that the pre-ionized plasma is partly transparent to the electromagnetic fields generated by the current pulse ($\Theta_{e,0} \approx 0.84, k_0 \approx 0.16$). Panels (c) and (d) depict a rapid increase in M across $t/\tau_{LC} \in [0, 0.05]$ as the current sheet becomes more conductive and peak energy transfer takes place. The mutual inductance then experiences an exponential falloff as the translating plasma spatially decouples from the coil, given by panel (h).

The sheet parameters evolve substantially throughout the early stages of a pulse and give us the ability to delineate the formation and acceleration phases of PIT dynamics. The species densities, shown in Fig. 2.4(e), exhibit exponential increases during formation. A stark difference in the magnitudes of n_s and n_f means that ionization reactions dominated

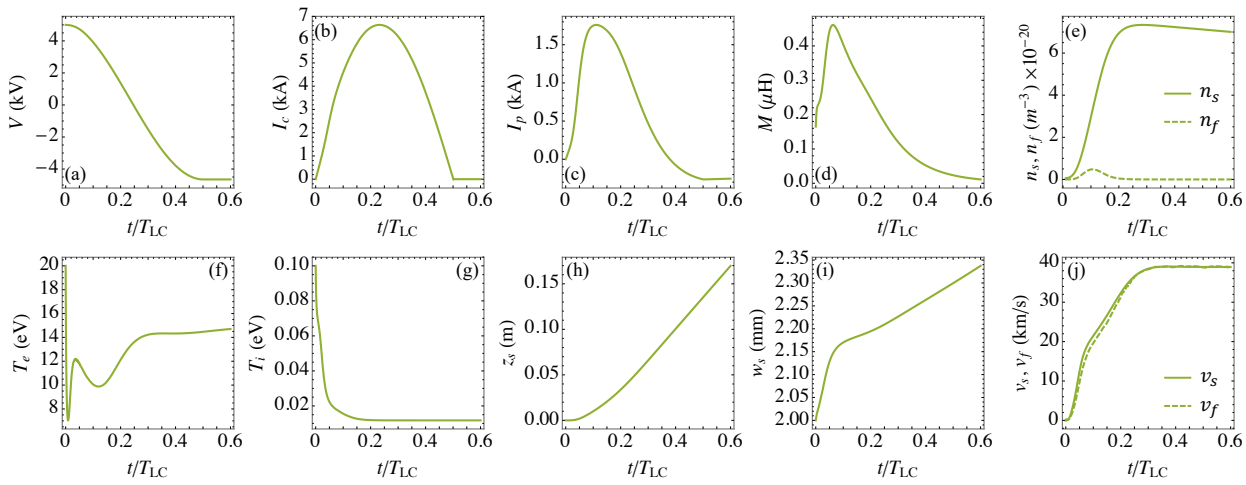

Figure 2.4: Time-dependence of single-pulse model state variables for the baseline input conditions listed in Table 2.2 (from [58]).

charge exchanges. CX collisions quickly subside as time progresses and neutral slip occurs, but n_s continues to grow from ionized and entrained neutrals. We confirm the importance of ionization in the formation phase of the pulse for $t/\tau_{LC} \in [0, 0.05]$ from the stunted axial motion of the plasma and the rapid growth in sheet width portrayed in panel (i). The background neutral and plasma sheet density profiles are also shown at different snapshots in time in Fig. 2.5, where the first row corresponds to the data in Fig. 2.4. Here, we see from the dashed $n_n(z,t)$ profile that a significant portion of the propellant gas is left in the wake of the exhausted plasma for these conditions. Once the Lorentz force dominates during the acceleration phase past $t/\tau_{LC} \approx 0.05$, we see the species velocities increase in panel (j) until they ultimately plateau, marking the decoupling time. By this point, diffusion processes drive a gradual increase in w_s and subsequent decrease in n_s due to slip.

Most notably, the dynamic time-evolution of electron temperature in Fig. 2.4(f) exhibits a back-and-forth competition between inelastic losses and Ohmic heating, given by Eqs. (2.33-34). The near-asymptotic drop in T_e immediately following switch closure can be attributed to ionization and radiation losses from the pre-ionized plasma reacting with the substantial

background neutral population peaking at $z = 0$. This trend reverses once Ohmic heating deposits energy into the electrons from a critical rise in I_p, and reverses again once a rising n_s drives greater inelastic losses. Past $t/\tau_{LC} > 0.15$, the current sheet is further from the coil face in a region of reduced neutral density (i.e. $z_s > z_n$) and Ohmic heating raises T_e once more. Slight changes in electron temperature beyond the coupling region occur due to residual plasma currents and cooling from diffusive expansion. Ion temperature found in panel (g) is far less dynamic, showing a monotonic decline throughout the pulse as $T_i \to T_n$. Coulomb heating of the ions is therefore negligible to the thermal energy of the population compared to the introduction of cold ions via the entrainment of background neutrals.

2.7.2 Multiple Case Studies

The case study in the previous section demonstrates the deterministic importance of processes in the formation phase to the ultimate entrainment of propellant gas. Knowledge of these early pulse dynamics informs the variables underlying system performance, and is therefore useful for the optimization of PIT efficiencies. In Little *et al.* [58], we have speculated that these processes are strongly influenced by the properties of the pre-ionized plasma and the rate of ionization relative to the rise rate of coil current. By sweeping $\chi_0 \in [0.01, 1]$ and $L_c \in [0.1, 10]$ μH, the following insights were offered from the model:

1. Increased pre-ionization fraction improves propellant mass utilization at the expense of electrical efficiency, given by Eqs. (2.66) and (2.67), respectively.

2. Decreased current rise times (i.e. smaller L_c, increased RLC damping ratio) also improves mass utilization at the expense of electrical efficiency.

3. Electrical inefficiencies introduced by decreasing the current rise time are less severe than those introduced by increasing χ_0.

We delve further into the effects of these two input parameters to show that formation and

acceleration dynamics as well as sheet transparencies can vary widely across single pulses, proffering cumulative effects across multiple pulses in high-repetition operating modes.

Influence of Pre-Ionization

Similar to the schematic in Fig. 2.3, we idealize the current sheets in Fig. 2.5 as step functions of height $n_s/n_{n,0}$ with darkening color gradients to reflect the entrainment of ambient neutral particles over time. The shape of the neutral profile in the wake of the plasma is given by the dashed curve, which deviates from the initial background density based on how effectively the sheet incorporates propellant gas. By toggling χ_0, we find that the composition of the sheet at the moment of capacitor discharge significantly influences the behavior of the exhaust over the LC-period of the coil. The time-dependent solutions depicting this in greater detail are given in Fig. 2.6.

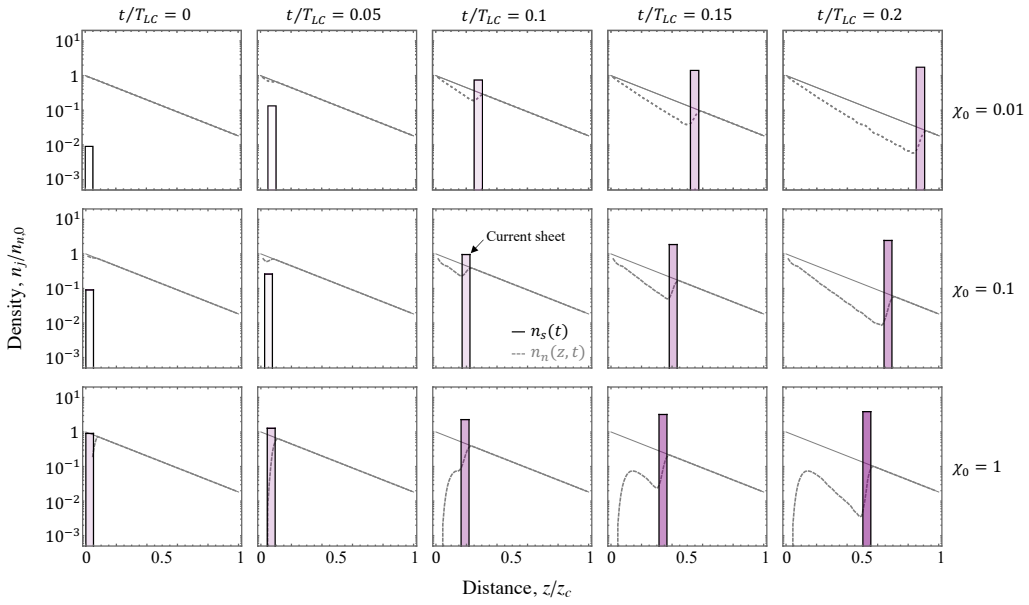

Figure 2.5: Instantaneous density plots of current sheet models for variable pre-ionization fraction (from [58]). Data is generated from the baseline input conditions listed in Table 2.2, except for a changing χ_0.

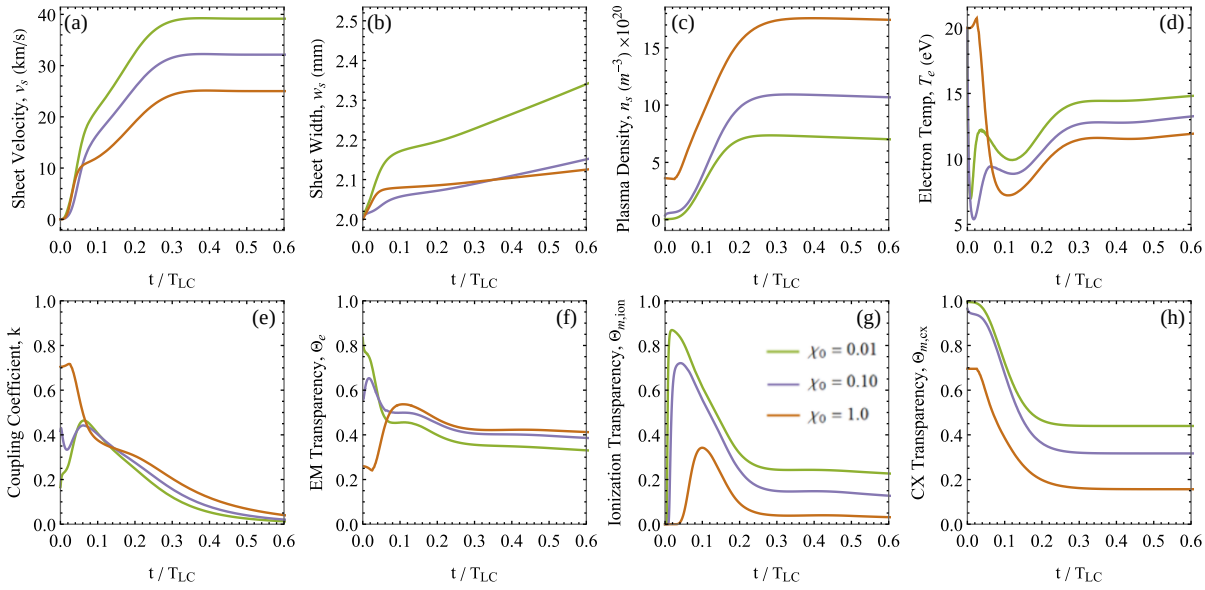

Figure 2.6: Time-dependence of state variables and transparency parameters critical to sheet formation and mass entrainment for variable pre-ionization fraction (from [58]). Data is generated from the baseline input conditions listed in Table 2.2, aside from χ_0.

We observe in panels (a) and (c) of Fig. 2.6 that lower pre-ionization yields a faster-moving current sheet that leaves a greater ratio of propellant gas unincorporated in the exhaust. As aforementioned, higher χ_0 drives better mass utilization efficiency, which is qualified by higher n_s for the same injected mass bit. Eq. (2.28) explains this phenomenon through the lens of momentum transfer by identifying that greater sheet densities imply higher collisional drag forces. A slower-propagating sheet experiences more charge exchanges and ionization reactions, which we can visualize according to lower mass transparencies in plots (g) and (h). As χ_0 increases, $\Theta_{m,ion}$ and $\Theta_{m,cx}$ both decrease and approach the snowplow model in the limit $\Theta_m \to 0$. The time histories of the mass transparency parameters scale inversely with n_s for $\chi_0 = 0.01$ and $\chi_0 = 0.1$, which can be explained by the increased probability of entrainment for denser plasma sheets. Total pre-ionization exhibits different behavior in the formation phase, where the electrons ionize almost all of the neutral particles encountered

by the sheet for $t/\tau_{LC} < 0.05$. This quenches T_e on a slightly different timescale, seen in (d), reducing S_{ion} enough so that the sheet becomes partly transparent during acceleration before Ohmic heating and residual currents restore $\Theta_m \approx 0$. The same trend is displayed in the shape of the residual neutral gas distribution in the bottom row of Fig. 2.5.

Fig. 2.6(d) also explicates the differences in energy loss modes for varying pre-ionization fractions. The low ($\chi_0 = 0.01$) and partial ($\chi_0 = 0.1$) pre-ionization cases experience an immediate drop in T_e once the switch closes as ionization and radiation losses dominate. The lower sheet density associated with $\chi_0 = 0.01$ allows T_e to recover faster because Ohmic heating deposits greater energy per electron, leading to the lowest effective ion energy cost. Noting that v_s scales inversely with χ_0, we surmise that pre-ionization increases the energy lost to ionization and radiation relative to the kinetic energy of the exhaust, which damages η_e. Stronger coupling between the inductive coil and the plasma also lends itself to smaller skin depth and Θ_e. Higher χ_0 leads to a lower plasma conductivity and consequently increases transparency to electromagnetic fields, but does not substantially affect η_e because we have assumed a small value of R_c.

Influence of Coil Inductance

We have previously discussed the importance of current rise time in the context of PIT performance as it impacts the formation of a uniform plasma sheet [7, 44]. In a parallel line of analysis as before, we examine the time-dynamic implications of varying current rise time by adjusting the inductance of the drive coil. Fig. 2.7 shows an entrainment diagram similar to Fig. 2.5 at four values of L_c, where the third row matches the baseline input conditions. We maintain low ($\chi_0 = 0.01$) pre-ionization across our new data sets to isolate L_c, and give time-dependent state variable evolutions in Fig. 2.8.

The instantaneous density plots in Fig. 2.7 depict better propellant mass entrainment for lower L_c values and lower current rise rates. This is corroborated by the mass transparencies shown in Fig. 2.8(g)-(h), which indicate that ionization and charge-exchange mechanisms are strongly influenced by coil design. The dashed curve representing $n_n(z,t)$ in Fig. 2.7 sharply

declines to zero for $L_c = 0.1$ μH, depicting snowplow behavior across most of the pulse. On the opposite end of the spectrum, $L_c = 5$ μH generates an almost nonexistent current sheet, which accelerates before creating a substantial plasma as we note from Fig. 2.8(c). Panels (a) and (b) inform us that this high inductance case solves for abnormally high v_s and w_s, and (e) shows minimal coupling. Hence, a threshold for sheet formation exists for cases where the current rise time exceeds the residence time of the plasma.

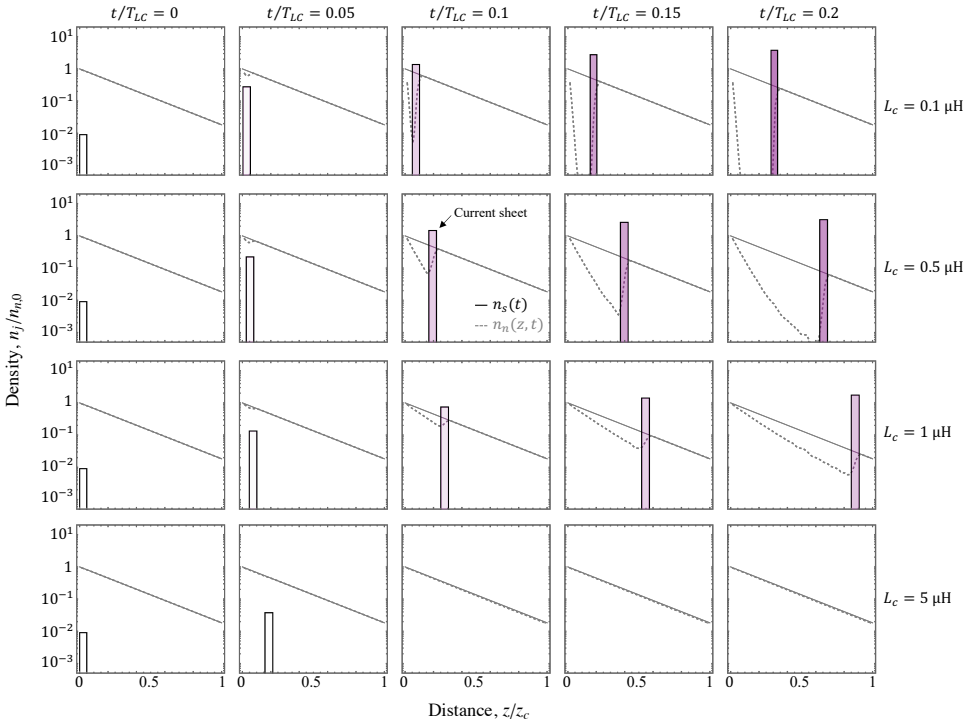

Figure 2.7: Instantaneous density plots of current sheet models for variable coil inductance (from [58]). Data is generated from the baseline input conditions listed in Table 2.2, aside from L_c. Note that bottom row ($L_c = 5$ μH) shows minimal current sheet formation.

We also observe significant effects on sheet dynamics with respect to electron temperature, coupling, and the ability of AC fields to permeate the plasma. The results are consistent with an a priori understanding of current rise time such that Ohmic heating outpaces ionization

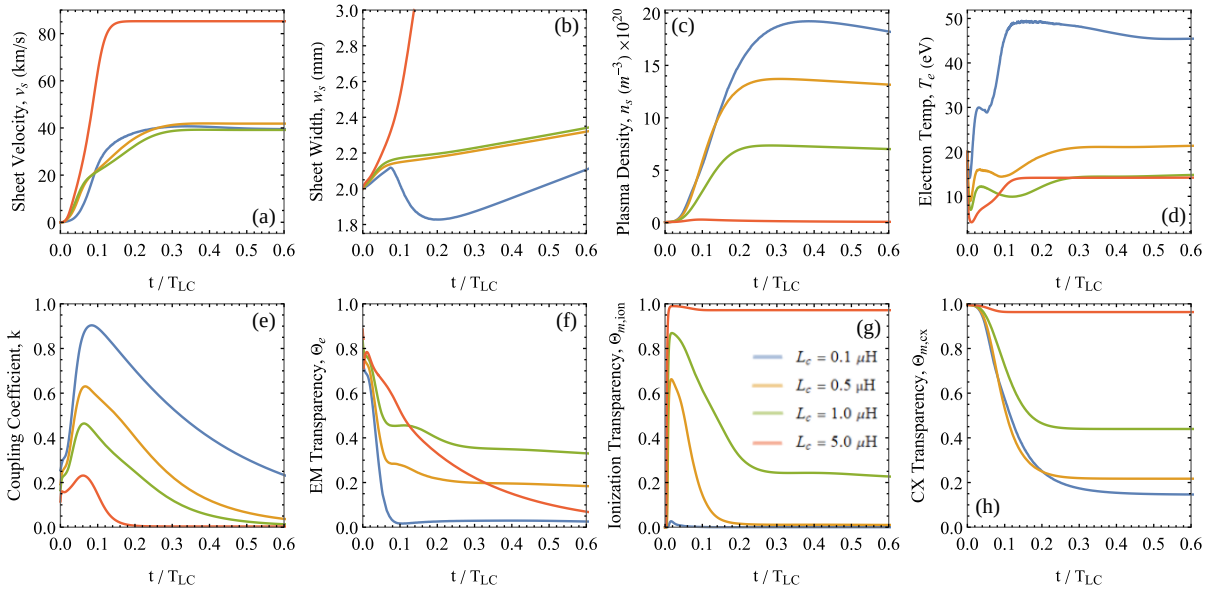

Figure 2.8: Time-dependence of state variables and transparency parameters critical to sheet formation and mass entrainment for variable coil inductance (from [58]). Data is generated from the baseline input conditions listed in Table 2.2, aside from L_c.

losses for lower L_c. The rise in T_e for $L_c = 0.1$ μH is significant enough to increase the plasma conductivity to where $\delta_s < w_s$ at $t/\tau_{LC} \approx 0.1$, meaning that entrainment occurs in the skin layer of the plasma (see Section 2.6.6). This corresponds to complete EM impermeability ($\Theta_e \to 0$) and a peak value near unity for k. A high final T_e value is indicative of unrecovered thermal energy in the sheet, decreasing η_e.

In the design space of coil inductance, extremely low L_c on the order of 10^{-7} H is difficult to achieve for smaller PIT geometries [41]. We find that $L_c \in [0.5, 1]$ μH is a favorable middle ground for the initial conditions listed in Table 2.2 since the plasma becomes largely impermeable to propellant mass anyway. Ionization still dominates CX collisions, and the balance of electron heating and cooling signals efficient discharge characteristics.

2.7.3 Propellant Comparison

Our two atomic propellant models allow us to build a physical intuition of the dynamics that occur during the early formation and acceleration of a current sheet for varying microscopic processes. We anticipate significant differences in thruster performance when operating at the same circuit parameters given changes to atomic weight, collision frequencies, reaction rates, interactional cross sections, and energy barriers. These develop the model at all levels; particularly through energy exchanges, power losses, and diffusion mechanisms.

In Fig. 2.9, we share the temporal progressions of significant state variables as before and use sheet transparencies to pinpoint underlying changes that could contribute to the performance discrepancies discovered by Dailey and Lovberg [8, 9]. Previous PIT research has broadly identified microscopic variations in the energy sinks of different propellants as the primary culprit behind behavioral dissimilarities [13], which we can now examine over the duration of a pulse.

The data shown reflect the same baseline input conditions, isolating the propellant variable for a 25 J capacitor at low ($\chi_0 = 0.01$) pre-ionization and intermediate ($L_c = 1$ μH) coil inductance. The solutions to our model in plots (a) and (b) show that argon yields a faster and wider current sheet, which logically follows from its smaller atomic weight. We apply the same electrical input to the coil from the PPU, so if work transfer takes place on similar scales in the plasma secondary, we confirm that the kinetic energy balance will retard the xenon exhaust. We find that xenon undergoes less diffusive expansion while collecting a much higher plasma density, proffering significantly higher η_m. The tremendous increase in xenon n_s due to collisions during the acceleration phase slows the sheet further, allowing the plasma to remain coupled to the coil for a longer duration, shown in (e).

The relative increase in coupling duration is a determining mechanism for other parameters in the system. Since the formation of the xenon plasma takes longer than argon, the model predicts higher peak k and T_e values. The xenon plasma is conductive enough so that Ohmic heating deposits more energy into the electron population over time and experiences

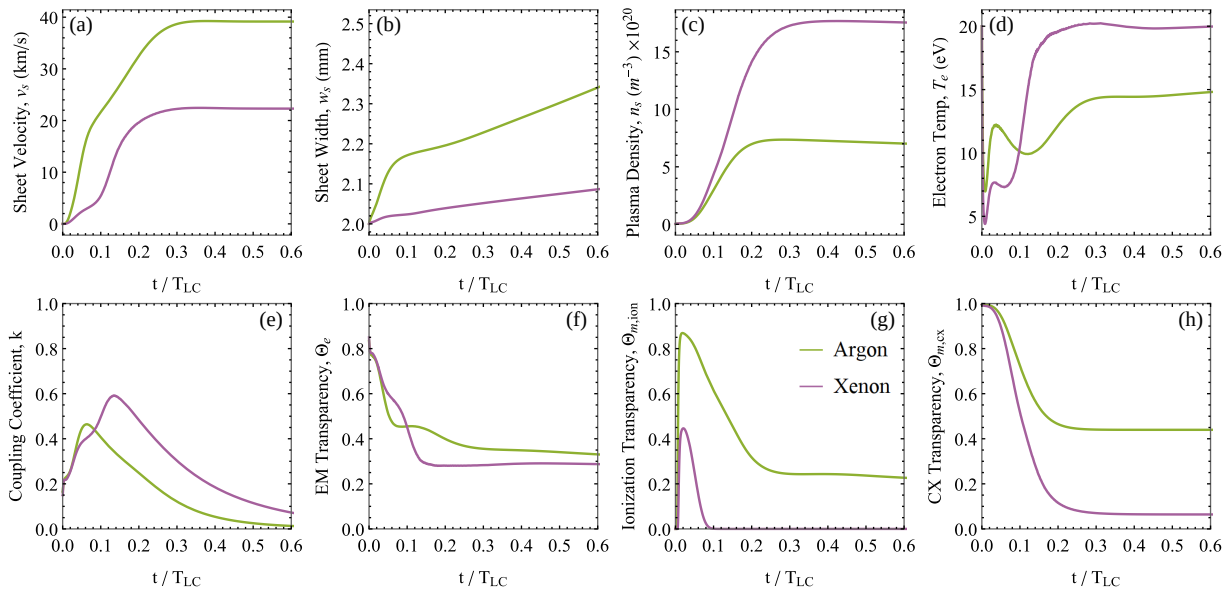

Figure 2.9: Time-dependence of state variables and transparency parameters critical to sheet formation and mass entrainment for argon and xenon propellants. Data is generated from the baseline input conditions listed in Table 2.2. Note that the argon model shows the same output as Fig. 2.4.

fewer inelastic losses. This portends an electrical inefficiency such that heavier propellants develop greater thermal sinks, but panel (f) also shows us that xenon becomes more impermeable to the AC fields of the coil on a shorter timescale than argon. This, combined with snowplow-like mass entrainment in the limit $\Theta_m \to 0$ for both ionization reactions and CX collisions past $t/\tau_{LC} \approx 0.1$ and 0.2, respectively, indicates a well-formed current sheet for this particular set of input parameters. The ability of our model to capture these physics on microsecond timescales will allow future circuit optimization for different propellant gas selections.

2.7.4 Dimensionless Parameters

Several fruitful efforts to nondimensionalize the governing equations for a 1D PIT model have identified scaling parameters influencing the performance of inductive accelerators [2,7,22,23,

38]. The physical importance of these parameters represents an ongoing study which, until now, has ineffectively captured the nature of propellant mass utilization. Since our model is capable of tracking variable entrainment across the time-duration of a pulse, we are able to formulate a design parameter for current sheet formation under non-equilibrium conditions. Here, we summarize and add to the mass utilization analysis of Little *et al.* [58] and compare our dimensionless results to past work. This situates our multi-pulse and backfill studies by prefacing the effective formation of current sheets subject to a spatially-constant ambient neutral gas distribution.

Dynamic Impedance and Critical Resistance Ratios

A few known parameters relevant to our study are dynamic impedance (α) and critical resistance ratios (ψ_1, ψ_2). Initially drawn from gas-fed PPT literature [1], the former identifies how well the circuit transfers energy to the plasma before it decouples from the coil, and the latter two control the nature of the current waveforms. The resistance ratios are defined as

$$\psi_1 = R_c\sqrt{\frac{C_0}{L_0}}, \qquad \psi_2 = R_p\sqrt{\frac{C_0}{L_0}} \tag{2.68}$$

and the dynamic impedance parameter is defined in terms of measurable quantities

$$\alpha = \frac{C_0^2 V_0^2 L_c}{2 m_{bit} z_c^2}. \tag{2.69}$$

Polzin [7] has found that there exists an optimum range, $\alpha \in [1, 5]$ for $\psi_1, \psi_2 \approx 0.1$, which maximizes the kinetic energy of the plasma and η_T. We look to confirm this finding in our sheet formation analysis to ensure that our model is consistent with past work in performance scaling.

Sheet Formation and Mass Utilization Scaling

The neutral gas breakdown threshold represented by a minimum coil current rise rate ($dI_c/dt|_{t=0} = V_0/L_c$) formulated by Polzin [7] motivates us to incorporate physical infor-

mation associated with the plasma formation phase to characterize a well-formed current sheet. A lower empirical breakdown threshold was proposed for PIT designs employing a pre-ionization scheme, but since there are notable differences between gas breakdown mechanisms and sheet formation processes, we generalize to the terms used in our model.

In our analysis thus far, the single-pulse results emphasize the importance of energy deposition in the electron population during the formation phase, as the relationship between electron-impact ionization and mass entrainment is explained in Eq. (2.25). Ionization of a neutral propellant in the absence of an energy source quenches the electron population and ultimately generates a plasma transparent to downstream particles, degrading η_m and η_T. The efficiency of the formation process should therefore hinge upon the ratio of energy deposited in the electrons to the energy required to ionize the propellant gas. This semi-empirical argument lends the dimensionless parameter

$$\Omega \equiv \frac{E_h}{E_{ion}} \tag{2.70}$$

where

$$E_h = \int_0^{\tau_{dc}} R_p I_p^2 dt \tag{2.71}$$

is the amount of energy deposited in the electron population by Ohmic heating and

$$E_{ion} = \frac{m_{bit}\bar{\varepsilon}^*_{ion}}{m_i} \tag{2.72}$$

is the energy required to fully ionize the mass bit. Within these terms, τ_{dc} denotes the plasma decoupling time and $\bar{\varepsilon}^*_{ion}$ refers to the average ionization energy. We note that Eq. (2.70) is a nondimensionalized form of Eq. (2.32), which allows us to ultimately arrive at the approximation

$$\Omega \approx \frac{m_i z_c \bar{R}_p V_0}{2\bar{\varepsilon}^*_{ion} L_c}\sqrt{\frac{\bar{k}^3 C_0}{m_{bit}}}. \tag{2.73}$$

Several assumptions are made in arriving at Eq. (2.73), which are explained in depth by Little *et al.* [58]. Most importantly, we note that Ω contains many of the same design variables as α since these terms are subsumed by the scaling of τ_{dc}, and Ω also varies directly with $dI_c/dt|_{t=0} = V_0/L_c$. Based on our analysis of the influence coil inductance, we predict thermal quenching of the electrons for $\Omega \ll 1$, implying poor mass utilization. In the opposite limit of high Ω, ionization supports a better η_m, but must still be balanced with electrical efficiency to reach a favorable η_T.

Returning to our model results, we sweep a variety of input conditions to assess the legitimacy of Ω as an indicator of well-formed current sheets. To do so, we examine trends of η_m versus V_0 to reflect the adjustment of a PPU voltage across a test campaign. This data is depicted as discrete points in Fig. 2.10, which represent the values of η_m taken at t_{max}. Parameter changes are listed within the panels themselves, but the (black) baseline corresponds to the conditions listed in Table 2.2 at a lower inductance value of $L_c = 0.2$ μH.

Across five input parameters, Fig. 2.10 exhibits a sharp increase in η_m with rising V_0 up to a threshold voltage (V_0^*), after which a gradual leveling toward an asymptotic value is observed. Panel (a) indicates that V_0^* increases as the coil is positioned further behind the gas injection plane due to a decrease in $\bar{k}$. Panels (b)-(d) tell us that V_0^* has a direct relationship with L_c, but an inverse relationship with z_c and C_0. We can explain this phenomenon using Eq. (2.73) by adjusting V_0 in order to compensate for other variable changes to maintain a constant Ω. Finally, $n_{n,0}$ exhibits a direct relationship with V_0^* because it is analogous to m_{bit} for a single pulse.

Fig. 2.10(f) amalgamates the data from the other five input control sweeps and plots η_m versus Ω on a logarithmic scale. Results shown represent approximations from Eq. (2.73) using the simplifying assumptions: $\bar{k} \approx k_0, \bar{R}_p \approx R_{p,0}$, and $\bar{\varepsilon}^*_{ion} \approx \varepsilon^*_{ion}(T_{e,0})$. The graph indicates that mass utilization collapses onto a single curve of $\sim 20\%$ spread, which emphasizes that Ω can act as a scaling parameter for current sheet formation in PITs with reasonable consistency. It is also promising that there is an apparent "knee" in the curve at $\Omega^* \approx 1.5$, signifying a critical design value for efficient operation.

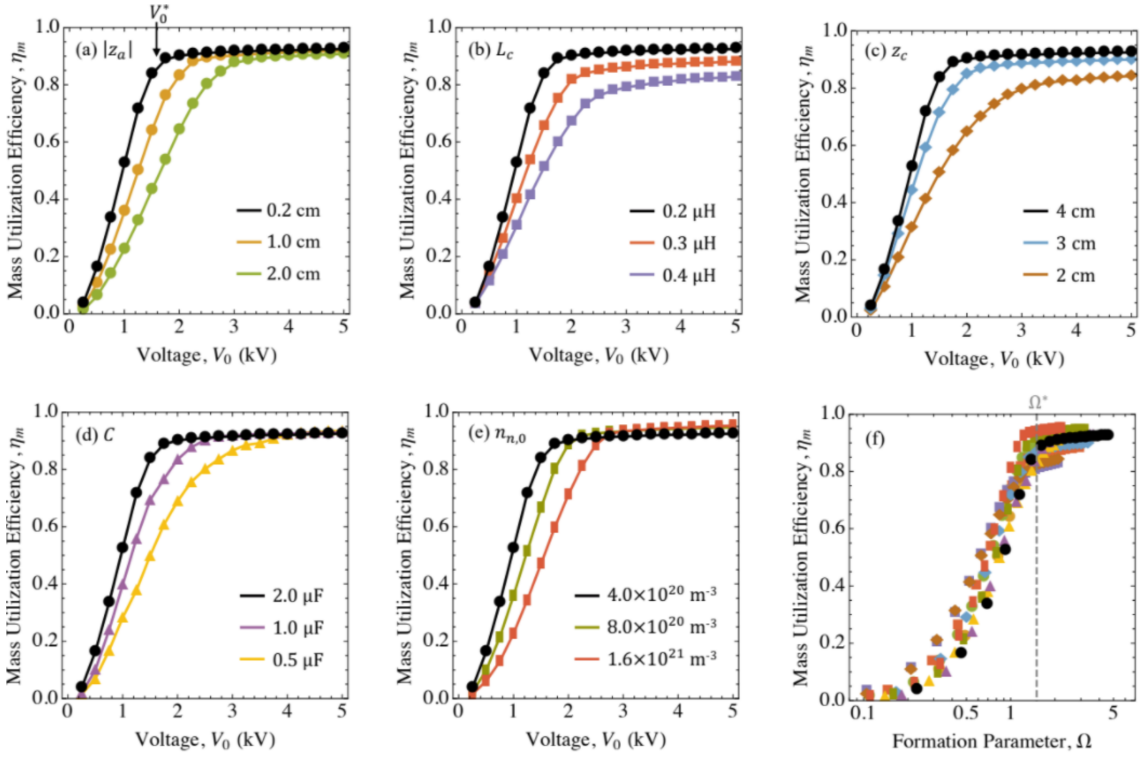

Figure 2.10: Dependence of mass utilization efficiency on initial capacitor charge voltage for various input parameters. The (black) baseline case corresponds to data generated from the conditions listed in Table 2.2, except here $L_c = 0.2$ μH. Each panel shows deviations from the baseline for different variables, except for the bottom right which depicts the critical formation parameter, Ω^* (from [58]).

We compare Ω to the dynamic impedance parameter for the same eleven data sets in Fig. 2.11 to further analyze the critical formation threshold. Panel (c) explains that α is not formulated to scale with η_m since results do not condense to a single curve, even though the individual data trends resemble the shape of those in Ω. Fig. 2.11(b) depicts a strict exponential relationship between α and Ω below Ω^*, with nonlinear behavior appearing above the critical formation threshold. This means that well-formed current sheets exhibit more dynamic coupling with the coil, likely due to the nonlinear deposition of energy into the electron population.

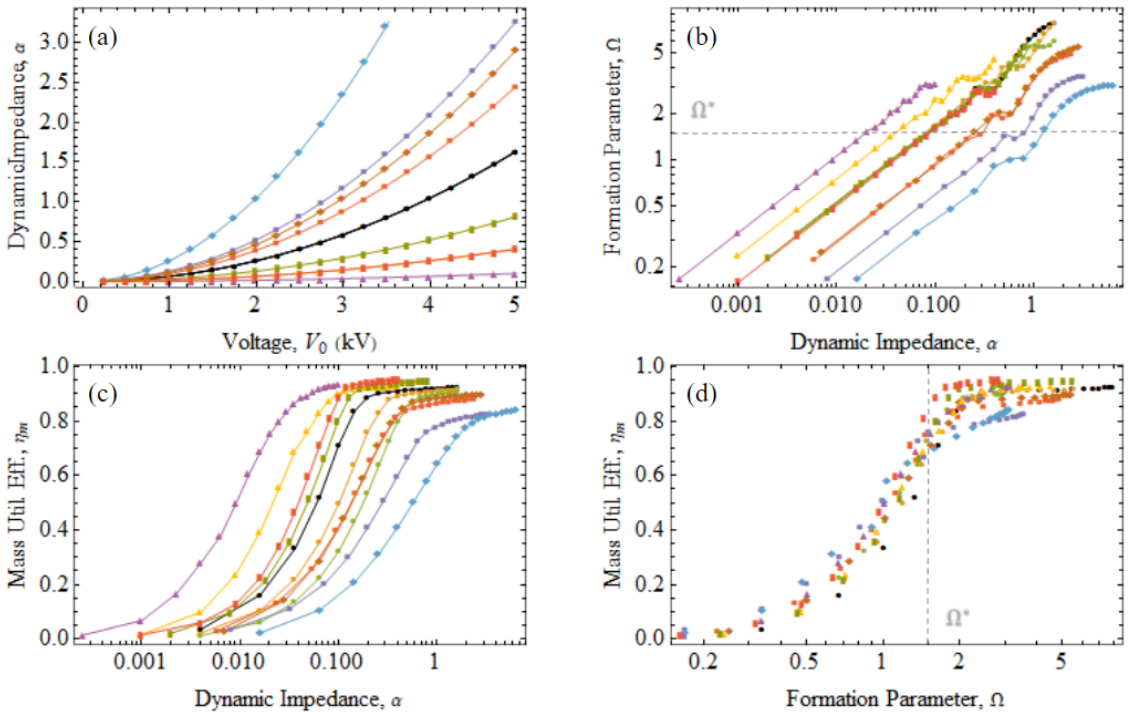

Figure 2.11: Comparison of the proposed formation parameter to the subsumed dynamic impedance metric, where data shown matches that found in Fig. 2.10. Note that panel (a) shows fewer curves because α has no dependence on z_a.

These results combine to reinforce Ω^* as a possible physical interpretation for Polzin's coil current rise rate requirement [7] based on data obtained from the FARAD proof-of-concept experiments [23, 40]. Although current sheets were observed to form, measurements found that the plasma remained partly transparent to both the EM fields of the coil and downstream propellant mass. A quick calculation by Little *et al.* [58] using the input conditions from [23] confirmed that the FARAD experiment operated at a maximum value of $\Omega \approx 1.1$, corresponding to $\alpha \approx 3, \psi_1 \approx 0.9$, and $\psi_2 \approx 0.2$. Examination of Fig. 2.10(f) suggests that this would yield a partially transparent plasma in accordance with the critical formation threshold even while operating in the optimum range of α and ψ_1, ψ_2.

2.7.5 Summary of Results

In this chapter, we analyze solutions to the single-pulse model for thruster input conditions in the expected operating range of a multi-kW class PIT with pulsed gas injection. Our results are used to develop an intuition for the impacts of pre-ionization and coil inductance on the formation and acceleration of current sheets by examining the dynamic energy transfers between fluid species. Argon and xenon propellants are compared to demonstrate model consistency across different noble gases, and scaling laws are constructed to find efficient thruster design spaces. Understanding the process of inductive current sheet formation at a more fundamental level is essential to the multi-pulse optimization of PITs and can provide deeper insight into plasmas observed in our solar system [64] and stellar bodies [65]. The primary results of this single-pulse study are listed below:

- Sheet parameters evolve substantially throughout the early stages of a pulse and exhibit a clear delineation between formation and acceleration phases at fractions of the LC-period of the circuit.

- Electron temperature in the sheet displays rich dynamics at short timescales due to the competing effects of Ohmic heating and inelastic losses.

- Greater pre-ionization generates a current sheet more transparent to the AC fields of the coil carrying a severe η_e penalty, but with better propellant mass entrainment.

- Lower coil inductances substantially improve the coupling between the coil and the plasma leading to better mass entrainment and lower Θ_e. At high values of L_c, no current sheet forms, so we observe a threshold for sheet formation for cases where the current rise time exceeds the residence time of the plasma.

- Xenon proffers better sheet formation than argon for the tested parameter space because its higher atomic mass increases the plasma residence time, yielding greater electromagnetic work transfer. This comes at a price of greater thermal deposition.

- A dimensionless scaling parameter offered by Little *et al.* [58] is found to be an effective predictor of well-formed current sheets and offers a critical design threshold consistent with our model.

Chapter 3

STEADY-STATE MODEL OF MULTIPLE-PULSE THRUSTER OPERATION

The modeling of current sheet dynamics at microsecond timescales for individual discharges offers the greatest predictive utility for understanding the in-space performance of IPPTs. It is assumed that successive ejected bodies of plasma do not electromagnetically interact while coupled with the thruster, even at high pules rates; hence, our 1D, single-pulse model constitutes the bulk of plasma physics presented in this thesis. We have constructed our model in such a way, however, as to meaningfully connect pulses to simulate an unsteady operating mode. By accounting for dynamic neutral fluid interactions and an evolved background density profile in both space and time, our formulation is uniquely capable of stitching together singular discharges for steady-state gas injection.

We outline an algorithm for connecting sequential pulses across shared design conditions for a changing ambient neutral density distribution. The multi-pulse model accommodates diffusion processes and neutrals left uncollected by preceding plasma sheets to be broadly applicable under anticipated experimental conditions. This allows us to substantively draw comparisons between steady-state operation and testing in a finite neutral backfill, presented in the next chapter. Here, we describe theory, limitations, and stand-alone results for inputs that proffer state variables consistent with the assumptions made in Chapter 2 and contrast them with the outputs of the single-pulse code.

3.1 Inter-pulse Model

Since the single-pulse model is responsible for describing the formation and acceleration of individual current sheets, a steady-state model only needs to capture the change in conditions

between pulses at adequate timescales. The final state of the inter-pulse evolution is then passed into the following single-pulse calculation as the initial conditions at $t = 0$. Each pulse is bounded by the same t_{max} so we specify the number of pulses to cap the total runtime. To simplify the execution of many pulses in tandem, we assume fixed initial conditions for the circuit, coil geometry, propellant, and pre-ionized plasma. This is representative of an engineering design goal for an in-space mission, which will want to keep device specifications constant over the lifetime of the thruster to bolster system reliability.

3.1.1 Additional Inputs

As mentioned, we include the number of pulses (N_p) as one of the model inputs. We can monitor the number of pulses required to reach a quasi-steady state for a certain set of ICs by modifying this parameter and assessing the performance metrics within a given tolerance, which we discuss further in Section 3.3.

We also specify the pulse repetition frequency (f_{rep}), which represents the number of times the switch ahead of the drive coil will close per second. In Chapter 1, it is mentioned that rates on the order of $1-10$ kHz would be required to reach optimal recapture efficiencies for the coupling distances found thus far for multi-kW power class IPPTs [39]. We convert this repetition rate to a repetition period ($t_{rep} = f_{rep}^{-1}$) over which to evaluate the inter-pulse model. Values for t_{rep} used in our analysis therefore range from $0.1 - 1$ milliseconds.

3.1.2 Background Neutral Density Update

We exploit the fact that $n_n(z, t)$ is a bivariate function to evolve the density profile of slow-moving background neutrals in both parameter spaces. To do so, we numerically solve the neutral continuity equation across the full axial span of the simulation (z_{max}) and repetition period (t_{rep}). This is a partial differential equation (PDE) where the initial condition is the spatial neutral density function evaluated at the end of the j^{th} pulse, $n_{n,j}(z, t_{max})$, and the boundary condition (BC) is the peak neutral density at the coil face as a constant function in time. That is,

$$\text{PDE}: \quad \frac{\partial n_n(z,t)}{\partial t} = -c_{s,n}\frac{\partial n_n(z,t)}{\partial z} + D_n\frac{\partial^2 n_n(z,t)}{\partial z^2} \tag{3.1}$$

$$\text{IC}: \quad n_n(z,0) = n_{n,j}(z,t_{max}) \tag{3.2}$$

$$\text{BC}: \quad n_n(0,t) = n_{n,0} \tag{3.3}$$

where $c_{s,n}$ is the neutral sound speed and D_n is the neutral diffusivity coefficient. The solution to this system gives the initial neutral density profile for the subsequent pulse, $n_{n,j+1}(z,0)$, which replaces the form seen in Eq. 2.56. The first and second terms on the right-hand side of the continuity equation represent the displacement of background neutrals due to axial translation and the source term from gas diffusion, respectively. The neutral sound speed, $c_{s,n} = \sqrt{e_c T_n/m_i}$, is also seen in the coefficient equation [59, 66],

$$D_n = \frac{\pi^{1/2} c_{s,n}}{n_{s,j}\sigma_{cx} + n_{f,j}\sigma_{qm}} \tag{3.4}$$

where σ_{qm} is the ion-neutral momentum transfer cross section, which we fix at 1.57×10^{-18} m^2 for argon [67] and 3×10^{-19} m^2 for xenon [68]. For N_p pulses, we execute this interpulse update $(N_p - 1)$ times and store the state variables and performance metrics for each pulse as separate data sets.

3.2 Assumptions and Limitations

A complete model of the inter-pulse physics and changes to the background neutral density distribution would require a greater working knowledge of gas kinetics in the test environment. Diffusion is an inherently probabilistic random-walk process, but expansion beyond the outer radius of the thruster is ignored. In this way, our model overpredicts the impact of a changing ambient gas profile for steady injection, but is consistent with the 1D equations we describe. We assume that the steady-state performance of the thruster matches the output data of the final pulse of the simulation once we locate a critical N_p value (if it

exists). We also assume that diffusion is a nondominant process such that $D_n \in [0, 1]$. From a computational perspective, this ensures that the inter-pulse density does not exceed the peak background density, $n_{n,0}$. We also assume that EM fields do not persist beyond the span of a main bank discharge, and have no effect on the inter-pulse physics.

With respect to experimental validation, multiple engineering advancements preclude testing at $f_{rep} \in [1, 10]$ kHz. Thermal loads on the PPU are particularly challenging to the HiPeR-PIT design, so this effort is speculative in its ultimate comparisons against a backfill. Future work extending this inter-pulse model to higher dimensions would require more boundary conditions, perhaps along the centerline of the thruster, which could be measured by an axial Langmuir probe.

3.3 Evolution of Neutral Density

In principle, all input conditions should eventually yield a steady state for fixed f_{rep} assuming constant gas injection [13]. However, by examining the pulse-to-pulse evolution of ambient neutral density profiles using the inter-pulse model, we can better understand why this is the case and how quickly certain input parameters lead to steady-state PIT operation. The latter will also inform the design spaces of future experiments to yield consistent current sheets with fewer total discharges.

3.3.1 Pulse-to-pulse Density Profiles

To start, we search for favorable input conditions using the multi-pulse model that align well with the available parameters in the HiPeR-PIT experiment. Those listed in Table 2.2 of the previous chapter yield poor multi-pulse performance metrics due to high characteristic ambient neutral density and coil inductance. Table 3.1 gives the baseline input conditions of the multi-pulse studies across Chapters 3, 4, and 5. Note that many parameters remain the same, but we lower capacitor voltage to $V_0 = 3$ kV, coil inductance to $L_c = 0.5$ μH, and peak neutral density to $n_{n,0} = 9.7 \times 10^{19}$ m^{-3}. This peak initial density value is consistent with a backpressure of $P_0 = 3$ mTorr via the ideal gas law, $P_0 = n_{n,0} k_B T_n$.

Table 3.1: Baseline input conditions for PIT case studies using the 1D multi-pulse model.

Input	Value	Input	Value	Input	Value
V_0	3 kV	$T_{e,0}$	20 eV	$z_{s,0}$	0 m
C_0	2 μF	$T_{i,0}$	0.1 eV	$w_{s,0}$	2 mm
R_c	5 mΩ	T_n	0.026 eV	$n_{n,0}$	9.7×10^{19} m^{-3}
L_0	50 nH	r_o	10 cm	z_a	-2 mm
L_c	0.5 μH	r_i	3 cm	z_c	4 cm
χ_0	0.01	z_n	1 cm	f_{rep}	10 kHz

We provide the input conditions for the 1993 experimental test campaign of the PIT MkV [8] in Table 3.2 to highlight a few of the blatant differences between MW-class inductive accelerators and those with lower discharge energies per pulse. The capacitor voltage, cross-sectional area, and injected neutral densities reveal the greatest disparities relative to Table 3.1 since a larger design allows for a more substantial mass bit. The coupling distance also increases, though it is estimated near the length of the conical injection pylon.

Table 3.2: Fixed and variable input conditions for the PIT MkV across multiple TRW test campaigns (from [8, 43]). z_a and f_{rep} are omitted since measurements are only given for singular pulses with downstream injection.

Input	Value	Input	Value	Input	Value
V_0	28 kV	$T_{e,0}$	10 eV	$z_{s,0}$	0 m
C_0	4.5 μF	$T_{i,0}$	0.95 eV	$w_{s,0}$	5 mm
R_c	5 mΩ	T_n	0.026 eV	$n_{n,0}$	5.8×10^{22} m^{-3}
L_0	80 nH	r_o	50 cm		3.5×10^{23} m^{-3}
L_c	0.66 μH	r_i	20 cm		9.9×10^{23} m^{-3}
χ_0	0.01	z_n	5 cm	z_c	7.5 cm

With this in mind, we anticipate model outputs that differ widely from some of the greater bodies of PIT data, but our goal is to examine trends at smaller scales that may be generalizable depending on temporal dynamics. Hence, while the magnitude of the neutral density distribution ahead of the drive coil is important, the shape is more significant to the

nature of our study. Fig. 3.1 depicts the initial neutral density curves ahead of each pulse in the baseline ($N_p = 6$) study using the model inputs found in Table 3.1. These profiles are shown on a logarithmic scale, where the form in Eq. (2.58) is given in blue representing the first pulse.

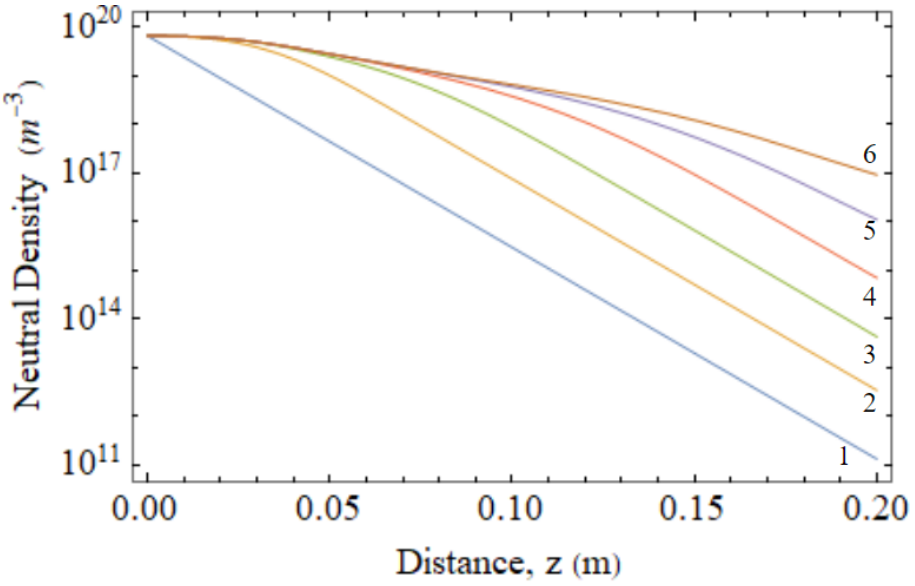

Figure 3.1: Spatial evolution of background neutral density, $n_{n,j}(z)$, for six pulses and five inter-pulse adjustments for the baseline input conditions listed in Table 3.1. The density profiles are labeled according to the input of the j^{th} pulse. This figure demonstrates the tendency of high-pulse-rate PITs to approach backfill conditions over many pulses.

We observe that the neutral density distribution levels out over the course of the simulation toward a more constant function in z, but maintains a monotonic decrease even in steady state. The pulse-to-pulse increase in $n_{n,j}(z)$ is attributable to the continuity term in Eq. (3.1), and the curves are smoothed by diffusion. It is critical to note that the density profiles become more tightly grouped with each pulse and maintain close agreement over longer stretches in z. This means that each successive current sheet experiences propellant mass entainment more comparable to that of steady-state operation. Hence, an increasing $n_{n,j}(z)$ is indicative of poorer entrainment for higher j. Fig. 3.1 tells us that greater quan-

tities of neutral particles are left uncollected by consecutive plasma sheets, auguring worse mass entrainment for multi-pulse operation. We note that this is broadly true across all input conditions we have observed for the model using argon propellant.

3.3.2 Reaching a Steady-state Operational Equilibrium

It is not immediately apparent by looking at Fig. 3.1 that the model has reached a steady state. Indeed, true steady-state operation would depict overlapping density profiles $\forall z \in [0, z_{max}]$, but for the purpose of efficient analysis, we can identify a critical value of N_p by comparing the model outputs from pulse-to-pulse and defining a change tolerance at which we say the final pulse represents an equilibrium. Since we assess the quality of well-formed current sheets via mass utilization scaling in Chapter 2, it follows that our definition of a steady-state equilibrium concerns the evolution of η_m. The error tolerance for changing mass utilization between pulses could scale with injected mass bit, but for the sake of simplicity we adopt the rule $\Delta\eta_m < \pm 1\%$ for all steady-state conditional arguments hereafter.

The rate at which the neutral density profile ahead of the thruster approaches a steady state for various ICs is a computationally-intensive line of inquiry for the multi-pulse model. However, we can distill the important parameter spaces based on the most easily controlled experimental conditions. We are particularly interested in the mass flow rate ($\dot{m}$) for inter-coil gas injection, which for our purposes depends on the size of the distribution channels seen in Fig. 2.3. In fluid mechanics, the mass flow rate is usually given by

$$\dot{m} = \rho A v, \tag{3.5}$$

but our model allows us to approximate according to

$$\dot{m} \approx m_{bit} f_{rep}. \tag{3.6}$$

Eq. (2.62) informs us that $m_{bit} \sim n_{n,0}$, so in order to examine different mass flow rates, we can sweep $n_{n,0}$ and f_{rep} in a 2D array. Fig. 3.2 shows the Boolean existence of a steady-

state equilibrium for six pulses across these two parameter spaces using the other baseline initial conditions in Table 3.1. By expressing this data in the form of a heat map subject to our chosen tolerance, we demonstrate that certain mass flows achieve steady-state operation more efficiently than others.

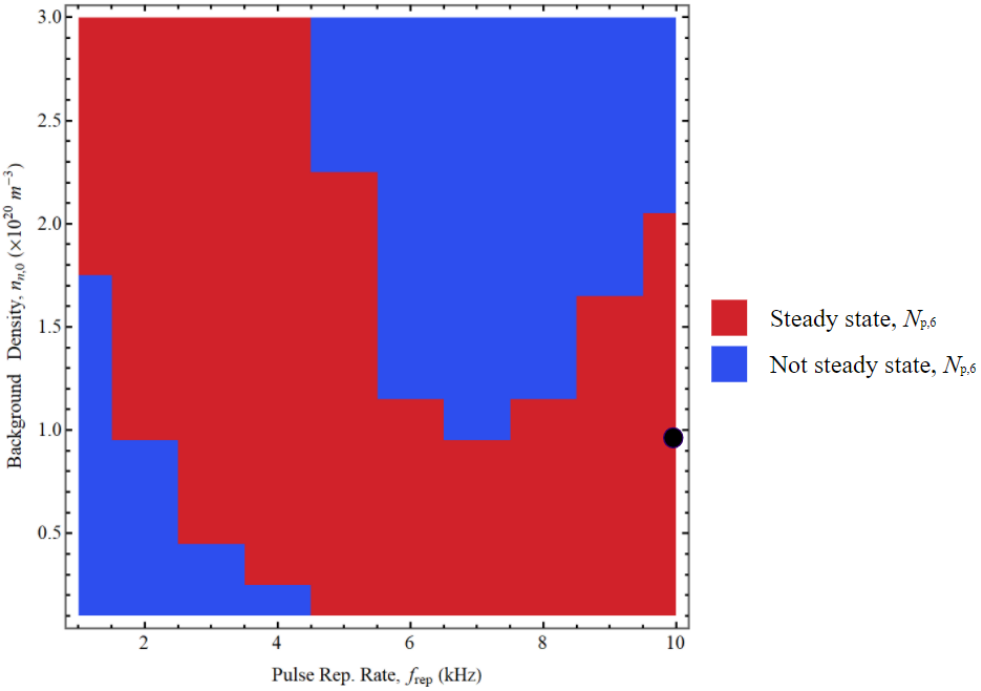

Figure 3.2: Existence of steady-state mass entrainment for six pulses across a mass flow rate parameter space subject to a 1% tolerance. f_{rep} and $n_{n,0}$ are swept across discrete intervals to simulate adjusting $\dot{m}$. The black dot indicates the base case consistent with Table 3.1. This figure demonstrates the relative rate at which a single set of circuit and plasma parameters can achieve a steady state using the multi-pulse model.

Across the swath of input conditions examined during the construction of this thesis, the model has predicted that most PIT designs will reach a steady state in six to eight pulses. Fig. 3.2 quantifies this claim by showing that certain mass flows proffer more consistent sheets by the sixth pulse such that, in general, $n_{n,0}$ scales inversely with f_{rep} to drive faster equilibrium settling times. This is likely because shorter pules periods require lower mass

bits to resolve the energy dynamics in the electron population. We observe that our baseline input conditions (black) fall comfortably within the steady-state region.

3.3.3 Multi-pulse Performance Contours

To better understand this mass flow parameter space, we can examine efficiency contours in a line of analysis similar to what Little *et al.* [58] have offered for the single-pulse model. Fig. 3.3 depicts η_R and η_m for the same solutions to the model shown in Fig. 3.2. We immediately notice that the contours lack smoothness, which could be attributable to a low step resolution in z and t, but could also indicate dynamic performance differences for the given input conditions. Fig. 3.3(a) shows a small band of optimum recapture efficiency $\gtrsim 20\%$ near the baseline conditions at high f_{rep} and $n_{n,0} \approx 10^{20}$ m^{-3}. This region corresponds to $\eta_m \approx 60\%$, which is sustained for $f_{rep} \in [4, 10]$ kHz.

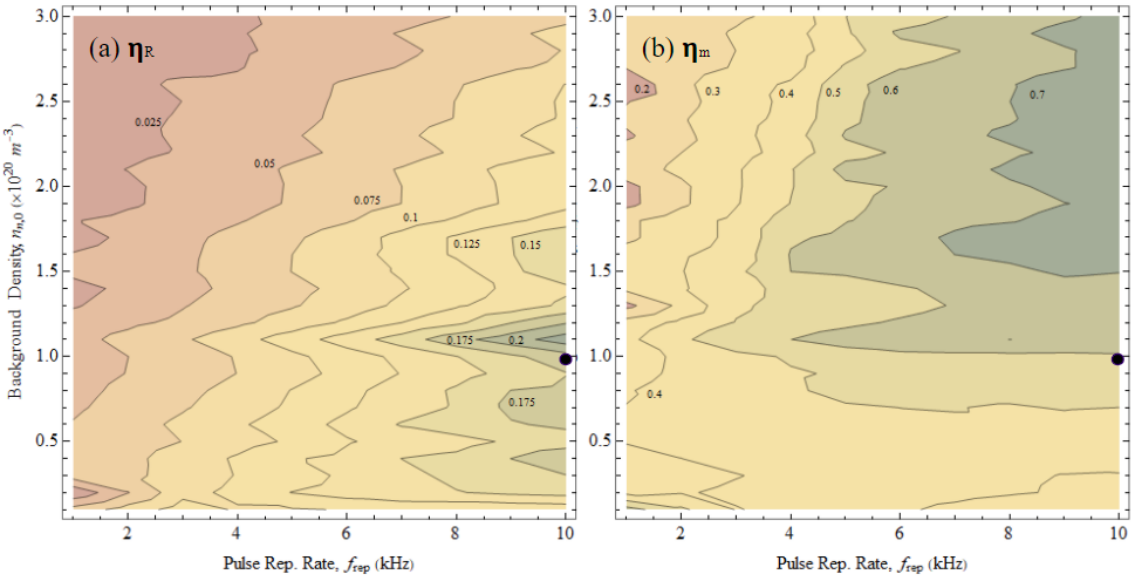

Figure 3.3: (a) Recapture and (b) mass utilization efficiency contours of the multi-pulse model across the same mass flow rate parameter space as Fig. 3.2. Green indicates a more efficient thruster, and the black dot corresponds to the baseline input conditions listed in Table 3.1. Time-dependent performance metrics at this point are shown in Fig. 3.5.

Fig. 3.3(b) finds that mass utilization is maximized for high ($n_{n,0} \gtrsim 1.6 \times 10^{20}$ m^{-3}) densities and high ($f_{rep} \in [8, 10]$ kHz) pulse rates. This is burdensome to the electrical efficiency of the system, however, which intuitively aligns with faster switching speeds and more particles to inductively accelerate. Hence, we find the optimum η_R band in panel (a). These findings combine with those from Fig. 3.2 to demonstrate that operating in higher mass entrainment regions requires more pulses to reach steady-state equilibrium. The low density, low pulse rate region in Fig. 3.2 that fails to reach steady-state in six pulses violates this rule, but this is likely attributable to other factors detailed in the next section, such as lower plasma densities and faster sheet velocities.

3.4 Results

Solutions to the multi-pulse 1D model have less experimental data available for validation, but are ultimately more indicative of the in-space operation of an IPPT. Our formulation allows us to analytically solve for the time-evolution of system state variables at each pulse, which enables a comparison between non-equilibrium and steady-state conditions. We anticipate that the development of a stable background neutral density profile influences the processes of ionization, electron heating, and sheet formation from pulse to pulse, so the following analysis will consist of time-dependent model outputs.

3.4.1 Transient and Steady-state Output Comparison

Since we have already discussed favorable parameter spaces in the previous section, we begin with a state variable overlay that contrasts the transient ($N_{p,0} = 1$) and steady-state ($N_{p,f} = 6$) model outputs at timescales critical to sheet dynamics. Fig. 3.4 gives the temporal functions relevant to sheet formation and mass entrainment across the first and final pulses for the baseline input conditions listed in Table 3.1. We observe substantial differences in each plot, demonstrating a wide gap between single-pulse and multi-pulse results for the same thruster circuit, geometry, gas properties, and pre-ionization level. Intermediate pulses are neglected for the sake of visual clarity.

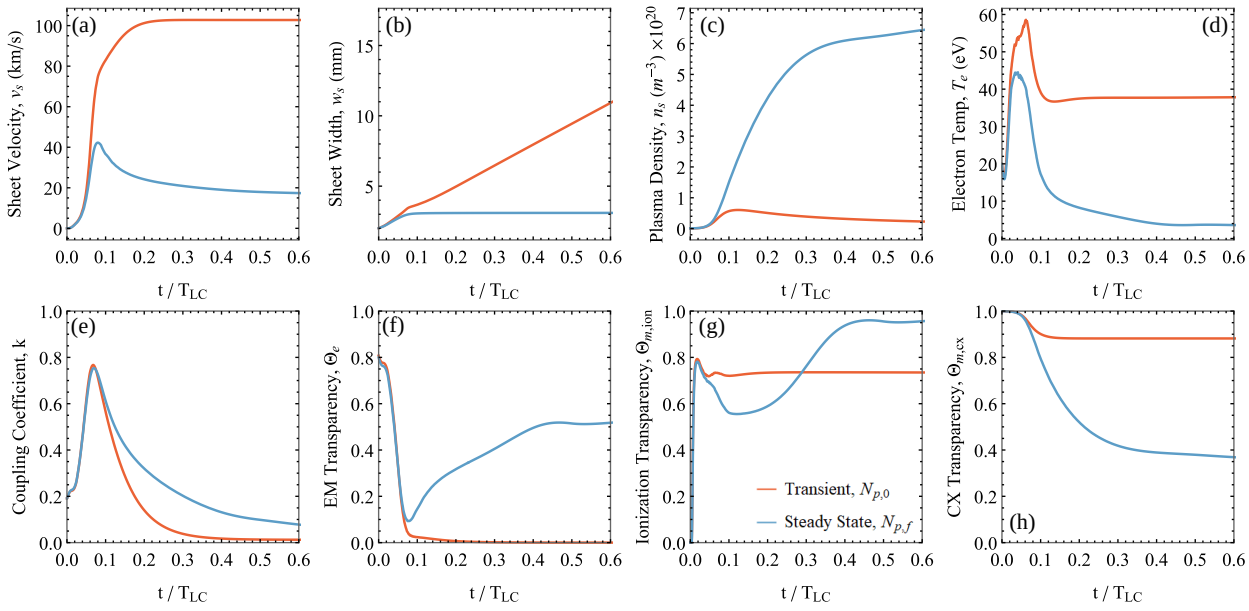

Figure 3.4: Time-dependence of multi-pulse model state variables for the baseline input conditions listed in Table 3.1 contrasting the first ($N_{p,0}$) and final ($N_{p,f}$) pulses.

Sheet velocity differs in both shape and magnitude according to Fig. 3.4(a), but exhibits close agreement throughout the formation phase for $t/\tau_{LC} < 0.1$. The steady-state sheet then peaks in v_s and begins to decelerate to a lower final value of ~ 20 km/s, whereas the transient sheet accelerates until it levels off in excess of 100 km/s. We see in panel (b) that the transient sheet continues to widen without bound, which (c) clarifies by showing n_s decreasing past the initial formation phase. This indicates that the first pulse never effectively achieves plasma formation per Eq. (2.39) because neutral slip stretches the skin depth throughout the pulse. The steady-state solution yields a more consistent sheet width and growing plasma density in time, which implies better formation and particle entrainment.

Other state variables confirm this finding by emphasizing different competing processes across the first and final pulses. The mass transparency parameters depicted in panels (g) and (h) indicate that the transient sheet is largely unaffected by ionization and CX collisions, whereas the steady-state solution shows a dynamic impermeability to both. We see that

charge exchanges dominate the reactions in the steady-state sheet, which tells us that the mechanisms driving efficient PIT operation change over time for high-pulse-rate modes - at least within the given regime. This follows from the increased presence of downstream neutrals highlighted in Fig. 3.1.

The electron population exhibits fewer dynamics but a greater peak temperature than before, which we can attribute to lower sheet density and plasma resistance per Eqs. (2.32) and (2.41). The first pulse encroaches upon the energy barrier of our model since we have neglected higher ionization states, and maintains a high asymptotic value of T_e due to minimal inelastic ionization and radiation losses past the acceleration phase. The steady-state solution shows almost complete quenching of the electrons past the initial thermal energy rise due to high I_p, and Fig. 3.4(e) tells us that the steady-state sheet maintains coupling with the coil for a longer duration. Newly entrained particles affect the ability of the charge carriers to respond to the AC fields of inductive transformer, raising Θ_e for $t/\tau_{LC} \in [0.1, 0.45]$ as the skin depth shrinks. The low Θ_e of the initial pulse is an artifact of the diverging sheet width and does not necessarily indicate better permeability.

The broad takeaways from Fig. 3.4 are that the transient and steady-state solutions align well within the early formation phase ($t/\tau_{LC} < 0.1$) but deviate once the initial pulse fails to generate a well-formed sheet. The differences we observe for $N_{p,0}$ are primarily caused by lower V_0 and $n_{n,0}$ relative to our results in Chapter 2, which tells us that multi-pulse operation calls for smaller mass bits at lower discharge energies. Fig. 3.5 reinforces these notions by giving the time-dependent performance metrics across the same set of data. These results highlight why performance is less critical to our study than other property trends since the first pulse supposedly carries higher η_R and η_e than the steady-state solution, which is an artifact of the diverging sheet width. Panels (b) and (d) exhibit nonlinear behavior to demonstrate the competing conversion of thermal energy in the electrons to kinetic energy in the plasma sheet. Sharp asymptotic behavior results from closing the primary switch for inductive recapture.

Fig. 3.5(c) provides a more telling comparison of mass entrainment, which we observe

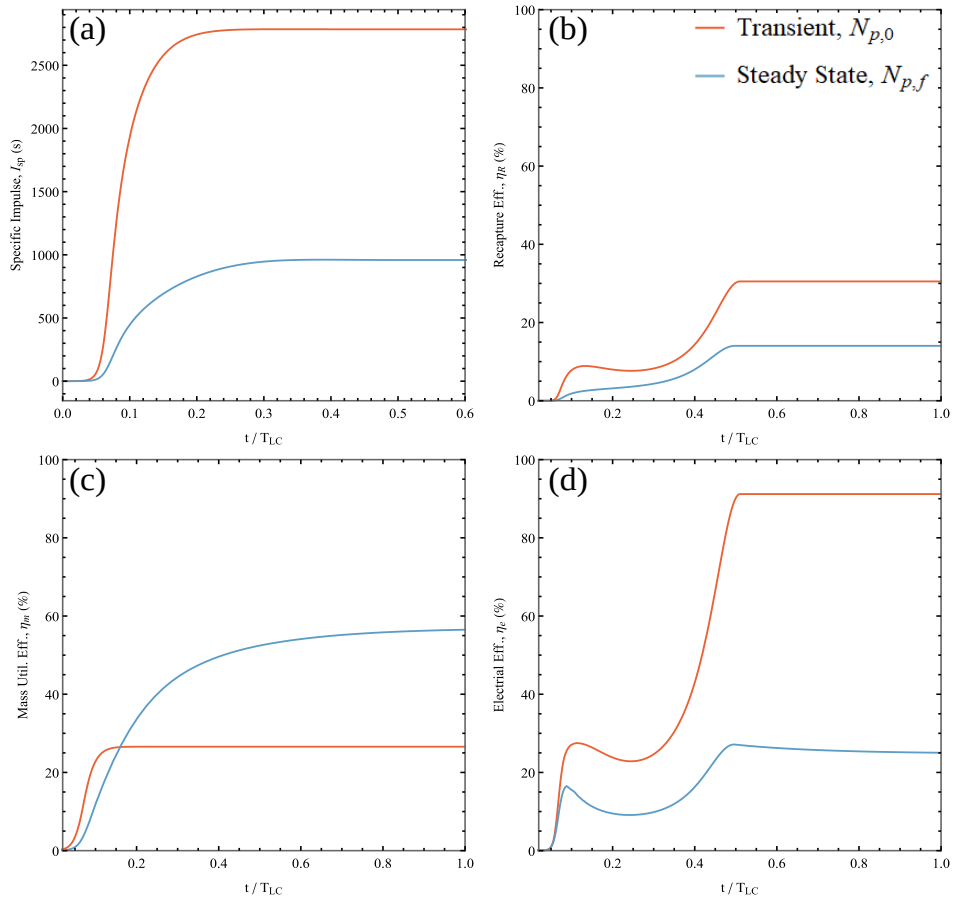

Figure 3.5: Time-dependence of multi-pulse model performance metrics for the baseline input conditions listed in Table 3.1 contrasting the first ($N_{p,0}$) and final ($N_{p,f}$) pulses.

to be significantly higher in steady state. A final value of $\eta_m, \approx 60\%$ indicates that the majority of injected neutral gas is profitably accelerated by the thruster. The figure also communicates that particle entrainment is more spatiotemporally gradual in a multi-pulse equilibrium, confirming the added importance of CX reactions as the propellant propagates downstream from the inductive driver. This has a secondary collisional effect, however, as the increased density downstream density slows the steady-state current sheet and hinders the electrical efficiency. Hence, the model calculates a low specific impulse ($I_{sp} \approx 1000$ s) relative to other EP devices for the baseline input conditions in Table 3.1.

3.4.2 Multiple Case Studies

The previous comparison is meant to detail the evolution of state properties across multiple consecutive pulses. Now, we look to analyze the influence of certain input parameters on the multi-pulse solution to the model, similar to our studies of pre-ionization and coil inductance in the previous chapter. We have already examined a mass flow rate parameter space for the purposes of reaching steady state and finding favorable regions of operation. We continue our investigation of characteristic neutral density and repetition rate below to visualize the time-dependent variable trends that underscore the efficient operating regimes in Fig. 3.3.

Influence of Characteristic Neutral Density

Previous PIT experiments and modeling efforts have varied the injected mass bit in both pulsed and static fill to characterize the output for different discharge and acceleration demands [8, 15, 43]. Using $n_{n,0}$ as our analog for m_{bit} under fixed circuit parameters and coil geometry, we can add to these efforts by offering the dynamic variable trends across steady-state pulses. We have found that η_m directly scales with higher $n_{n,0}$ for pulse rates of $5 - 10$ kHz from Fig. 3.3(b), which informs us that a greater fraction of propellant mass becomes entrained in the current sheet for larger overall injected gas populations.

Fig. 3.6 depicts the time-dependent state variables at three different values of $n_{n,0}$ for the input conditions listed in Table 3.1, where the characteristic densities correspond to $P_0 = 2, 3,$ and 4 mTorr in the order of the figure legend. These still represent steady neutral injection profiles subject to Eq. (2.58), but we have inspected these points to have relevance in later backfill comparisons. As expected, we observe in panels (a)-(c) that $n_{n,0}$ scales directly with n_s and inversely with v_s and w_s. A greater neutral particle population produces a denser, more compressed current sheet that propagates slower due to increased collisional reaction forces. We find that for linear increments in $n_{n,0}$ between data sets of $\sim 3 \times 10^{19}$ m^{-3}, v_s and w_s scale according to the square root whereas n_s scales linearly, as indicated by the gaps between the solution curves. Furthermore, characteristic neutral densities on the order of

10^{19} m^{-3} stimulate sheet densities $\mathcal{O} \sim 10^{20}$ m^{-3} due to both spatial integration and slipped neutrals left in the wake of previous pulses.

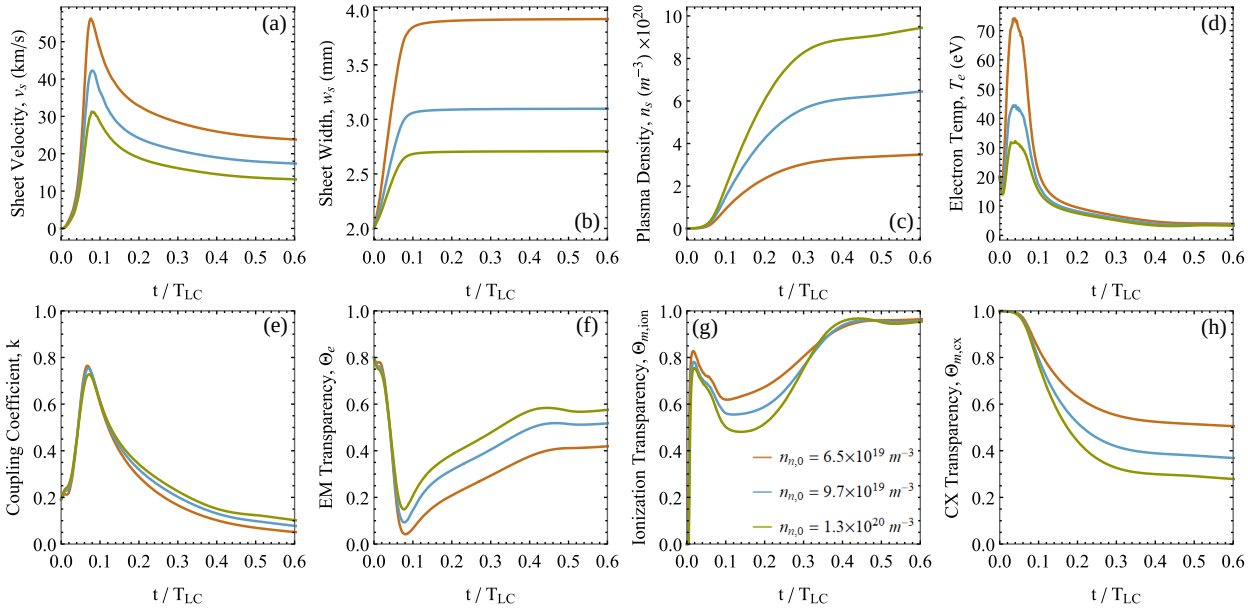

Figure 3.6: Multi-pulse time-dependence of state variables and transparency parameters critical to sheet formation and mass entrainment for variable characteristic neutral density. Data is generated from the baseline input conditions listed in Table 3.1, aside from $n_{n,0}$.

We note that the characteristic neutral density does not substantially change the shape of any dynamic properties - only the magnitude. This is intuitive since adjusting the mass bit maintains the discharge characteristics of the thruster. The model, in its current form, is poorly suited below a critical density threshold for given input voltage and coil inductance since the electrons in a diffuse plasma become sufficiently hot ($T_e \gtrsim 50$ eV) to excite higher ionization states in the current sheet, as seen in Fig. 3.6(d). Panel (e) depicts slight coupling differences across the latter stages of the entrainment phase during sheet deceleration, which are more apparent in (f) as Θ_e varies nonlinearly to reflect sheet width.

Higher neutral densities imply higher electromagnetic transparency, but lower ionization

and charge-exchange transparencies. Variations in ionization reaction rates are more subtle than for CX collisions across multiple pulses according to the parameters in (g) and (h) even though we observe drastic peak differences in Ohmic heating of the plasma. This demonstrates that the quenching of the electron population is more important to current sheet dynamics and performance scaling than initial energy deposition because slight $\Theta_{m,ion}$ dissimilarities between $t/\tau_{LC} \in [0.05, 0.4]$ influence n_s at much larger scales. This affirms the formulation of Ω in our previous analysis.

Influence of Pulse Repetition Rate

We vary our secondary mass flow parameter from Eq. (3.6) to quantify differences across the kHz range. Fig. 3.3 overtly demonstrates the importance of f_{rep} to overall thruster efficiency, verifying that high switching speeds are required to enable competitive PIT designs at lower discharge energies per pulse [39]. As before, Fig. 3.7 shows time-dependent trends at incremental pulse rate adjustments from the baseline conditions listed in Table 3.1.

We observe less variable activity as a result of changing f_{rep} compared to $n_{n,0}$, which tells us that much of the effect on thrust efficiency is contained in only a few state properties. Plots (b)-(e) and (h) depict negligible differences in sheet width, plasma density, electron temperature, coupling coefficient, and charge-exchange processes. Hence, work transfer between the elements of the inductive transformer remains roughly constant per pulse, with the caveat that the pulse repetition period exceeds the residence time of the plasma. Panel (g) indicates that lower pulse rates raise the ionization transparency of the steady-state solution by a small amount, but this is insignificant to overall entrainment since CX collisions dominate the given regime.

The electromagnetic transparency exhibits differences past the initial formation and acceleration phases, indicating that the skin depth varies since w_s remains constant across the sampled f_{rep} values. Delving deeper into the terms of Eq. (2.46), we find that the only changing value is the electron-neutral collision frequency from the embedded n_n term in Eq. (2.43). This also explains the differences in sheet velocity in Fig. 3.7(a) since collisional forces are

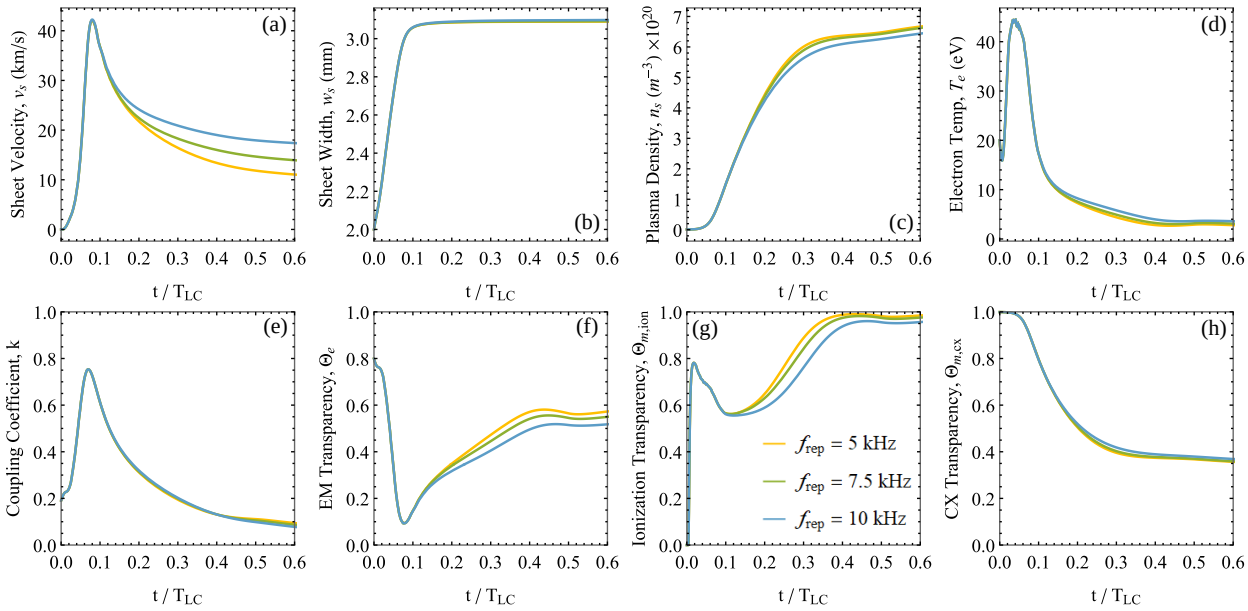

Figure 3.7: Multi-pulse time-dependence of state variables and transparency parameters critical to sheet formation and mass entrainment for variable pulse repetition rate. Data is generated from the baseline input conditions listed in Table 3.1, aside from f_{rep}.

higher for higher neutral densities at lower pulse rates. In essence, since f_{rep} has little effect on neutral particle entrainment per pulse, more pulses leads to better total entrainment and leaves fewer unswept neutrals downstream.

3.4.3 Multi-pulse Propellant Comparison

Lastly, we can compare the argon and xenon models using the multi-pulse architecture to verify whether the single-pulse propellant study maintains its dynamic trends in steady state. We have previously observed that atomic mass plays a key role in the current sheet physics, allowing xenon to significantly outperform argon in propellant mass entrainment at the cost of greater inelastic losses. Fig. 3.8 reaffirms these findings to some extent, but the evolution of neutral density shortens the performance gap.

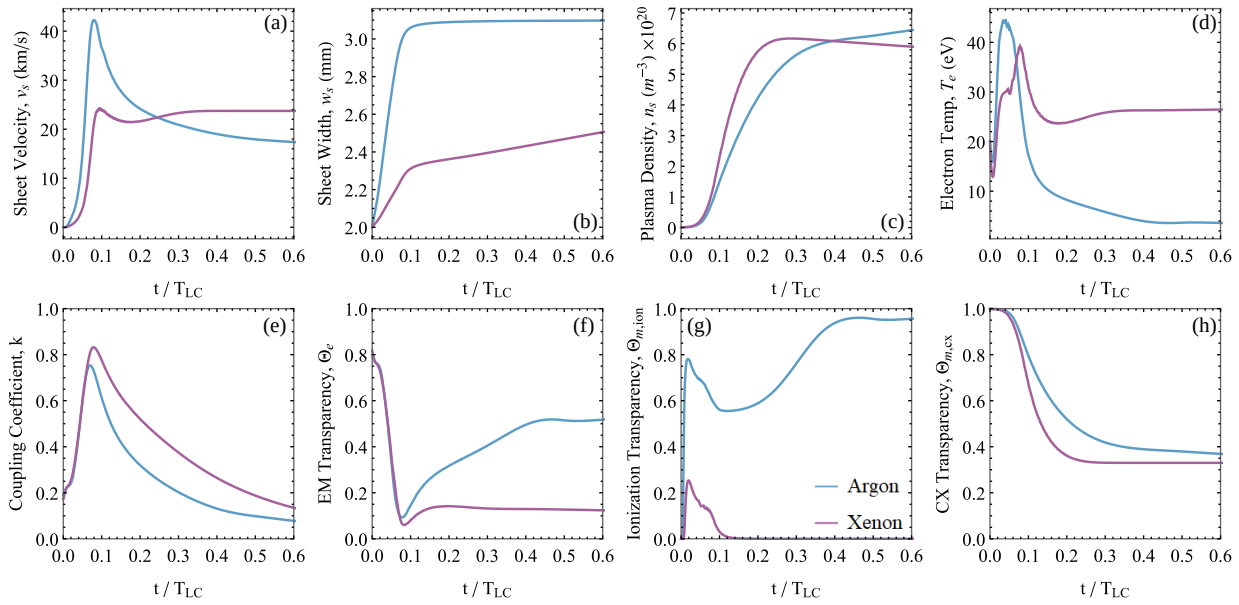

Figure 3.8: Steady-state time-dependence of state variables and transparency parameters critical to sheet formation and mass entrainment for argon and xenon propellants. Data is generated from the baseline input conditions listed in Table 3.1. Note that the argon model shows the same output as $N_{p,f}$ in Fig. 3.4.

Panel (a) already demonstrates nonconformity once the argon sheet loses over half of its peak velocity over an exponential deceleration phase while xenon maintains nearly constant v_s past $t/\tau_{LC} > 0.1$. We see in (b) that argon still achieves a higher final width, but (c) notably disagrees with the single-pulse comparison by depicting comparable plasma densities across both propellants for the same input conditions. Furthermore, the xenon plasma begins to lose particles past the acceleration phase due to neutral slip, indicating that a portion of entrained ions lack the energy to interact favorably with plasma currents. The mass transparency parameters given by (g) and (h) still show that xenon is relatively impermeable to upstream neutral particles with a much better probability of entrainment via ionization.

Electron temperature curves in (d) reinforce lower inelastic power losses for xenon due to ionizing and radiative processes. Paired with lower $\Theta_{m,ion}$, this tells us that the xenon

plasma requires less energy from the electrons to achieve better total ionization. This is because the xenon sheet sustains its impermeability to the AC fields of the coil for a longer duration to improve overall EM energy coupling. Plots (e) and (f) quantify this behavior and show that the skin depth of the steady-state argon plasma expands during the latter stages of the pulse due to thermal quenching of the electrons.

3.4.4 Summary of Results

We have extended our analysis of the 1D PIT model to multiple pulses to examine quasi-steady-state solutions in the experimental operating ranges of a low-discharge-energy, high-pulse-rate test article. Our findings demonstrate that the evolution of neutral density is the primary distinguishing factor relative to single-pulse case studies. The adjustment of mass flow rate and propellant type for a given circuit design yields varying plasma state properties and performance regimes. The primary results of the multi-pulse study are listed below:

- Multi-pulse operation in higher entrainment regions of the mass flow rate parameter space loosely requires a greater number of pulses to reach an equilibrium.

- Charge exchanges become increasingly important to the steady-state current sheet dynamics of argon due to the downstream propagation of the injected neutral gas profile.

- Varying the injected mass bit presents an uneven tradeoff between sheet velocity and plasma density, while varying the pulse repetition rate leads to fewer dynamic differences on a per-pulse basis.

- Xenon maintains better coupling and ionization properties through multiple pulses while evading inelastic losses that decelerate the exhaust. However, argon proffers a denser sheet at the same input conditions due to less fast neutral conversion.

Chapter 4

FACILITY EFFECT STUDY OF A FINITE NEUTRAL BACKFILL

Facility effect studies for EP devices at higher levels of technological readiness often aim to characterize the impact of an ambient backpressure on the performance of the thruster [11, 49, 50]. Our model is ill-suited to the quantification of performance metric gaps between a finite static fill and the in-space environment since we define I_{sp} and η_T in terms of m_{bit} in Eqs. (1.1) and (1.2). Instead, our goal is to compare the dynamic properties of plasma sheets generated in a backfill and the idealized steady-state solutions to inform the degree of fidelity in future test campaigns at low discharge energies per pulse.

Early PIT studies [16, 23, 40] have provided measurements under static fill conditions across a swath of input energies to investigate the effects of different pre-ionization schemes [15]. In a similar vein, we can explore our time-dependent 1D model solutions to distinguish the physical mechanisms that vary between different background conditions through the lenses of neutral gas entrainment, finite skin depth, and heating of the electron fluid population. This will enable us to substantively discuss the formation and acceleration of current sheets in a backfill, which is the primary contribution of this thesis.

4.1 Backfill Modeling

Up to this point, the injected neutral gas profile given by Eq. (2.58) has taken the form of a decaying exponential function with characteristic peak density $n_{n,0}$. In a backfill, the ambient density assumes a constant value in z and only deviates from its fixed linear condition across the entrainment period of a pulse. The inductive coil can still produce ample current densities to ionize the neutral particles situated within the coupling region to form a plasma

sheet, but the background gas is anticipated to affect the state properties over the evolved sheet propagation. Higher pressures in the millitorr range are presumed to dominate the rate of gas ingestion by the plasma, which obviates the examination of multiple pulses since the backround distribution is restored to its original constant value between discharges. We modify this assumption in the next chapter, but for now the spatial background density is given simply by

$$n_n(z) = n_{n,0}. \tag{4.1}$$

which becomes the input condition for each pulse modeled in a backfill.

We note that this comparison would ideally be made in higher dimensions to account for radial expansion, cooling, and the asymmmetric penetration of fields within the current sheet microstructure. Our model assumes uniformity to reduce the state properties to 1D, which violates the findings of several studies [17,23]. However, uniformity represents a better assumption in static fill than for steady injection, so we proceed knowing that certain radial and azimuthal effects will be ignored. A recent MHD numerical simulation has determined that these 2D processes are negligible across the plasma residence time in the coupling region [57], which lends some credence the results below.

4.2 Time-dependent Facility Effects

We maintain the input conditions of the previous chapter to examine consistent regimes across the backfill and steady-state models. Results are compared to identical solution curves corresponding to the ICs listed in Table 3.1 using the same color schemes across all studies found in this thesis. Fig. 3.1 depicts the pulsed neutral density evolution for the steady-state model data given here, which is important to the motivation of our inquiry. Recall that the background neutral profile begins to flatten across the axial span of the simulation as the inter-pulse continuity equation approaches an equilibrium. The progression from a Maxwellian neutral distribution centered at the coil face to a pseudo-backfill condition using

steady injection should produce similar exhaust dynamics.

Fig. 4.1 offers the strongest evidence against this prediction by giving the macro-level plasma sheet physics normalized by the LC-period of the pulse for both the backfill and steady-state solutions. We see that the greatest gaps between the two data sets exist in codependent sheet position and velocity, given by plots (a) and (c) respectively. Panel (b) finds that sheet width is nearly identical across both conditions, and (d) tells us that the backfill sheet will ionize a slightly greater plasma density across the latter stages of a pulse.

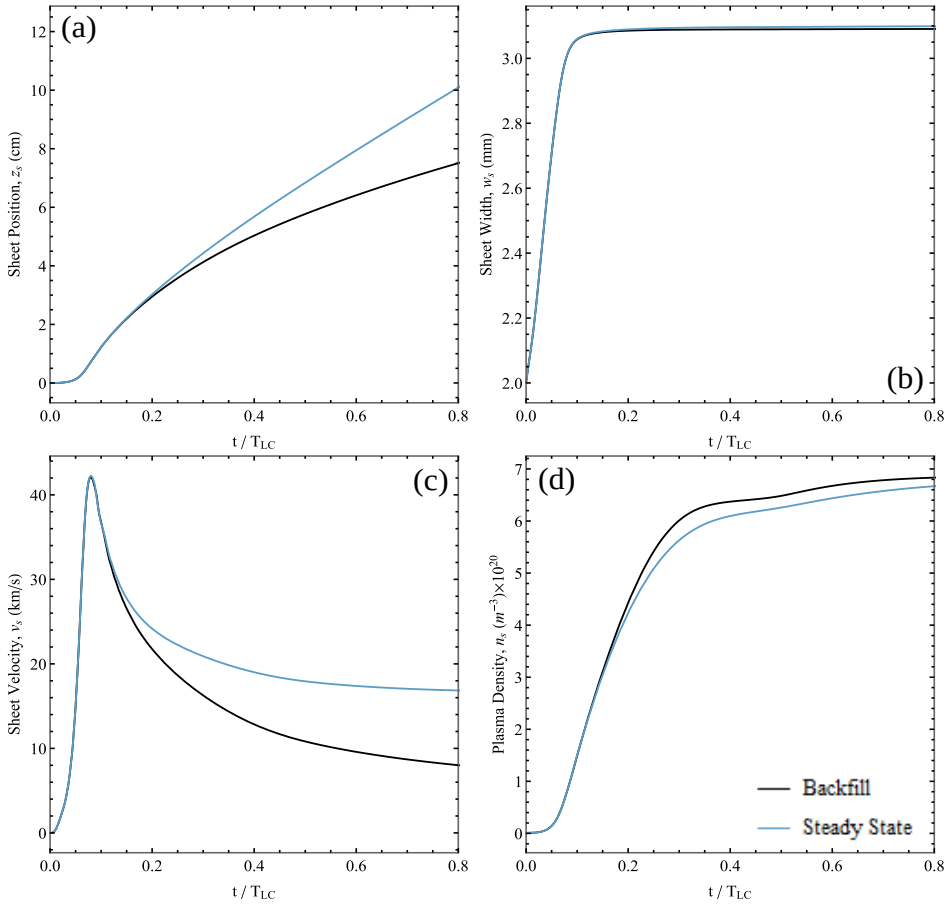

Figure 4.1: Time-dependence of PIT state variables describing macro-level plasma sheet physics under backfill and steady-state ambient neutral gas conditions. Data is generated from the baseline input conditions listed in Table 3.1. Backfill solutions are only collected for a single pulse.

The minor difference in total neutral ingestion is not substantial enough to justify wider deviations in the deceleration phase beyond $t/\tau_{LC} > 0.15$. These terms balance linearly according to the momentum equation given by Eq. (2.27), which suggests that the collisional drag force plays a more significant role in a backfill beyond the initial formation and acceleration phases. This has been readily anticipated by previous works [7, 23, 43], but we demonstrate that dynamic differences do not manifest in other state properties. Fig. 4.2 shows the calculated histories of fluid population energies, plasma current, and lumped-element coupling to highlight the overlap between results. We find that the energetics closely agree with only slight deviations in final electron temperature and coupling coefficient, given by panels (a) and (d) respectively. The backfill solution exhibits marginally greater quenching of the electron population at precisely the same point in time as we observe sheet velocity separation at $t/\tau_{LC} \approx 0.125$. This is because the collisional drag force, f_c, depends on the ionization reaction rate according to Eq. (2.28).

We observe in Fig. 4.2(b)-(c) that ion temperature and plasma current are in close agreement across facility conditions. The latter conveys that a Rogowski coil should be able to measure AC current in a backfill with the same fidelity as steady-state PIT operation. The cusp in I_p at $t/\tau_{LC} = 0.5$ corresponds to latching the capacitor for inductive recapture. Coupling discrepancies past $t/\tau_{LC} > 0.45$ found in (d) ultimately depict small errors in current sheet skin depth contained in the Θ_e term of Eq. (2.19). Fig. 4.3(a) elucidates these differences more explicitly by depicting a wider EM transparency gap past $t/\tau_{LC} \approx 0.125$. Since many differences first appear at this timescale, we understand exactly why the backfill and steady-state conditions differ.

At $t/\tau_{LC} = 0.125$, Fig. 4.1(a) shows us that both sheets are located at $z \approx 2$ cm. We return to Fig. 3.1 to examine the neutral density profile corresponding to the steady-state pulse, and find that $n_n(z) \approx n_{n,0}$ for $z \in [0, 2]$ cm, approximating a backfill condition. It is only once $n_n(z)$ begins to decay that we see any sizeable differences in state properties, but these are still relatively insignificant. The greatest concern is a misrepresentation of sheet velocity by a factor of almost two.

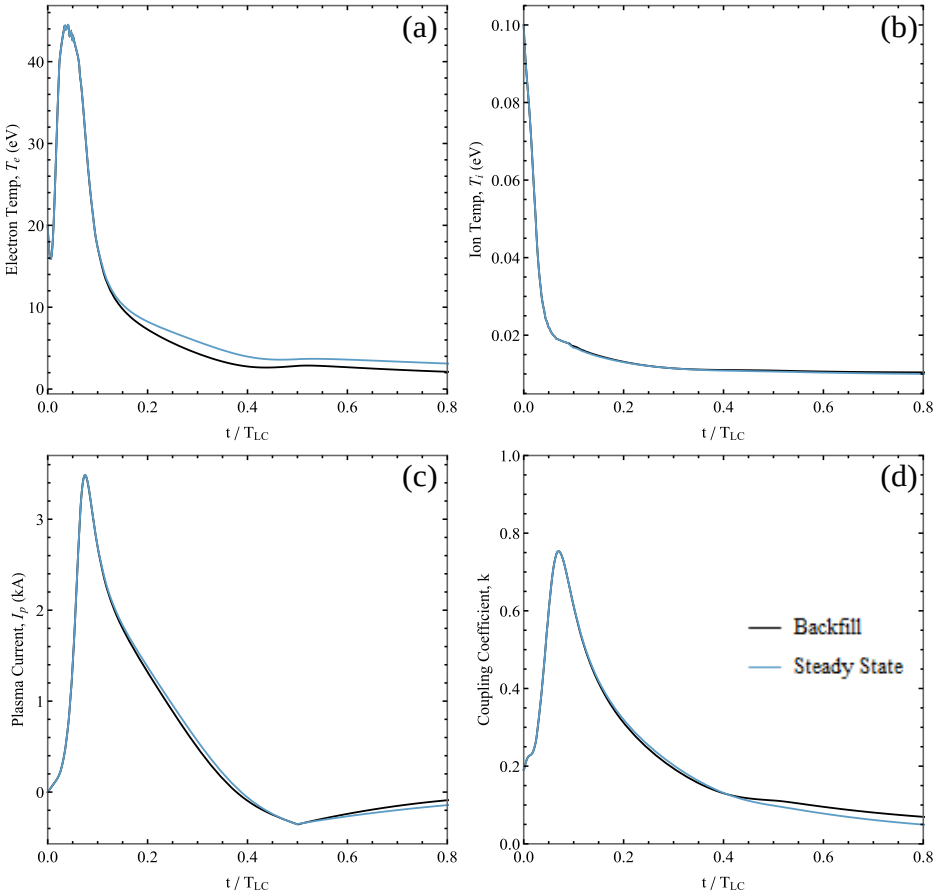

Figure 4.2: Time-dependence of system energy transfer under backfill and steady-state ambient neutral gas conditions. Data is generated from the baseline input conditions listed in Table 3.1. Backfill solutions are only collected for a single pulse.

Fig. 4.3(b)-(c) inform us that the velocity imbalance has less of an effect on neutral entrainment than we might suspect given the formulation of $\Theta_{m,ion}$ in Eq. (2.25). Still, a higher v_s corresponding to the steady-state solution yields lower ionization mass transparency, indicating a more well-formed sheet in the snowplow limit of neutral ingestion. The backfill condition still finds a greater total sheet density due to the increased importance of CX collisions and lower $\Theta_{m,cx}$.

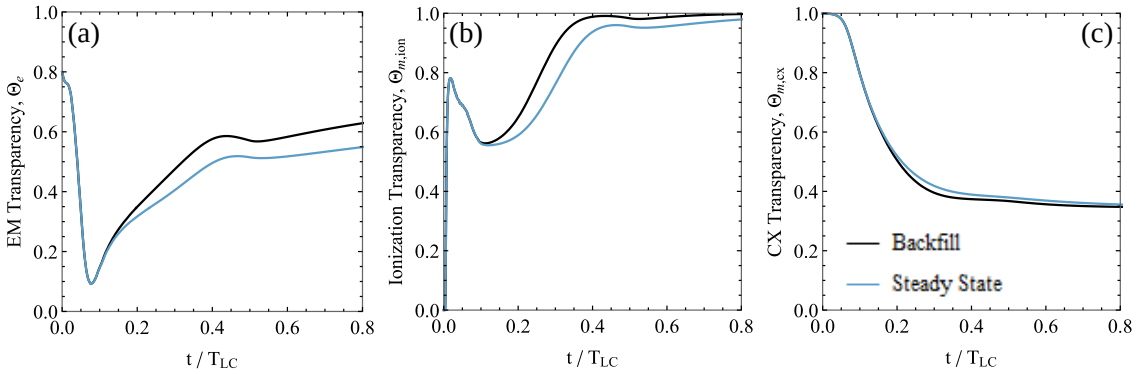

Figure 4.3: Time-dependence of plasma state properties describing electromagnetic permeability and mass entrainment processes under backfill and steady-state ambient neutral gas conditions. Data is generated from the baseline input conditions listed in Table 3.1.

4.3 Energy Partitioning and Sheet Formation in a Backfill

To better understand the process of current sheet formation for lower pre-ionization fractions and backpressures in the millitorr range, we provide a holistic comparison of kinetic, thermal, and internal plasma energy modes relative to the steady-state model output. We analyze the dependence of different efficiency metrics for varying charge voltage and characteristic neutral density to assess the relevance of the formation parameter proposed by Little *et al.* [58] from Chapter 2. The breakdown of energy partitioning ultimately clarifies substantive work transfer from the inductive coil to the various fluid populations in our model to demonstrate clearer differences between the backfill and steady-state operating regimes.

4.3.1 Energy Comparison

Fig. 4.4 gives seven distinct time-evolved energy modes across the normalized duration of a pulse to show the timescales at which different energetics influence current sheet dynamics. We normalize the energy modes by the instantaneous capacitor (E_{cap}) and inductor (E_{ind}) energies since the input circuit parameters are consistent across the two data sets. The

former is given by Eq. (2.65) and the latter is calculated as

$$E_{ind} = (L_0 + L_{eff})I_c^2/2. \tag{4.2}$$

Here, thermal energy (purple) is embedded in the volume-integration of ion energy given by Eq. (2.36), ionization energy (blue) is calculated as a frozen flow loss subject to Eq. (2.35), and Ohmic heating (cyan) is given by Eq. (2.33). We observe that thermal energy dominates the internal modes but that both rise during the primary deceleration phase of the sheet before approaching an asymptotic value as the ions cool and residual plasma currents subside.

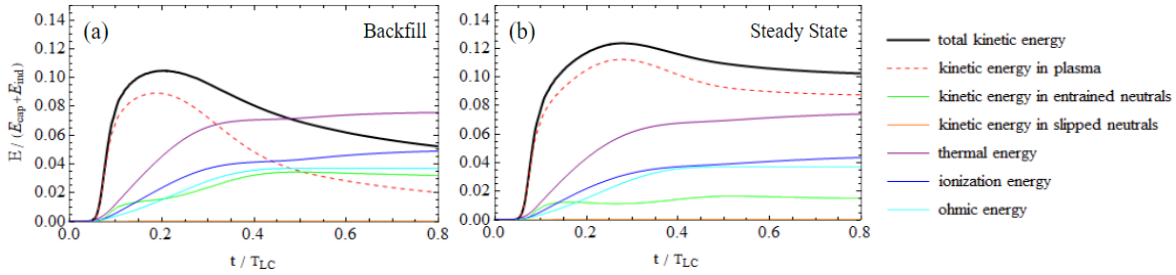

Figure 4.4: Time-evolving energy modes for (a) backfill and (b) steady-state conditions using the baseline inputs listed in Table 3.1. Calculations compare the kinetic energy partitioning of various fluid populations, thermal energy, ionization energy, and energy deposited by Ohmic heating. Results are normalized by the instantaneous capacitor (E_{cap}) and inductor (E_{ind}) energies.

By subdividing the kinetic energies of the exhaust species by the plasma sheet, entrained neutrals, and slipped neutrals (i.e. v_s, v_f, and Δv_{sf}), we can characterize the relative importance of different mass utilization processes across the two background conditions. Fig. 4.4(a) tells us that the total kinetic energy in a backfill is surpassed by total thermal energy in the sheet at $t/\tau_{LC} \approx 0.5$, representing the zero-crossing of the coil current waveform. This is also roughly the point at which the kinetic energy in the plasma ions (red) intersects the kinetic energy in the entrained neutral (green) population. CX collisions therefore dominate ionization reactions in the latter half of the backfill pulse period.

The steady-state solution in Fig. 4.4(b) depicts a diminished importance of charge exchanges due to a higher overall kinetic energy in the plasma ions. We find that the separation between kinetic energies across the two background conditions occurs even earlier than $t/\tau_{LC} \approx 0.125$ because the values shown here are dwarfed by the scale of v_s in Fig. 4.1(c). Still, higher terminal v_s corresponding to the steady-state current sheet explains the near twofold increase in total kinetic energy. Thermal energy deposition is consistent across the two simulations while ionization losses are lower in steady state. In both cases, the slipped neutrals (orange) contain negligible amounts of kinetic energy relative to the system.

These energy plots pair with Fig. 4.1(d) to convey that near-equal sheet densities result from broader underlying differences balanced by the conservation of momentum. In a backfill, the increased overall presence of downstream neutrals raises both the drag force and the probability for charge exchanges between plasma ions and fast neutrals. Ohmic heating of the electron populations is balanced, but the quenching of T_e by electron-impact ionization is less extreme in steady-state operation. With respect to our earlier discussion of mass utilization scaling in Section 2.7.4, this tells us that testing in a backfill decreases the efficiency of the formation process and generates a more transparent plasma. Therefore, more energy is required to drive fewer net ionization reactions.

Polzin *et al.* [43] have provided similar insights for a single-pulse model by analyzing the energy modes of PIT MkV conditions listed in Table 3.2 as a function of the dynamic impedance parameter, α. Fig. 4.5 summarizes these results, where panel (a) captures the peak efficiency case for lowest mass bit, and (c) raises m_{bit} to decrease α (see Eq. (2.69)). The solutions shown resemble our results in that kinetic and thermal energy in the plasma increase with time early in the discharge when the electromagnetic coupling between the coil and the sheet are greatest. The progression from (a) to (c) demonstrates that kinetic energy is overtaken by thermal and internal depositional modes in the limit $\alpha \to 0$.

Fig. 4.5 also gives the magnetic field energy resulting from the coil current, I_c, which decreases in peak value while the duration of the first half-cycle increases with lower m_{bit}. As the current sheet propagates away from the coil more quickly, the magnetic field occupies

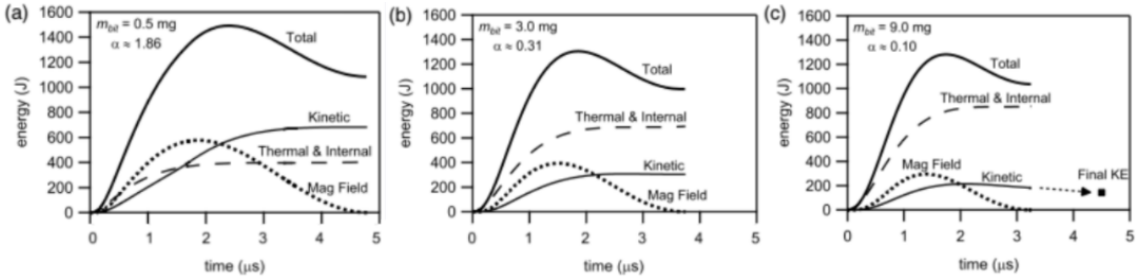

Figure 4.5: Results of previous model calculations on argon for PIT MkV conditions showing the time history of total energy in the plasma and the partition between plasma kinetic energy, thermal and internal energy, and energy in the magnetic field for mass bits of (a) 0.5 mg, (b) 3.0 mg, and (c) 9.0 mg (from [43]).

the space between the transformer elements to compensate for smaller mutual inductance. An increased mass bit therefore implies greater plasma inertia and lower v_s, leading to a slower change in inductance and an increase in maximum I_c to drive higher values of I_p. Consequently, there is an increase in Ohmic heating at the expense of plasma acceleration. We add to this finding in our backfill energy comparison on a smaller scale since $n_{n,0}$ is fixed across Fig. 4.4. Mass bit is a poor input analog for our purposes, but the tradeoff is similar nonetheless. We demonstrate that kinetic energy will compete with CX collisions and ionization reactions according to the initial neutral density profile of a pulse.

4.3.2 Dimensionless Scaling in a Backfill

Lastly, we investigate sheet formation in a static fill analytically to understand whether a critical threshold exists for the production of impermeable plasmas. Fig. 4.3 gives evidence that the current sheets generated in both a backfill and steady-state pulsed operation will be partially transparent to the electromagnetic fields of the drive coil and mass entrainment via ionization and CX collisions. These results only test a single set of favorable input conditions for argon, however, so while we develop an intuition for the influence of a finite ambient backpressure on temporal dynamics, we have a limited scope of efficiency scaling. Again,

the values of performance metrics for testing in a backfill are somewhat meaningless due to a high, confounding mass bit distributed evenly across the chamber rather than uniformly within the coupling region of the coil.

With this in mind, we return to Eq. (2.73) to assess the trends of the single-pulse formation parameter in a backfill condition. We note that Ω scales with $m_{bit}^{-1/2}$ due to the incorporation of α in the approximation of E_{ion}, which immediately tells us that the value of Ω is less important to our study here than in Chapter 2. Still, we adjust the design inputs relevant to the backfill testing of an adolescent test article such as HiPeR-PIT; namely, ambient pressure and charging voltage. Fig. 4.6 depicts the spread of recapture, electrical, and mass utilization efficiencies for $V_0 \in [0, 5]$ kV and $n_{n,0}$ corresponding to $P_0 = 2$ and 3 mTorr, respectively. All other ICs are consistent with Table 3.1. Ω is plotted discretely to show the dependence of η_m on key variables indicating a well-formed plasma.

Fig. 4.6(a)-(c) show that η_R and η_m scale directly with increasing V_0, while η_e inversely approaches an asymptotic value after an initial nonlinear decrease. Lower backpressure improves the efficiency parameters across all aspects of the system, but higher η_e at sub-kV charging voltages in (b) is an artifact of poor sheet formation. We find evidence of this in (d) such that low values of Ω correspond to data points collected at lower V_0. Mass utilization scales reasonably well for higher voltages at the given conditions because, as we have discussed in the previous section, charge exchanges are more probable at higher overall sheet energies.

Panel (d) indicates that PIT operation in a backfill results in lower Ω than the conditions shown in Fig. 2.10. We note that Fig. 4.6 depicts higher input values of L_c at lower $n_{n,0}$, which affects the value of η_m. Here, we still observe a sharp rise in mass utilization with exponentially increasing Ω, but without the characteristic "knee" in the curve as before. The vertical asymptotic behavior is indicative of maximum formation parameters near unity at given neutral densities. Hence, the backfill condition is unable to reach a threshold Ω^*, which leads us to believe that testing in a backfill will always produce semi-transparent current sheets.

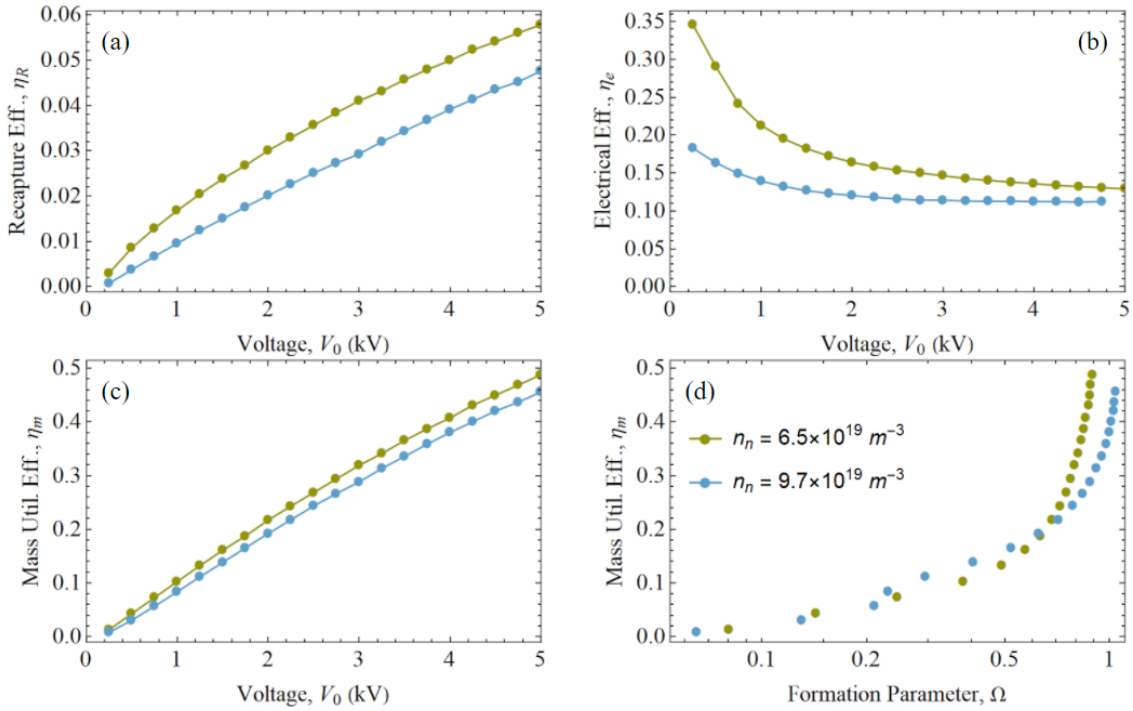

Figure 4.6: Dependence of mass utilization efficiency on initial capacitor charge voltage and neutral backpressure for a backfill condition. The (blue) baseline case corresponds to the ICs listed in Table 3.1, but we adjust the static neutral density to compare test pressures corresponding to $P_0 = 2$ and 3 mTorr.

We note that lower ambient pressure drives higher values of Ω for the same incremental increase in V_0. If we consider the data points clustered to the right of Fig. 4.6(d) corresponding to $\eta_m \geq 0.25$ to indicate sufficiently well-formed sheets fit for experimental study, then we can postulate a cutoff voltage for backfill testing at a given neutral pressure. The varied presence of background neutral particles implies that this critical charge voltage, V_0^*, directly scales with P_0. At 2 mTorr, this test condition resides at $V_0^* \approx 2.5$ kV, and at 3 mTorr, we get $V_0^* \approx 3$ kV. Higher neutral densities therefore yield more impermeable current sheets, but at a greater voltage requirement. In both cases, the overall efficiency is poor since dynamic impedance is well below the optimum range given by Polzin [7]. The data sets shown correspond to $\alpha = 0.152$ and 0.227 in order of ascending $n_{n,0}$.

4.4 Implications for Experimental Design

The ultimate goal of the backfill comparison is to confirm and refine the utility of future testing with a simplified gas injection scheme in steady state. Since we demonstrate that the current sheet dynamics are in close agreement across a majority of critical state properties, we conclude that testing in this domain is a worthwhile endeavor for the early stages of PIT development. Future measurement of thruster performance will require lower base pressures, as we discuss in the next chapter, as well as an expanded set of diagnostics to find the impulse bit of propellant ejecta [10]. It is possible that adjusting the initial conditions that affect sheet deceleration (e.g. χ_0 and f_{rep} in Figs. 2.6 and 3.7, respectively) will close the gap between the backfill and steady-state operating conditions, but in modeling these effects we find the differences to scale linearly. We summarize the findings of this chapter and their implications below:

- The majority of state properties across backfill and steady-state conditions agree within a 5% tolerance across the time-duration of a pulse for argon propellant. The most notable counterexamples of this finding are sheet position and velocity, where v_s experiences a near twofold decrease due to the collisional drag force imparted by downstream neutral particles.

- The evolution of neutral density in a steady-state equilibrium yields conditions identical to a backfill near the coil face, so the formation and acceleration phases for $t/\tau_{LC} \in [0, 0.125]$ overlap closely. Measurements in a backfill taken during the first quarter of a half-cycle carry high fidelity.

- The findings of experiments conducted in a backfill could be scaled to results for steady gas injection using the model at measured design inputs.

- CX collisions in the deceleration phase of sheet propagation balance with higher ionization losses to deposit more kinetic energy in the fast neutral population for a backfill.

The overall kinetic energy of the system is nearly halved for the same thermal energy deposition.

- Higher charge voltages proffer better formation scaling up to a critical limit in a backfill, but the resulting plasmas will always be semi-transparent to the AC fields of the coil and upstream neutrals. Increased backpressures call for greater charge voltages to generate well-formed sheets. For pressures above $P_0 = 2$ mTorr, input voltages above 2.5 kV produce best results with diminishing returns.

- Finally, the core findings of this comparison are consistent across argon and xenon propellant models, so we omit the latter to avoid redundancy. We still predict that xenon produces better sheet properties that improve energy and mass scaling. For numerical evidence, refer to Appendix B.

Chapter 5

INTERMEDIATE TEST PRESSURE STUDY ASSUMING A BACKFLOW

The backfill comparison presented in the previous chapter gives a clear-cut distinction between idealized operating conditions in the low-level ground test and space environments. We now append the static fill condition to examine time-dependent effects on PIT sheet dynamics at lower experimental pressures. It is anticipated that steady gas injection introduced to a chamber held at a static particle density far lower than the peak input neutral density will equilibrate between pulses. We refer to this as a "backflow," wherein gas particles further downstream from the peak neutral density region ahead of the coil replace the propellant ingested by the current sheet on the timescale of the repetition period.

The purpose of this study is to determine whether it would be worthwhile to test the HiPeR-PIT using steady gas injection at lower chamber pressures with more powerful pumping equipment. We adjust the inter-pulse model described in Chapter 3 and quantify the predicted operating differences for steady-state solutions across the same baseline input conditions for lower discharge energies per pulse. Relative performance metric errors are provided to demonstrate the varying facility effect of ambient pressure.

5.1 Physical Interpretation of a Backflow

We propose the backflow concept to approximate the equilibration process between pulses for a high-pulse-rate PIT design in low vacuum. In doing so, we make a series of approximations to remain consistent with the input conditions listed in Sections 2.4 and 3.1 while maintaining the 1D architecture of our model. Pressure equilibration and gas diffusion are multi-dimensional processes as we have mentioned before, so the results shown are inexact

and depend greatly on the individual sheet physics. We begin formulating adjustments to the multi-pulse model by describing the modified evolution of neutral density.

5.1.1 Simplifying Assumptions

We give a side-on schematic of the backflow condition to better explain the neutral particle action in 1D for a simplified test chamber in Fig. 5.1(a). The current sheets are depicted by solid rectangles of constant width propagating in z with variable monochrome gradients to indicate higher densities as entrainment takes place over time. Discs of plasma are fixed at the outer radius of the coil (left) to maintain the model geometry, which is a poor assumption for chamber walls that avoid magnetic field compression according to the facility effect study of Polzin and Reneau [52]. For higher-fidelity 2D and 3D models, radial expansion should be considered since the diameter of the plasma relative to the cross section of the chamber will have a substantial effect on equilibration. We use n_{bf} and $v_{th,n}$ to refer to the backflow neutral particle density limit and the thermal velocity of the propellant, respectively.

Neutral density profiles of the various input conditions are compared in Fig. 5.1(b) directly below the chamber schematic to maintain a consistent depiction of axial position. As seen, a backfill offers a constant injected neutral density function of $n_{n,0}$ as we discuss in Section 4.1, and the exponential distribution labeled $n_n(z)$ corresponds to the form given by Eq. (2.58) for pulsed flow. The backflow condition maintains a finite static fill below the peak neutral density value, meaning that $n_n(z)$ will assume an exponential decay before leveling off at a horizontal asymptote set at the vacuum density, n_{bf}. We assume that the backflow condition will yield smooth neutral density profiles constrained between $n_{n,0}$ and n_{bf} such that the adjustment of n_{bf} essentially allows us to model sheet dynamics at different test pressures.

5.1.2 Adjusted Inter-pulse Model

We maintain the single-pulse model to develop the temporal dynamics of the lumped inductive transformer across the LC-period of the circuit, but we adjust the inter-pulse model

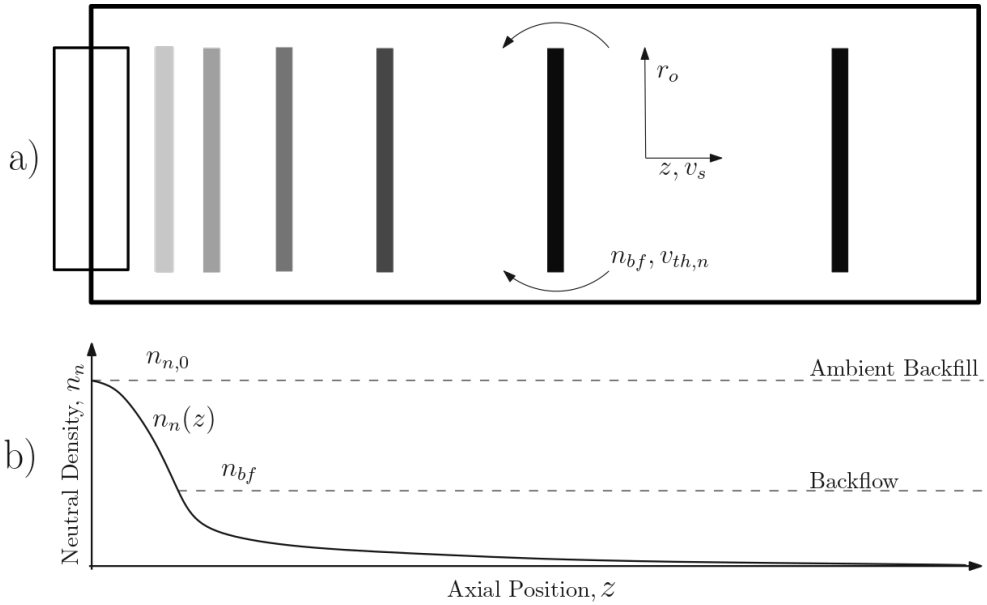

Figure 5.1: (a) Side-on schematic of neutral backflow in a simplified test chamber showing the axial translation of a current sheet of outer radius r_o with gradient plasma density. (b) Idealized spatial neutral density distributions for exponential, backfill, and backflow profiles. The solid line represents a single-pulse injected density analog, seen in Eq. 2.58. Backfill denotes a constant peak density and the backflow condition incorporates a lower base particle density in the chamber.

given in Section 3.1 to raise the pulsed progression of $n_n(z,t)$. The PDE given by Eq. (3.1) is appended to include an approximate backflow term that uses the variables seen in Fig. 5.1:

$$\frac{\partial n_n(z,t)}{\partial t} = -c_{s,n}\frac{\partial n_n(z,t)}{\partial z} + D_n\frac{\partial^2 n_n(z,t)}{\partial z^2} - \frac{n_n(z,t) - n_{bf}}{r_o/v_{th,n}} H\left(n_{bf} - n_n(z,t)\right) \tag{5.1}$$

where $n_{bf} = P_0/(e_c T_n)$ converts torr input to m^{-3} and $v_{th,n} = \sqrt{e_c T_n/m_i} \approx c_{s,n}$. We maintain the same boundary and initial conditions. Since we assume T_n to be held constant at room temperature, we neglect radiative cooling as before. The backflow term estimates the partial derivative of neutral density at a given radius as the neutral density differential per backflow timescale, $r_o/v_{th,n} \sim 0.5\ \mu$s. This timescale is comparable to the pulse period, t_{rep}, for high-

pulse-rate switching and smaller coil geometries. We include a Heaviside step function to account for a backflow only when $n_{bf} > n_n(z,t)$, which means that the inter-pulse density adjustment will lag behind the true system constraint given by Fig. 5.1(b).

Fig. 5.2 depicts the neutral density evolution for multiple backflow conditions in the same style as Fig. 3.1 for the steady-state solution. Ambient pressure is varied between 10^{-4} and 10^{-8} Torr to show that a lower base vacuum approaches the idealized steady-state results using the same input conditions found in Table 3.1. The fixed (dashed) lines appearing in each plot correspond to n_{bf} and confirm that the modified inter-pulse model slightly overshoots the given constraint since $r_o/v_{th,n} > t_{rep}$ at $f_{rep} = 10$ kHz.

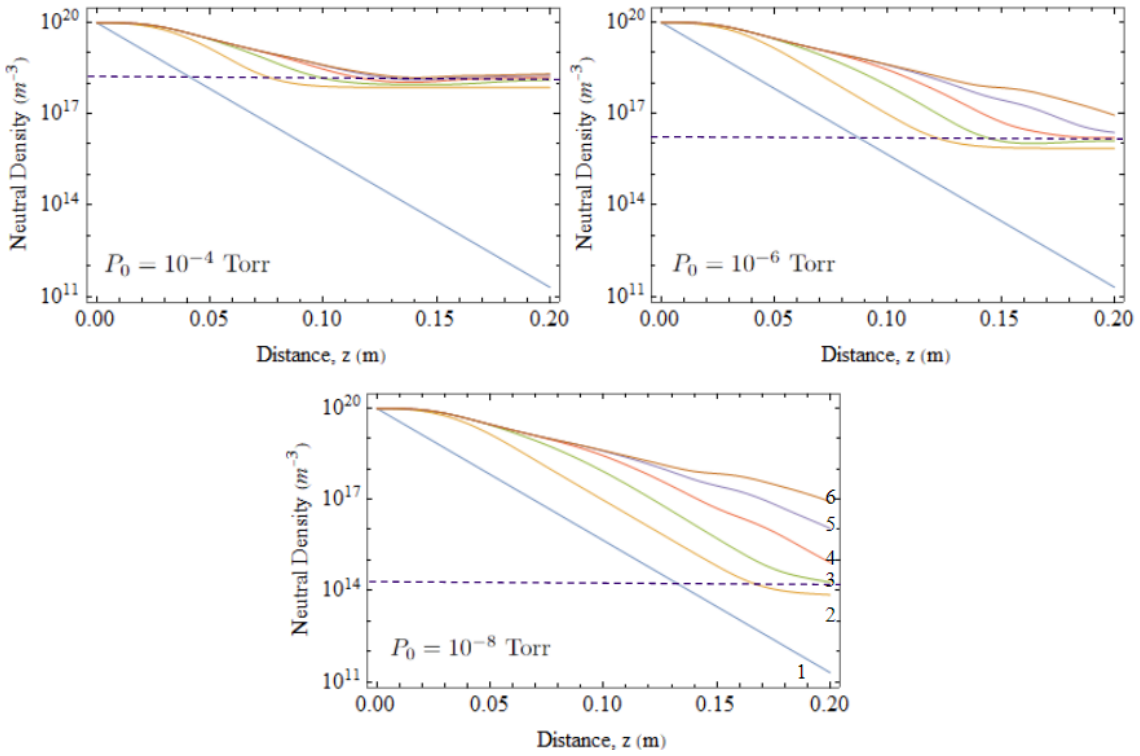

Figure 5.2: Spatial evolution of background neutral density, $n_{n,j}(z)$, for six pulses and five inter-pulse adjustments at the baseline input conditions listed in Table 3.1 for a PIT operating in a backflow at various test pressures. Pulses are labeled for $P_0 = 10^{-8}$ Torr. This figure demonstrates the ability of the backflow model to adjust the initial neutral density profiles according to test density, n_{bf}, given by the dashed lines.

5.2 Time-dependent Facility Effects

The adjusted neutral density evolutions depict a backflow as an intermediate test condition in the context of the backfill comparison. By raising the base pressure closer to the peak density of the injected neutral population, we approach the backfill model in the limit $n_{bf} \to n_{n,0}$. We can therefore examine the effect of only a slight backflow to consider less robust pumping mechanisms like those in the benchtop setup of HiPeR-PIT, as we discuss in the next chapter. The efficacy of the model will depend on the ability of the vacuum equipment to maintain n_{bf} in between pulses, but for the purposes of this study we assume constant ambient base density. To demonstrate the agreement between the backflow and steady-state models, we set $P_0 = 2$ mTorr corresponding to $n_{bf} = 6.5 \times 10^{19}$ m^{-3} for the following time-dependent comparisons where $n_{n,0} = 9.7 \times 10^{19}$ m^{-3}, representing a 1 mTorr difference.

5.2.1 State Properties

We present the time-evolved state properties describing macro-level sheet physics, energy transfer, and transparency parameters in the same style and order as Section 4.2 to isolate the influence of a backflow. Since the intermediate test pressure adjustment only aims to edit $n_n(z,t)$ over the course of multiple pulses, we find that the backflow model affects the variables that are most prominently driven by neutral density ahead of the coil such as z_s, v_s, and Θ_e. Fig. 5.3 shows us that even at a high base vacuum relative to the characteristic peak density of gas injection, we find that the backflow results lie closer to the steady-state output than the backfill model. Sheet width and plasma density are nearly unchanged by the adjustment in Eq. (5.1), and significant differences only appear during the deceleration phase past $t/\tau_{LC} > 0.3$.

Fig. 5.4 confirms that the energetics of the backflow solution align with the steady-state results almost exactly, with only a slight deviation in final electron temperature. We have discussed in our backfill analysis that the electron populations experience slight differences in quenching due to varied ionization probabilities, which are evident in Fig. 5.5(b). This

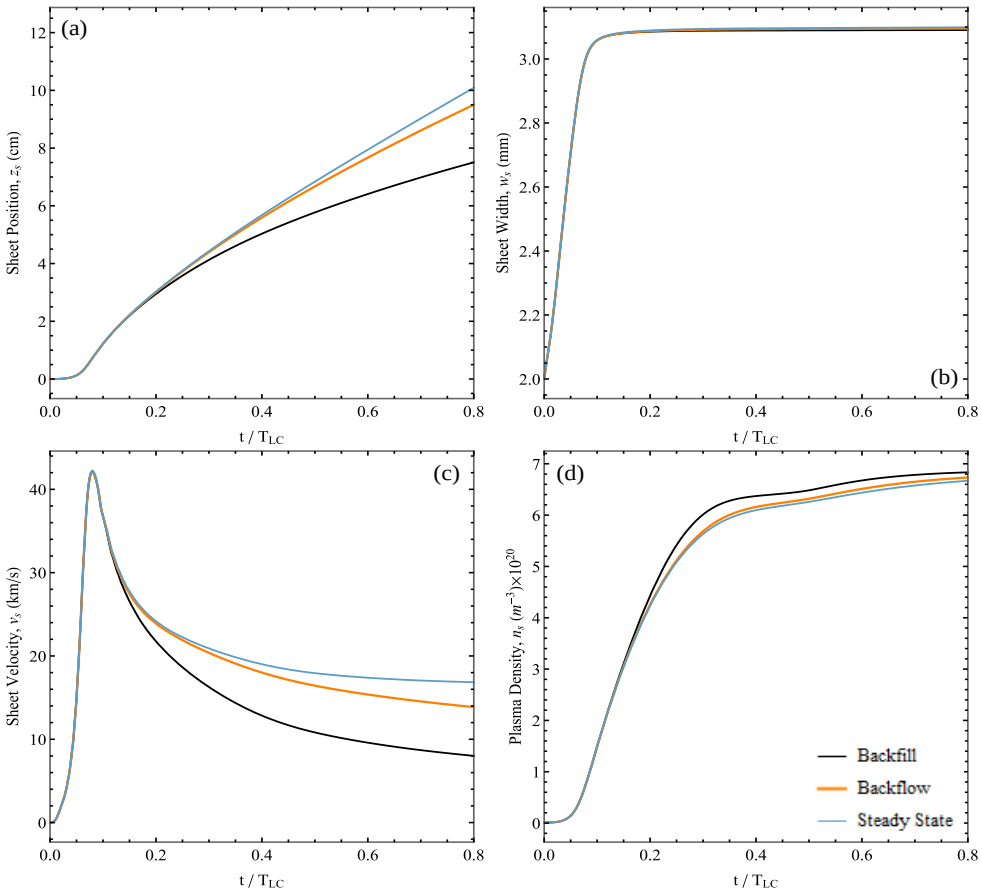

Figure 5.3: Time-dependence of PIT state variables describing macro-level plasma sheet physics under backfill, backflow, and steady-state ambient neutral gas conditions. Data is generated from the baseline input conditions listed in Table 3.1 and for $n_{bf} = 6.5 \times 10^{19}$ m^{-3}.

tells us that pressure equilibration between pulses allows for higher partitioning of energy in the plasma over the fast neutrals. Fig. 5.5(a) gives evidence of larger changes in skin depth across the three conditions due to higher differences in electron-neutral collision frequency at distances further from the coil.

Across Figs. 5.3, 5.4, and 5.5, the key takeaway is that a low-burden backflow condition represents a large improvement in correcting experimental error introduced by testing in a static fill. The primary sources of error are consistent across the time-dependent state

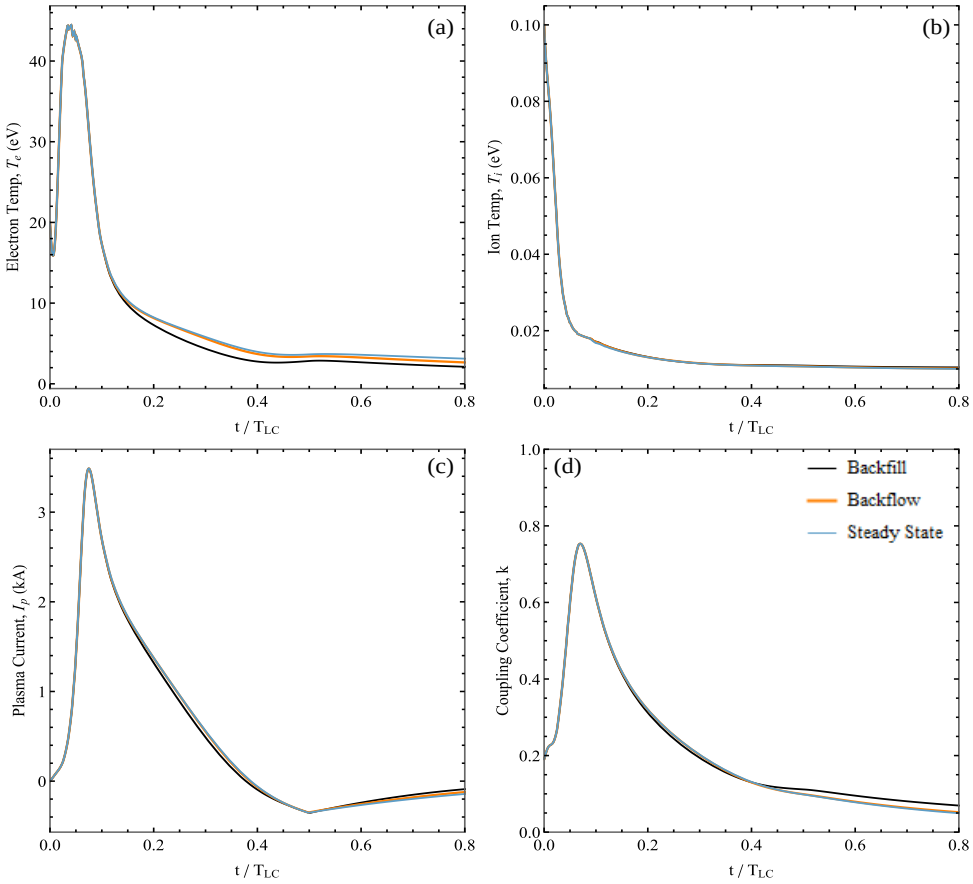

Figure 5.4: Time-dependence of system energy transfer under backfill, backflow, and steady-state ambient neutral gas conditions. Data is generated from the baseline input conditions listed in Table 3.1 and for $n_{bf} = 6.5 \times 10^{19}$ m^{-3}.

properties of the plasma, but we can greatly diminish the magnitude of these effects by pumping to a slightly lower base pressure.

5.2.2 Time-dependent Performance Metrics

It is demonstrated by Fig. 5.3(c) that v_s varies inversely with collisional drag ahead of the thruster for different ambient conditions. We therefore anticipate that modeling differences are amplified across the performance metrics given by Eqs. (1.1-2) and (2.66-67) since mass

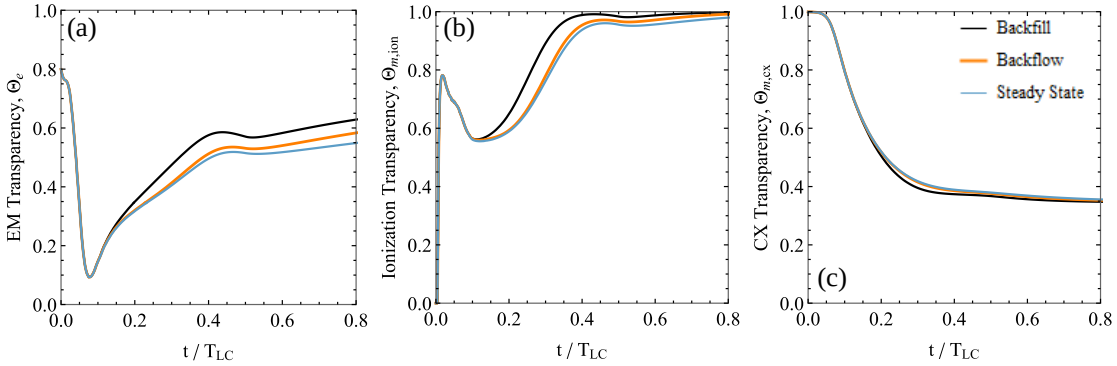

Figure 5.5: Time-dependence of plasma state properties describing electromagnetic permeability and mass entrainment processes under backfill, backflow, and steady-state ambient neutral gas conditions. Data is generated from the baseline input conditions listed in Table 3.1 and for $n_{bf} = 6.5 \times 10^{19}$ m^{-3}.

bit also varies widely given the form of Eq. (2.62). Below, we give the time-dependent performance metrics across the three background neutral conditions in Fig. 5.6 to focus on the separation between the models rather than the values of the metrics themselves.

We have previously observed that backflow data more closely resembles idealized steady-state operation across the many state properties describing current sheet dynamics. Now, we understand this to be reversed at a system level, where the backflow data appears to be more in alignment with backfill results at the same initial conditions. Fig. 5.6(a)-(c) depicts a much higher degree of separation between backflow (orange) and steady-state (blue) curves due to the double effect of changing v_s and m_{bit}.

As we delve into each plot, we notice that I_{sp} and η_R have the same horizontal scaling since the two metrics are co-defined in our model for equal circuit designs. Specific impulse exhibits a sharp increase then levels off past $t/\tau_{LC} > 0.3$, whereas η_R has an initial jump due to the early acceleration phase then experiences an exponential rise to a final value from inductive recapture. Mass utilization scaling in (c) realizes the primary performance gap between backflow and steady-state conditions such that η_m approaches a linear function in time in the limit $n_{bf} \to n_{n,0}$. Electrical efficiency, however, finds closer agreement across the

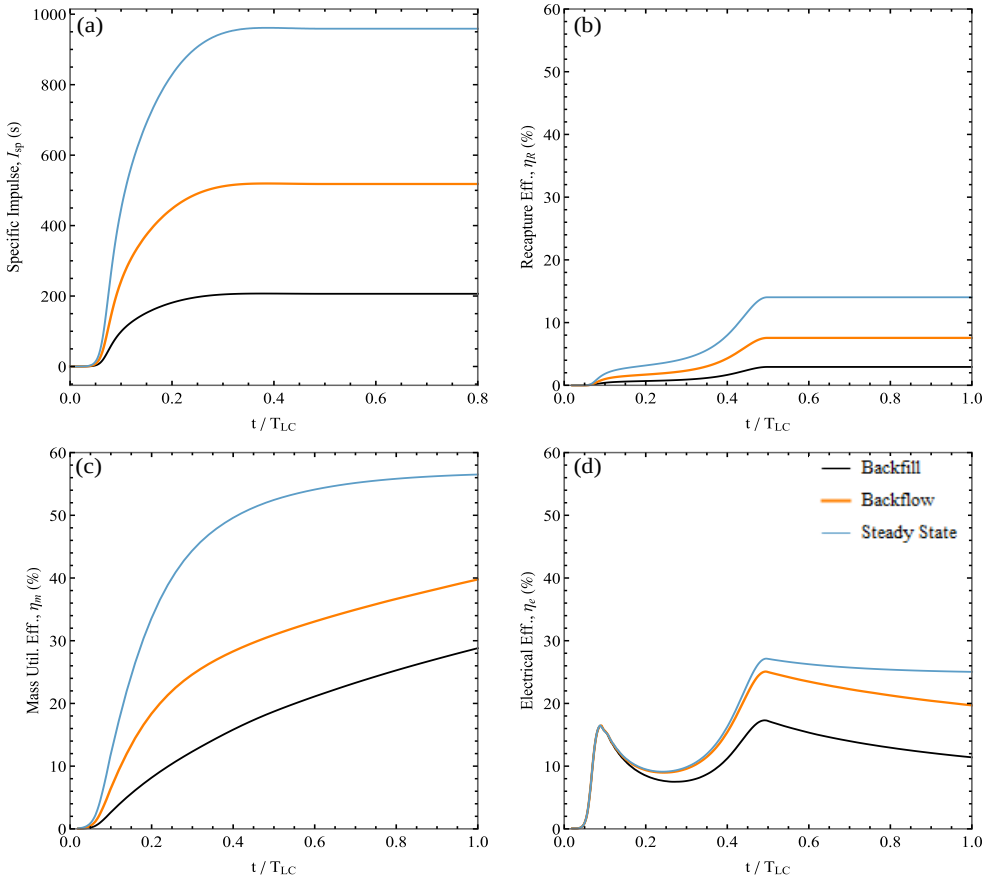

Figure 5.6: Time-dependent performance discrepancies across backfill, backflow, and steady-state ambient neutral gas conditions. Data is generated from the baseline input conditions listed in Table 3.1 and for $n_{bf} = 6.5 \times 10^{19}$ m^{-3}. This figure demonstrates wide gaps in performance for different conditions with the same input parameters.

deceleration and recapture phases after an initial peak at $t/\tau_{LC} \approx 0.1$ due to maximum v_s.

Panels (c) and (d) jointly inform us that a high n_{bf} relative to $n_{n,0}$ will produce entrainment similar to a backfill with energy partitioning similar to steady injection. This is an artifact of our mass bit calculation because a backflow will present comparable rates of ionization reactions and charge exchanges to the idealized model. Since CX collisions fail to compensate for increased drag, we find a lower time-evolution of η_m. The conditional error

introduced by higher $n_n(z,t)$ downstream from the coil can be assessed to determine whether a critical vacuum pressure exists such that mass utilization is no longer diminished.

5.3 Predicted Test Error at Low Discharge Energies

We proceed with an isolated study of the separation between backflow and idealized steady-state models to give a low-level understanding of the performance error introduced by testing in the ground environment. This is the closest analog to traditional facility effect studies [11, 49, 50] in our analysis. We sweep a broad range of ambient neutral pressures ($P_0 \in [10^{-3}, 3]$ mTorr) corresponding to different input values of n_{bf} for constant $n_{n,0} = 9.7 \times 10^{19}$ m^{-3}. As Fig. 5.2 has already informed us, the neutral density evolution is less constrained as the horizontal floor represented by backpressure is reduced. Fig. 5.7 confirms this effect by providing the relative errors between the backflow and steady-state results for the baseline multi-pulse conditions listed in Table 3.1.

Matching data is observed in plots (a) and (b) just like the time-varying I_{sp} and η_R given by Fig. 5.6 to reflect a shared dependence on I_{bit}. The models achieve a maximum relative recapture efficiency error of 58.6% in the limit $n_{bf} \to n_{n,0}$, denoting the backfill case. We then observe a nonlinear decay to sub-percent error at $P_0 = 10^{-6}$ Torr, which is an achievable condition for most turbomolecular and cryogenic vacuum pumping systems. We collect more data points near the backfill condition in the region of greatest model disagreement. Fig. 5.7(c)-(d) indicates higher predicted error in η_m than for η_e.

We have identified a critical test pressure ($P_0^* \approx 0.2$ mTorr) in panel (b) to indicate a relative model error of $\sim 5\%$. Below this value, the backflow and steady-state results closely agree but base pressures become more difficult to achieve in a benchtop setup. Hence, P_0^* represents a reasonable compromise in the tradeoff between test rigor and experimental accuracy. This value offers a rule-of-thumb vacuum requirement of $n_{bf}/n_{n,0} \approx 1/15$ for a low-discharge-energy PIT in a backflow. In plain terms, the backpressure in the chamber should be held at roughly 6.7% of the injected neutral pressure for quasi-steady-state operation. We note that this value scales with the size of the thruster since we approximate the timescale

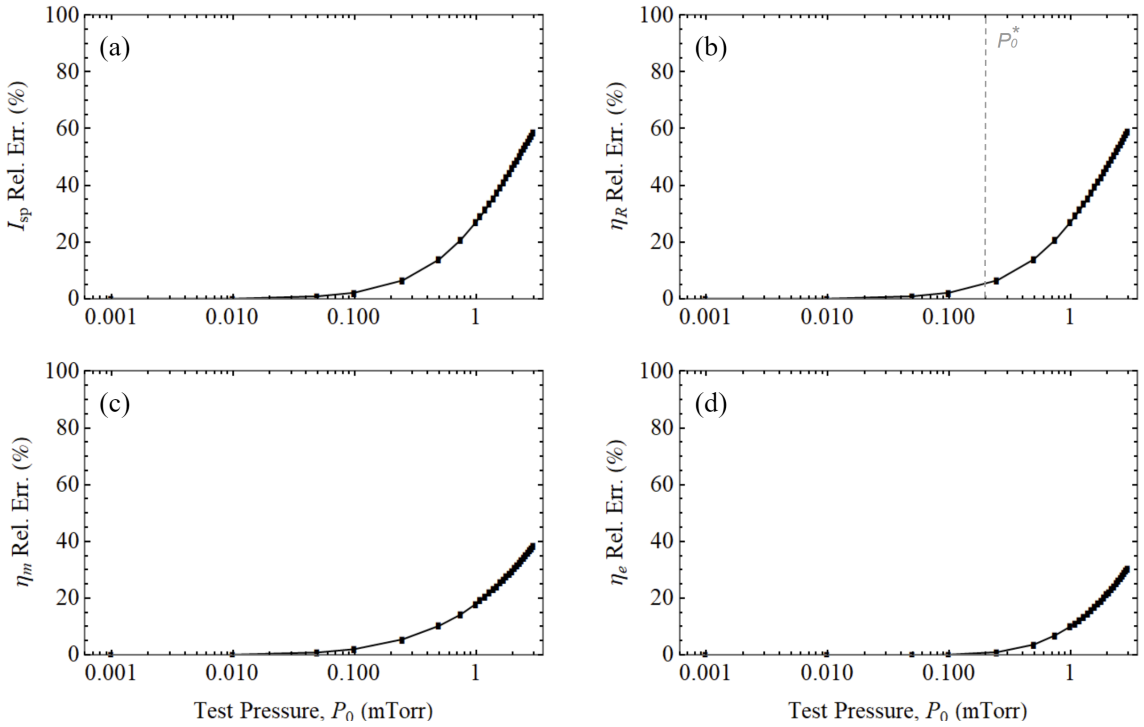

Figure 5.7: Predicted relative performance errors between a backflow condition and steady-state operation across an ambient neutral pressure sweep: $P_0 \in [10^{-3}, 3]$ mTorr. Idealized steady-state results for $n_{n,0}$ corresponding to a peak injected pressure of 3 mTorr are used as the accepted value. A critical test pressure (P_0^*) is labeled to denote a relative error cutoff of 5%.

of pressure equilibration using $r_o = 10$ cm as the characteristic neutral displacement.

In summary, we quantify the effects of higher finite neutral pressures after reinstating the gas valve in a small-scale PIT design. This choice can improve thrust efficiency at the price of system complexity, but a critical test condition emerges from our model to serve as a minimum vacuum capability before inclusion of the gas valve becomes worthwhile. We note that we are analyzing model error which ignores radial expansion and cooling. Hallock [2] has constructed a 2D PIT model to show that radial motion has the general effect of decreasing thrust efficiency, which tells us that it would likely influence the timescale of a backflow.

Chapter 6

EXPERIMENT FOR MEASURING PLASMA SHEET DYNAMICS OF HIPER-PIT

The work presented in this thesis thus far has detailed theoretical efforts that explore complex physical processes and inform future test campaigns. Now, we pivot our discussion to focus on experimental development and analysis of the HiPeR-PIT. This chapter describes the facility equipment and various diagnostics used to obtain quantitative and qualitative information pertaining to current sheet formation and acceleration in a compact planar IPPT operating in single-pulse mode. We outline design choices, materials, power systems, sources of error, and desired measurements relevant to the backfill study of argon propellant.

6.1 Facility Specifications

The vacuum facility used to house the HiPeR-PIT experiment is a 62 cm (2.03 ft) long cylindrical glass chamber with a 25 cm (0.82 ft) diameter. The chamber is sealed by rubber L-gaskets between a stainless steel plate and an acrylic bulkhead containing the inductive coil. Fig. 6.1 gives side-on and gas injection viewpoints of the benchtop configuration to provide a sense of scale for the thruster and its supporting components. The stainless steel plate (right) contains a circular cavity for downstream pressure maintenance at a high throughput.

In this setup, two gas lines were fed into the bulkhead using brass Swagelok tube fittings and manual valves for injection control. Separate gas lines allowed us to modulate the ratio of propellant directed into the central pre-ionization channel while achieving quasi-uniform neutral distributions across the coil face using a foam plenum embedded in the acrylic housing. Base pressures were determined to be limited by imperfect seals in the bulkhead rather than by the vacuum equipment. A minimum backfill of $P_0 \sim 10^{-4}$ Torr was

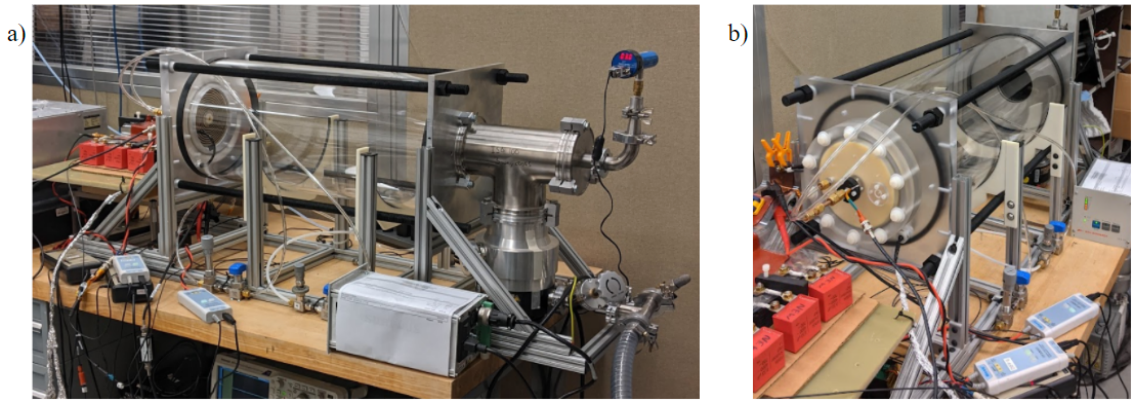

Figure 6.1: Benchtop HiPeR-PIT experimental setup showing (a) side-on and (b) gas injection viewpoints. The thruster uses central (PI) and off-axis gas injection through two separate lines for improved steady fill control. Valves are attached to the rigid structure supporting the chamber, and pressure is maintained by downstream roughing and turbopumps. The brassboard PPU is installed ahead of the coil where three capacitors (red) are connected in parallel to form the main bank. Not shown are the oscilloscopes, RF controller, and two 5-kV power supplies.

maintained by an Edwards RV12 roughing pump and a 510 l/s turbopump with Edwards EXC120 controller; however, all tests were conducted with argon mass flow rates giving pressures in the millitorr range. These conditions were monitored with an accuracy of ±5% by a Varian Multi-Gauge cold cathode board.

6.2 HiPeR-PIT Characteristics

As introduced in the first chapter of this thesis, the HiPeR-PIT design aims to overcome many of the traditional shortcomings of IPPTs by achieving sufficiently high pulse rates to utilize both steady gas injection and lower discharge energies. Our backfill study demonstrates that testing these engineering goals with high fidelity at timescales short enough to resolve microscopic processes within the plasma sheet is viable. Now, we provide the physical details that could empirically realize these findings.

6.2.1 Inductive Coil

The design of an optimal small-diameter coil with $L_c \in [0.2, 0.5]$ μH and minimal stray inductance is an ongoing area of development. For the results presented in this thesis, the driver utilized two five-turn windings where symmetric Archimedes spirals were set in parallel to achieve $L_c = 2 \pm 0.02$ μH and $L_0 = 0.6$ μH as measured by a BK880 precision LCR meter. The coil was constructed out of 660/42 Litz wire (equivalent to 11 AWG) to reduce skin effects at high AC frequencies and was insulated in 0.5 mm heat shrink to protect against ionized propellant. This geometry had $r_o = 7.5$ cm and $r_i = 2.25$ cm with 2.5 mm of separation between windings to reduce mutual inductance effects.

6.2.2 Plasma Source

Since the HiPeR-PIT leverages low discharge energies per pulse relative to the state-of-the-art in IPPT technologies, we have found that a two-step pre-ionization approach offers favorable formation properties without a significant detriment to current sheet residence time [13]. This entails the joint use of central RF power and a separate, antecedent pulse from a smaller capacitor bank triggered only a few cycles before the primary acceleration discharge. Our PI scheme incorporated a $30 - 40$ W RF power generator and matching network and a 0.022 μF snubber capacitor linked to a separate DC power supply.

6.2.3 Power Processing Unit

A benchtop implementation of a paralleled boost converter design is under development alongside the HiPeR-PIT to research the operation and performance of a high-pulse-rate PPU [48]. This work is beyond the scope of this thesis, but we note the highlights of the setup in order to provide an understanding of the electromagnetic energy supplied to the thruster.

A Glassman DC power supply was used to slowly charge a large film, 1460 μF capacitor to a nominal voltage between $120 - 200$ V, which served as the backing bank. Two 1700 V, 182

A silicon carbide (SiC) Schottky diodes were connected in series to comprise boost cells with blocking up to 3400 V and high thermal durability. Custom gate driver boards were used to control two 6500 V, 200 A Infineon IGBTs denoting the boost cell switches. These offer low stray inductance and switching losses at fast switching times with improved overvoltage protection. The main bank consisted of three 0.33 μF snubber capacitors connected in parallel to give $C_0 \approx 1$ μF. A second 3300 V, 800 A IGBT in a high-side configuration was used for the discharge switch, and non-inductive ceramic resistors provided the circuit load.

Connections between circuit elements were made using wide, 0.89 mm (0.035 in) thick copper busbar. Outgoing and return lines across the full architecture were paralleled and held within a few millimeters to reduce L_0 across the system. Still, the preliminary HiPeR-PIT test article carried a high parasitic inductance relative to other PIT prototypes.

6.3 Diagnostics

Several diagnostic tools and methodologies are refining the HiPeR-PIT project to utilize different types of information for understanding physical phenomena. Only a handful of these are relevant to the backfill study; namely: a Rogowski coil, a B-dot probe, and an intensified charge-coupled device (ICCD) high-speed camera.

At an overhead level, the PPU, camera, and data collection devices were all controlled by a QC9520 pulse generator via Ethernet connection with a desktop computer. Signals were used to trigger Tektronix DPO5054, TDS3034B, and TDS2024B digital phosphor oscilloscopes for high-frequency monitoring of voltage and current waveforms. The Rogowski coil was implemented in the style of Polzin [23] to measure high levels of current without impacting the circuit inductance of the experiment.

6.3.1 Probes

Voltage Probes

Measurement of the time-varying voltages of the multiple capacitor banks in the boost converter design was performed using four Pintech PT8020 and two Micsig DP20003 high-voltage differential probes. Each of these probes was radio-frequency compensated with a bandwidth of 100 MHz. Depending on the input voltage of a given test regime, output was attenuated by a factor of either 100 or 1000 to display and record the waveforms of various capacitor voltages on the fast oscilloscopes.

Magnetic Field Probes

There was an attempt to measure the time-varying induced magnetic fields of the HiPeR-PIT coil using a B-dot probe as outlined by Polzin *et al.* [69]. The concept behind this diagnostic was to self-generate an output voltage to give a raw value of $\partial\mathbf{B}/\partial t$ which can be integrated to find $\mathbf{B}(t)$ and $\mathbf{J}(t)$ indirectly via Ampère's law. The probe was constructed by embedding eight 5.6 μH chip inductors in a 3D-printed ring sharing the same outer radius as the drive coil, each spaced evenly in the azimuthal direction. The coil was then insulated using thermal epoxy and silicone tape such that magnet wire connected in twisted pairs to each chip terminal could be directed in a single shielded strand through the acrylic bulkhead.

Our early testing determined that this probe design was faulty and confounded the data in multiple ways. Insufficient shielding caused some of the acceleration coil energy to be coupled to the B-dot loop, which was visibly evident as greater luminosity appeared at the circumference of the thruster. Time-dependent output waveforms failed to match expected peak times given higher-fidelity current and voltage data, and the lead wire obstructed plasma photography as we will discuss below. In effect, the presence of this probe caused much of our data to be unreliable and it will need to be redrafted in future studies.

6.3.2 ICCD Photography

Visual evidence of current sheet formation and axial translation were captured using the Teledyne PI-MAX 4 ICCD. High-speed gating offered us extremely sensitive image resolution to give relative intensities within the plasma exhaust at sub-microsecond timescales. We looked side-on at the 1D profiles of current sheets in a similar manner as Polzin [23] and Li *et al.* [70] at various time increments past the delay of the pulse generator. This effectively gave us the spatial and temporal histories of a small set of state variables for comparison to our 1D model output.

Fig. 6.2 provides a cropped image of the coil face with various labeled components and the ICCD position to give a better idea of the experimental vantage. As mentioned, the B-dot coil resided at the outer circumference of the inner windings and gas distribution channels were etched between the insulated Litz to provide steady inter-coil injection. The ICCD was positioned on the outside of the transparent chamber along the centerline of the thruster at roughly $z = 0$ to track 1D plasma motion from the reference plane.

The photographs were obtained without implementing narrow linewidth filters, so all light emission from the plasma was detected. Hence, the glow of the pre-ionized RF plasma was captured ahead of the primary discharge. Images were taken with an exposure time of 0.5 μs and a focal ratio (i.e. "fstop") of 11.

6.4 Measured Parameters

The spatiotemporal evolution of current sheet formation and acceleration was collected to give 1D exhaust dynamics for a test article with known circuit parameters, thruster geometry, propellant properties, and gas profile. The steady injection of neutral argon at low mass flow rates gave regimes that could be modeled using our improved numerical model with variable mass entrainment. Multiple plasma discharges at the same input voltages and chamber pressures proved to be approximately repeatable according to visual data, which was important to the validation of the benchtop HiPeR-PIT.

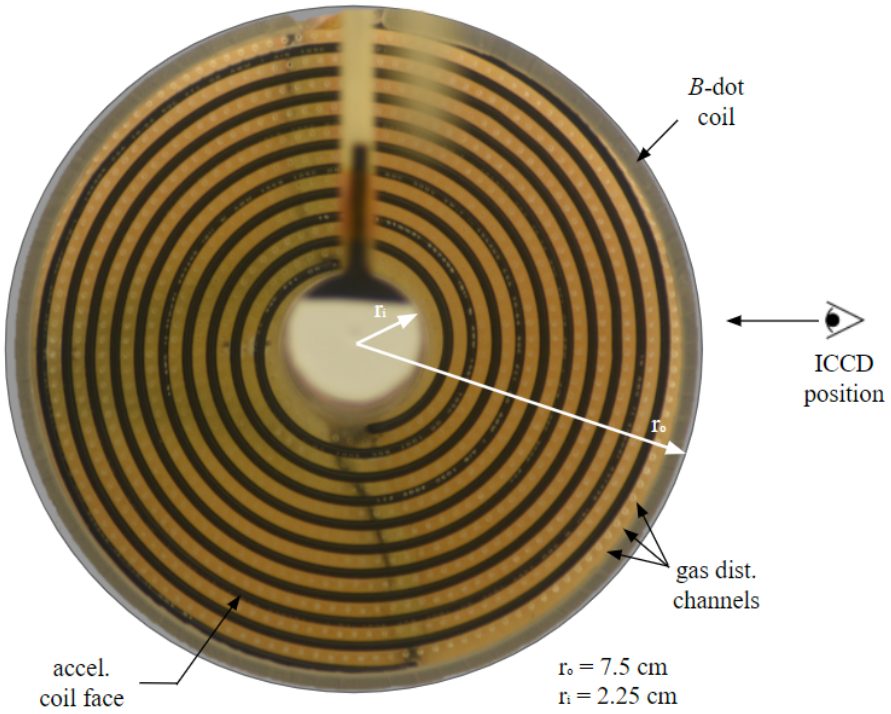

Figure 6.2: End-on schematic of the HiPeR-PIT coil face highlighting the ICCD imaging plane to the side of the chamber. Inner and outer radii are labeled to give scale to the two-spiral coil design. The B-dot coil is wrapped around the edge of the thruster to provide magnetic field measurements at varying azimuthal locations.

Specifically, our setup allowed us to approximate the time-dependence of z_s, w_s, and v_s by tracking the trailing and leading edges of the current sheets at a critical intensity threshold relative to the image background. We were also able to collect the relative intensities at each time increment to get an idea of peak density and diffusion processes later in the pulse. Images were globally normalized for fixed V_0 and P_0 with minor compensation for pressure drift over an extended collection window.

To ultimately compare the visual data with our model output, we had to find the coupling distance of our inductive coil. This entailed fastening a conductive, aluminum disc to a Thorlabs tri-axis translation stage ahead of the coil and measuring the effective inductance

of the lumped system at low discharge energies. The disc modeled a plasma slug with uniform conductivity, so by adjusting its axial separation we were able to determine z_c in the style of Martin and Eskridge [42] (see Fig. 4) using Eqs. (2.7) and (2.11).

Significant sources of error in this study included inexact current sheet boundaries, obstructions within the ICCD field of view, and higher coupling near the outer circumference at the B-dot coil. The coil was offset from the axial boundary of the imaging plane at $z_a \approx -2$ mm, making it difficult to view the early stages of plasma formation.

Chapter 7

HIPER-PIT PLASMA SHEET ESTIMATES

The previous chapter details the preliminary HiPeR-PIT design and experimental setup that enable an approximate measurement of plasma sheet dynamics in a backfill. We now explain the processing algorithms used to reduce the visual data acquired by the ICCD camera and present the results of a single temporal sweep across the first three half-cycles of the primary capacitor discharge. Initial qualitative observations are shown first to demonstrate the formation and profitable acceleration of a low-voltage, inductively-coupled current sheet. Then, raw quantitative data is distilled from each photograph to show the intensity profile of the plasma in both the axial and radial planes. A tabular summary of HiPeR-PIT conditions corresponding to ICs in our 1D backfill model is given to contextualize a subsequent comparison of theoretical and experimental results. We comment on the sources of error and ultimately conclude that the model is more reliable than the preliminary ICCD findings.

Again, the working gas for the data was argon. Multiple different backpressures were used across our preliminary test campaign, but we have provided the largest data set at $V_0 = 3$ kV and $P_0 = 2.25$ mTorr, corresponding to a pulse energy of 9 J. The demonstration of inductive coupling at pulse energies this low was notable in itself, but an even lower data set collected at 4 J is depicted in Appendix C. Across all testing, it was observed that the pulse-to-pulse repeatability of the experiment at fixed conditions was high according to visual results and oscilloscope measurements, allowing us to stitch together multiple pulses to represent a single pulse at many sampling points in time. It was noted that higher voltages yielded better photographic evidence of plasma sheet formation, which agreed with Polzin's current rise rate requirement. We also discerned the formation of a secondary current sheet beyond the first half-cycle of capacitor ringdown, as predicted by the literature.

7.1 Image Processing

All photographs captured by the ICCD were imported and processed in LightField prior to our own post-processing adjustments provided in Appendix A. Minimum intensities were parsed from each converted tag file and then subtracted from the original image for individual correction. The maximum intensity value across a full sweep of representative frames was then parsed and divided from each pixel to normalize the photographs in each data set. The maximum intensity of the PI-MAX 4 was taken to be 65000 a.u., which we then divided from each pixel in the corrected images to yield a globally normalized data set. For bi-directional intensity comparisons, we mapped each pixel grid in the horizontal ($\hat{z}$) and vertical ($\sim \hat{r}$) directions and sampled along the centerline of both axes. As seen in the frames below, this gave a limited view of the full sheet physics, but was necessary to approximate along a 1D reference with minimal obstruction.

The horizontal intensity profiles gave us the ability to calculate time-dependent z_s, w_s, and v_s by estimating the leading and trailing edges of the current sheets in 1D. We truncated each data set to examine frames with clear formation and a discernible, finite sheet width. Hence, we set $t = 0$ at ~ 8.7 μs after signal generation, which aligned closely with the second I_c peak for an LC-period of $\tau_{LC} \approx 8.9$ μs. Only fourteen data points separated by the ICCD exposure time were gathered for a full sweep so as not to be confounded by the formation of a secondary current sheet. Data was converted from pixels to meters using the obstructing bulkhead as a visual reference, which spanned roughly 200 px and was hand-measured at 4.25 cm thick. Sheet velocity was calculated from sheet position using a first-order approximation, $v_s = \Delta z_s / \Delta t$, where $\Delta t = 0.5$ μs between points.

7.2 ICCD Results

Representative, processed photographs of experimental plasma sheets at various time increments past signal generation are given in Fig. 7.1 as an array to show the formation and acceleration processes across more than a full LC-period of the inductive drive coil. These

images correspond to $V_0 = 3$ kV and $P_0 = 2.25$ mTorr with a gradual pressure drift due to upstream equilibration in the gas line such that $P_0 \approx 2.5$ mTorr by the final pulse. We note that there are obstructing opaque objects in each frame; most notably: the acrylic bulkhead, rubber L-gasket, and shielded B-dot probe wire.

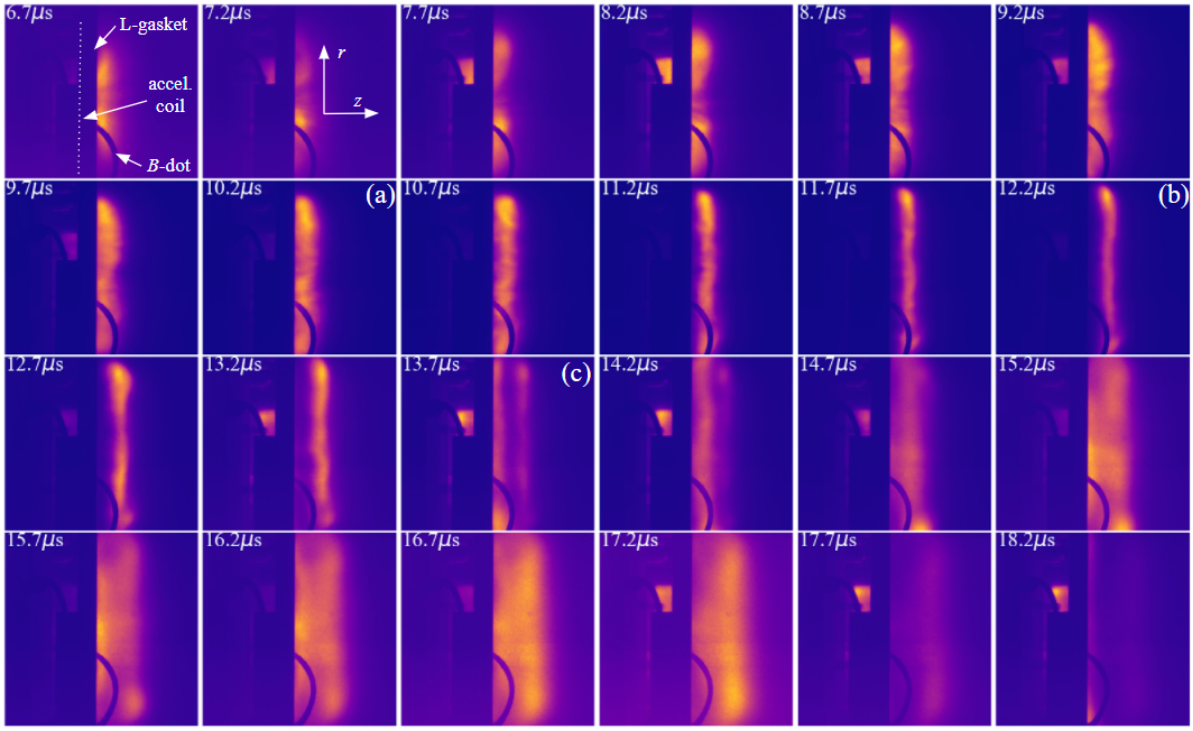

Figure 7.1: Representative image frames of experimental plasma sheets at discrete time increments during the first three half-cycles of capacitor discharge for $V_0 = 3$ kV, $P_0 = 2.25$ mTorr. Photograph (a) marks the formation of a well-developed sheet, (b) corresponds to minimum w_s, and (c) shows the formation of a secondary sheet due to maximum negative I_c. The circular obstruction in the bottom of each frame is the B-dot probe connection.

High contrast within the representative frames allows us to observe the pre-ionization and formation phases ($\sim 6.7 - 10.2$ μs), the acceleration phase ($\sim 10.2 - 13.7$ μs), and the formation of a secondary current sheet with higher snowplow losses ($\sim 13.7 - 17.2$ μs). Frame (a) marks the point in time corresponding to the highest intensity values as shown in Fig. 7.2, which we take to represent the formation of a well-developed sheet. This frame shows us

that the plasma is still in close proximity to the inductive coil and is likely brightest due to active coupling with the electromagnetic fields and high relative density. Between panels (a) and (b), we find valuable axial translation and a continual compaction of sheet width before achieving a minimum w_s at 12.2 μs. This is indicative of low entrainment losses through the acceleration phase, after which downstream diffusion takes effect. Panel (c) provides a clear depiction of a secondary current sheet while the primary plasma is still visible.

The frames in Fig. 7.1 show varying levels of non-uniformity across both $\hat{z}$ and $\hat{r}$ with spatial anomalies near the B-dot probe connection. These are likely due to unintentional coupling between the plasma and the probe as we have previously discussed. Since a uniform plasma is a key assumption in our numerical model, we anticipate that this will produce slight discrepancies in our comparison below. Analysis of instabilities and filamentation is beyond the scope of this thesis, but worthy of note in assessing thruster inefficiencies and current sheet permeability.

The secondary sheet is also worth cursory discussion as the HiPeR-PIT is the first prototype to demonstrate this phenomenon below a discharge voltage of $\sim$ 15 kV. Steady gas injection results in higher gas densities near the coil face during the second half-cycle of the capacitor ringdown [13], which increases the probability of secondary sheet formation as demonstrated by Li *et al.* [70]. We note that panel (c) marks 5 μs past our designated $t = 0$, so with shorter exposure times this likely aligns exactly with the second half-cycle underlying Fig. 7.1. MHD simulations by Che *et al.* [57] have indicated that a secondary sheet can contribute as much as 20% of the total impulse bit with pulsed gas injection, so this is a significant process that deserves future examination in the benchtop configuration.

We examine the corrected intensity data of each frame in Fig. 7.2 to show the relative brightness of the current sheets along two planes. These panels fit quantitative information to our qualitative results in order to concretely measure trends within the pulse. Each plot shows a pixel spread from 0 to 1000 to give the image location of mapped intensity data along the centerline of both planes. Intensity along $\hat{z}$ (blue) is sampled from west to east, whereas $\hat{r}$ (orange) is taken from north to south. We maintain the panel labels of Fig. 7.1 to

emphasize the critical developments along the time-evolution of the pulse. Note that major discontinuities exist in the data due to the obstructing bulkhead, L-gasket, and B-dot probe connection. Significant noise exists at higher intensities from the exacerbation of spatial non-uniformities close to the coil face.

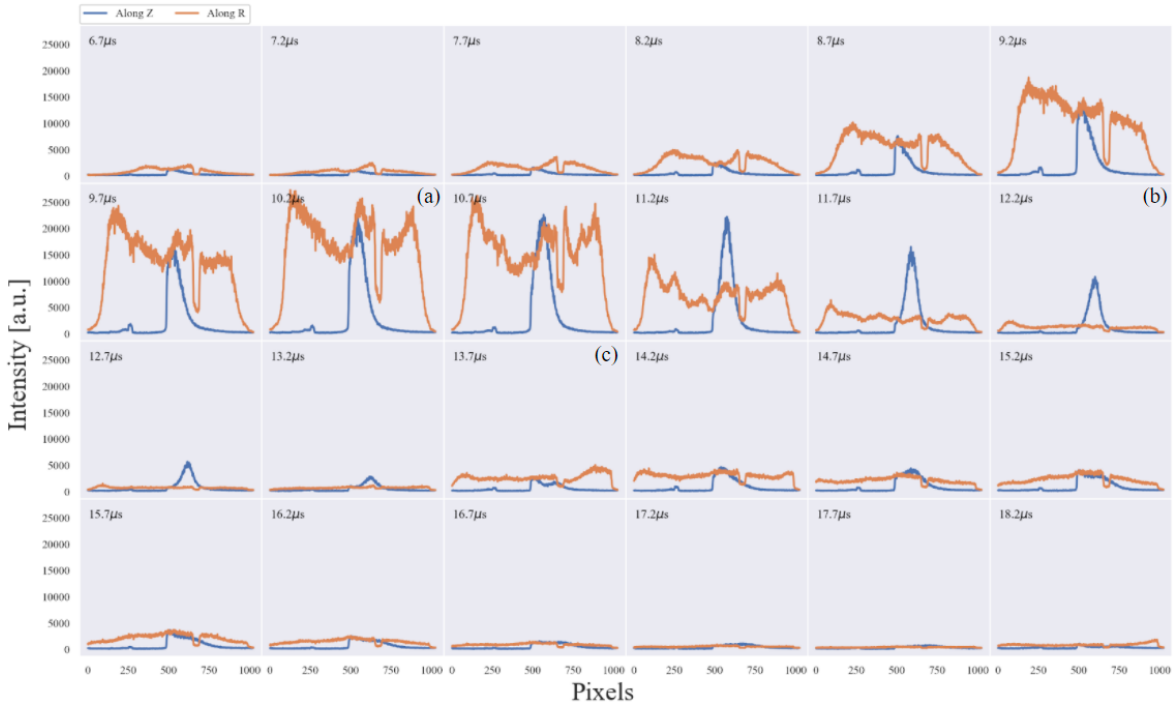

Figure 7.2: Relative intensities along $\hat{z}$ and $\hat{r}$ collected by the PI-MAX 4 ICCD camera corresponding to frames from Fig. 7.1 for $V_0 = 3$ kV, $P_0 = 2.25$ mTorr. Intensity magnitude quantifies the electromagnetic coupling between the plasma and the coil. The pixel position of peak intensity in $\hat{z}$ (blue) depicts the axial propagation of current sheets over time. Empty intensities along $\hat{z}$ for px $\in [275, 475]$ correspond to the bulkhead and L-gasket, and sharp discontinuities in $\hat{r}$ (orange) result from the obstructing B-dot probe wire.

The evolution of intensity along $\hat{z}$ depicts the 1D current sheet dynamics that align with our model. We find that the bulkhead and L-gasket obstruct key data for px $\in [275, 475]$, which limits our examination of the pre-ionization and early formation phases. Peak intensity grows until it reaches a maximum value at 10.2 μs in panel (a), after which we observe

translation of the peak as the current sheet propagates away from the coil. The width of the sheet is captured by the separation of the intensity curve from the ambient floor. Panel (b) exhibits a high level of compression while the peak intensity is still substantial. We observe that intensity diminishes between $12.7 - 13.2$ μs before rising again in (c), marking the appearance of the secondary sheet at the second half-cycle.

Along $\hat{r}$, we observe somewhat higher intensities than along the centerline in $\hat{z}$. We generally observe the brightest regions of plasma in the northern part of the current sheet, given by the first peak in the curve. The physics underlying this trend are unknown, but we note that significant deviations along $\hat{r}$ could be artifacts of coupling with the B-dot probe or other instabilities.

In the FARAD proof-of-concept experiment, Polzin [23] suggested fitting a Gaussian distribution to the raw intensity waveform of similar measurements. We have foregone this method here since the data represent preliminary findings and several viewing obstructions confound the results. For future HiPeR-PIT experiments, this technique could be used to more accurately determine the 1D time-dependent motion of the sheet. Density measurements could be collected by a Langmuir probe and placed on an arbitrary scale to better assess the entrainment process.

7.3 Model Comparison

Figs. 7.1 and 7.2 provide the groundwork for several lines of analysis that could explore the relationships between circuit architecture, coil design, neutral backpressure, current sheet microstructure, and subsequent plasma dynamics. We proceed with a simplified 1D comparison to test model conformity with preliminary experimental results. The aim of this endeavor is to assess our image processing techniques and to locate early sources of error to inform future test campaigns since the simulation has already been validated by higher-fidelity data in PIT literature.

Table 7.1 summarizes the experimental input conditions and HiPeR-PIT parameters discussed in the previous chapter to contextualize the ICs passed into the model. Some high-

lights to note are the high stray and coil inductances, which yield a slow current rise rate and low circuit damping ratio. χ_0, $w_{s,0}$, and $T_{e,0}$ were estimated based on 30 W of RF power and the parameters used by similar small-scale designs [23,41]. Without the L-gasket obstructing the view of the early pre-sheet, $w_{s,0}$ could be measured directly from the visual results.

Table 7.1: Experimental input condition estimates for the benchtop HiPeR-PIT test article at $P_0 = 2.25$ mTorr and $V_0 = 3$ kV. Data collection took place during the fall of 2021 using outmoded bulkhead and coil designs, so parameters listed below represent points to improve.

Input	Value	Input	Value	Input	Value
V_0	3 kV	$T_{e,0}$	10 eV	$z_{s,0}$	0 m
C_0	1 μF	$T_{i,0}$	0.1 eV	$w_{s,0}$	5 mm
R_c	5 mΩ	T_n	0.026 eV	$n_{n,0}$	7.3×10^{19} m^{-3}
L_0	600 nH	r_o	7.5 cm	z_a	-2 mm
L_c	2 μH	r_i	2.25 cm	z_c	1.5 cm
χ_0	0.01	z_n	1 cm		

7.3.1 Results

Fig. 7.3 depicts the theoretical and experimental overlay for time-dependent sheet position, width, and velocity. Broadly speaking, the backfill model displays poor agreement with the data collected by the ICCD, particularly at peaks and troughs in the current waveform at $t/\tau_{LC} = 0$ and $t/\tau_{LC} = 0.5$. Error bars are given to quantify the uncertainty associated with values parsed from Fig. 7.2. As seen, error decreases as the plasma condenses and z_s and w_s are more easily distilled from qualitative results.

Sheet position exhibits rough agreement in Fig. 7.3(a) as both results grow at the same order of magnitude over time, but the model predicts greater axial translation than we observed across the HiPeR-PIT sweep. For the conditions listed in Table 7.1, the backfill model yields a brief but powerful acceleration phase for $t/\tau_{LC} < 0.1$ before the argon sheet begins to decelerate over the course of neutral ingestion. Panel (c) emphasizes the discrepancies seen in (a) by telling us that the first two data points gathered by the ICCD represent a

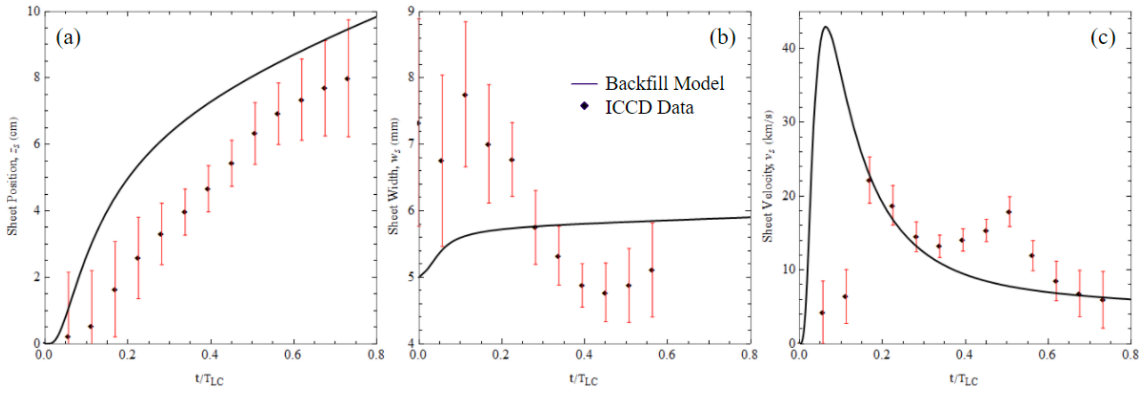

Figure 7.3: Photographically measured sheet position, width, and velocity as functions of time overlayed with 1D model predictions for HiPeR-PIT input conditions listed in Table 7.1. Data is discretized by frame for $\tau_{LC} \approx 8.9$ μs. Error bars indicate higher uncertainty during the formation phase due to visual obstruction and greater intensity variance. These are preliminary experimental results, so the model is considered higher fidelity.

low-velocity startup rather than a high-impulse growth. The experimental sheet ultimately decelerates at roughly the same rate as the predicted result, but with a smaller final position in z by approximately 1.75 cm. The disagreement seen across the latter majority of the pulse could follow from initial error associated with startup corresponding to 8.7 and 9.2 μs in Figs. 7.1 and 7.2.

Sheet width is blatantly nonconformant across the early stages of the pulse for $t/\tau_{LC} \lesssim 0.2$. High errors of approximately ± 1.6 mm are depicted to express the unreliable measurement of sheet boundaries for intensity curves in this span. We also observe that the theoretical and experimental results exhibit different trends for w_s in regions of higher fidelity. The model predicts a continual widening of the sheet over time, whereas the visual results indicate that significant compression takes place before achieving a minimum $w_s \approx 4.77$ mm at the second half-cycle of the discharge. We portray fewer measured data points in panel (b) because w_s loses clear visual boundaries after the formation of the secondary current sheet. Based on the sub-millimeter growth of w_s according to the model, we are assured in the initial estimation of $w_{s,0} = 5$ mm.

The velocity comparison exhibits varying levels of agreement across multiple spans within the pulse. Unexpected discrepancies arise in the experimental data for $t/\tau_{LC} \in [0.35, 0.6]$ such that a local maximum appears at roughly the second half-cycle of capacitor ringdown. This could be an error resulting from measurement inaccuracy, but may also be a true effect associated with secondary sheet formation. Future backfill testing should examine this region with higher scrutiny across a wider variety of input conditions.

7.3.2 Sources of Error

Beyond the assumptions made in the formulation of our 1D PIT model, there are several sources of experimental error that confound the comparison made in Fig. 7.3. We summarize the three primary concerns below:

1. Visual interference: intensity data corresponding to $t/\tau_{LC} \lesssim 0.1$ was confounded by the L-gasket obstructing the side-on view of the ICCD near the coil face. Since the initial position of the plasma was assumed to be flush with the gas injection plane, the first three data points were erroneous.

2. Sheet width estimation: It is clear from the frames in Fig. 7.1 that w_s carries a degree of uncertainty if we merely define it as the span between the leading and trailing edges of the current sheet. Once significant lateral diffusion or entrainment losses occur, these boundaries become difficult to define. We used an approximate method, and have yet to formulate a means for assessing the time-evolution of skin depth. $\delta_{s,0} > w_{s,0}$ due to increased plasma resistivity, which further confounded the first few data points.

3. Secondary sheet formation: the PIT model only considers a single plasma per discharge for steady gas injection. No 1D theoretical efforts thus far have quantified the effects of secondary sheet formation and its influence on thruster performance. The experiment demonstrated that this behavior was critical to system evolution in a backfill.

It should be noted that the HiPeR-PIT operated without the use of inductive recapture. Additional switching could prevent the formation of a secondary current sheet, which would promote better alignment between the model and the experiment. Although the simulation can be adjusted to maintain the closure of the switch throughout the pulse, the variables presented are largely unaffected by voltage latching during the first half-cycle of the discharge anyway. Small ripples in the current waveforms were also observed, which could have been attributable to the use of an additional, parallel capacitor for the PI bank, as postulated by Polzin *et al.* [71]. These effects were assumed to be insignificant to the given analysis, and examination thereof is beyond the scope of this thesis.

7.3.3 Implications for Experimental Design

In light of the errors introduced by the preliminary experimental setup and data reduction methods used above, we offer recommendations for improving the efficacy of ICCD-based visual analysis of the HiPeR-PIT exhaust. Some of the items below are already in progress at the time of this thesis publication.

- Remove the B-dot coil to prevent irregular coupling at the coil circumference and visual interference in the radial direction. Future implementation should aim to reduce the proximity error given by Polzin *et al.* [69].

- Machine a new acrylic bulkhead to extend the coil further into the chamber past the L-gasket. No component or diagnostic in the setup should obstruct the side-on view of the gas injection plane and coupling region.

- Fit a Gaussian distribution to the intensity data along $\hat{z}$ for a more accurate statistical assessment of sheet position.

- Test the HiPeR-PIT in a backfill both with and without the use of inductive recapture. The formation of a secondary current sheet is worthy of extensive analysis, but should be excluded for the purpose of model comparison.

- Maintain the primary input voltage and focal ratio of the ICCD while adjusting the backpressure to determine peak intensity at a given V_0. This should correspond to a peak plasma density according to the model. This would be an effective means to validate the trends observed by the backfill study. Repeat this analysis for fixed pressure and variable voltage.

- Using a low primary input voltage, decrease the rate of steady gas injection until sheet formation does not occur. This could provide an effective benchmark that would inform the model boundaries, similar to the coil inductance study in Section 2.7.

- ICCD results are particularly useful in diagnosing $z_{s,0}$. Examine different parameter spaces to test the assumption that the current sheet initially forms at the gas injection plane for steady throughput.

Chapter 8
CONCLUSION

In this thesis, we have formulated a 1D model of plasma sheet formation and acceleration in a planar IPPT using a lumped-element circuit description and time-dynamic fluid equations that capture propellant physics at the particle level. The incorporation of non-equilibrium ionization, a finite skin depth, and variable neutral entrainment has allowed us to forecast the dynamics of thruster exhaust with a high degree of theoretical fidelity. This has prompted the introduction of a new dimensionless scaling parameter that predicts the quality of sheet formation based on electrical energy deposition in the electron population. We have constructed the numerical simulation to take the neutral gas profile ahead of the coil at the time of capacitor discharge as an initial condition, affording the examination of multiple, consecutive pulses at various test conditions in an unsteady operating mode.

By comparing plasma dynamics for steady propellant injection and static fill, we have ultimately offered an analysis of some effects associated with removing the gas valve ahead of the inductive driver in a low-discharge-energy, high-pulse-rate PIT design. We have quantified the differences between idealized steady-state solutions to the 1D model and those produced by testing the same thrusters in a backfill to evaluate the utility of future experimental campaigns at a relatively high chamber pressure. A modified inter-pulse equilibrium has been proposed and analyzed for testing at lower base vacuums with unsteady neutral injection, yielding a recommended facility requirement to reduce error for hypothesized design regimes.

We have also described the experimental setup and results of preliminary testing on the UW HiPeR-PIT benchtop prototype, and have outlined near-term improvements by comparing approximate data with the 1D numerical model. The inductive pulsed plasma

thruster is still at a low level of technological readiness compared to other EP devices, so the goal of our effort has been to inform future research directions rather than to empirically quantify the facility effect of a finite neutral backfill. We summarize the results of our work below, and conclude with a brief proposal of advancement paths.

8.1 Summary of Analytical Modeling Results

Before we compile our primary takeaways, we should note that a number of simplifying assumptions were made throughout the derivation of both the single- and multi-pulse descriptions of PIT operation. Firstly, the properties of the plasma were assumed to be uniform across the finite sheet volume which directly contradicted the findings of previous research [17, 32–34], as well as our own visual results. A meaningful attempt at modeling filamentation and plasma anisotropies would require extending the formulation to higher dimensions. Next, the equation for the evolution of sheet width for time-varying neutral entrainment was derived from phenomenological arguments rather than first principles. We have also used a semi-empirical constant to relate the electromagnetic transparency of the exhaust to the ratio between skin depth and sheet width, but this has only appeared in our analysis of scaling trends. Last and most importantly, our analysis has neglected the presence of higher ionization states and recombination reactions. Previous efforts invoking the Saha equilibrium [43, 57] have predicted the former, but the reaction timescales are generally slower than the plasma residence time at $T_e \lesssim 50$ eV. We have limited our analysis to regimes that avoid these levels of heating.

In our inter-pulse model, we have constrained the neutral diffusivity constant so as to limit the evolution of neutral density below the peak injected value. We have also neglected radial expansion and cooling, which have been shown to be significant over larger timescales [2, 38, 53, 55]. In our proposed "backflow" condition, we have assumed that the vacuum system is able to regulate pressure on a similar timescale as the pulse repetition rate.

With all this in mind, we amalgamate the key insights of Chapters 2 through 5 below, which explore the dynamic effects of various model parameters and test conditions:

- Plasma electron temperature displays rich dynamics at short timescales due to the competing effects of Ohmic heating and inelastic losses. The dimensionless scaling parameter offered by Little *et al.* [58] uses this behavior to effectively predict the quality of current sheet formation and offer a critical design threshold in the single-pulse regime.

- Varying the mass flow rate in a multi-pulse operating mode changes the rate at which the thruster reaches steady state. In general, higher propellant mass entrainment requires a greater number of pulses to reach an unsteady equilibrium.

- Charge-exchange collisions become more common in steady-state PIT operation due to the increased presence of downstream neutral particles. This also leads to an increased collisional drag force and significantly lower exhaust velocities.

- The majority of state properties across backfill and quasi-steady-state conditions agree within a close tolerance across the time-duration of a pulse, but with different underlying species densities and energy partitioning acquired during deceleration. The evolution of neutral density in a steady-state equilibrium yields identical conditions to a backfill near the coil face.

- When testing in a backfill, higher charge voltages yield better mass entrainment and offer more efficient sheet formation up to a critical limit. However, the resulting plasmas will always be semi-transparent to the AC fields of the coil and upstream neutrals. Increased backpressures require greater discharge voltages to generate well-formed sheets.

- A small-scale PIT design using steady gas injection sees an exponential falloff in test error with decreasing chamber pressure. A critical vacuum condition relative to the injected neutral density emerges for a given set of design parameters.

- The xenon propellant model predicts denser, slower-moving plasma sheets than argon

for the same input conditions. This promotes better impermeability to the AC fields of the inductive coil and greater electromagnetic coupling for both single- and multi-pulse modes.

8.2 Summary of Preliminary Experimental Results

Since the data was confounded by multiple factors in our preliminary visual examination of HiPeR-PIT exhaust, we summarize the findings and but place greater emphasis on their implications for experimental design.

- The formation and axial acceleration of compact current sheets was captured by an ICCD for discharge energies below 10 J, depicting similar phases of plasma generation and motion as the 1D model. Raw visual data exhibited significant spatial non-uniformities along the radial direction.

- Steady gas injection led to the formation of secondary current sheets at the second half-cycle of the coil current waveform, which may have affected the primary sheet velocity according to the processed image intensity distributions.

- Preliminary current sheet dynamics at a single input voltage and backfill pressure exhibited poor agreement with the output of the numerical model, which was largely caused by sources of error in data collection.

- Several paths for reducing the error associated with ICCD measurements were provided, to include: removing visual obstructions, machining a new bulkhead, and processing the data using a Gaussian fit.

8.3 Future Work

Throughout this thesis, we have alluded to different paths for improving both the fundamental understanding of the plasma physics relevant to PIT operation in different ambient

conditions and the engineering methods used to assess these findings on a small-scale prototype. The realization of Chapter 4 is that while steady gas injection and testing in a backfill may affect the performance of the thruster, many state properties are consistent enough with idealized models to draw representative conclusions from less rigorous systems and setups. New methods [72] for measuring the thrust component generated by a particular acceleration mechanism are under development, and could be used to empirically define the effect of a neutral backfill going forward. Since the data presented in Chapter 7 leave come conclusions to be desired, significant work remains in validating the 1D model. We divide the research into two main camps, listed below:

1. Model development: the inclusion of higher ionization states and recombination reactions would be critical to the examination of a broader input spectrum. In its current form, the analysis would benefit from further parameter sweeps to optimize a more complete region of thruster design conditions (e.g. damping ratio, z_a, z_c, etc.). Pressure-varying γ and temperature-varying collisional cross sections could also be implemented to improve the accuracy of energy transfer. The inclusion of greater plasma chemistry to extend the propellant models to molecular gasses would be ambitious, but ultimately quite useful in the analytical exploration of hydrazine and various in-situ resources for future missions.

2. HiPeR-PIT validation: the repeatability of the HiPeR-PIT experiment could provide several opportunities for measuring system scaling trends and estimated values. It should first be determined whether operating with inductive recapture precludes the formation of a secondary current sheet. Then, the discharge voltage and backfill pressure could be adjusted across a wide parameter space to investigate 1D sheet dynamics and threshold conditions for effective plasma formation and acceleration. The use of a Langmuir probe to provide a baseline sheet density would expand the predictive utility of photographic intensity data, but a time-accurate method for defining a finite sheet width would be equally as important.

BIBLIOGRAPHY

[1] R. G. Jahn, *Physics of Electric Propulsion*. New York, NY: McGraw-Hill, 1968.

[2] A. K. Hallock, *Effect of Inductive Coil Geometry on the Operating Characteristics of a Pulsed Inductive Plasma Accelerator*. PhD Thesis, Department of Mechanical and Aerospace Engineering, Princeton, Univ., Princeton, NJ, 2012.

[3] R. J. Goldston and P. H. Rutherford, *Introduction to Plasma Physics*. New York, NY: Tayler & Francis Group, 2000.

[4] D. M. Goebel and I. Katz, *Fundamentals of Electric Propulsion: Ion and Hall Thrusters*. Pasadena, CA: California Institute of Technology, Jet Propulsion Laboratory, 2008.

[5] S. Mazouffre, "Electric propulsion for satellites and spacecraft: Established technologies and novel approaches," *Plasma Sources Sci. Technol.*, vol. 25, no. 033002, p. 27, 2016.

[6] R. L. Burton and P. J. Turchi, "Pulsed plasma thruster," *J. Propul. Power*, vol. 14, no. 5, pp. 716–735, 1998.

[7] K. A. Polzin, "Scaling and systems considerations in pulsed inductive plasma thrusters," *IEEE Trans. Plasma Sci.*, vol. 36, no. 5, pp. 2189–2199, 2008.

[8] C. L. Dailey and R. H. Lovberg, "The PIT MkV pulsed inductive thruster," Tech. Rep., NASA CR 191155; TRW Space and Technology Group, Redondo Beach, CA, 1993.

[9] R. H. Lovberg and C. L. Dailey, "A PIT primer," Tech. Rep., RLD Associates, TR 005, Lebanon, PA, 1994.

[10] K. A. Polzin, T. E. Markusic, B. J. Stanojev, A. DeHoyos, and B. Spaun, "Thrust stand for electric propulsion performance evaluation," *Rev. Sci. Instrum.*, vol. 77, no. 10, p. 105108, 2006.

[11] M. L. R. Walker, A. L. Victor, R. R. Hofer, and A. D. Gallimore, "Effect of backpressure on ion current density measurements in hall thruster plumes," *J. Propul. Power*, vol. 21, no. 3, pp. 408–415, 2005.

[12] E. A. Cubbin, J. K. Ziemer, E. Y. Choueiri, and R. G. Jahn, "Pulsed thrust measurements using laser interferometry," *Rev. Sci. Instrum.*, vol. 68, no. 6, pp. 2339–2346, 1997.

[13] K. A. Polzin, A. K. Martin, J. M. Little, C. L. Promislow, B. A. Jorns, and J. M. Woods, "State-of-the-art and advancement paths for inductive pulsed plasma thrusters," *Aerospace*, vol. 7, no. 105, pp. 1–67, 2020.

[14] K. A. Polzin, "Pulse inductive thruster using martian atmosphere as propellant," Tech. Rep., NASA Marshall Space Flight Center, Propulsion Systems Department, 4344, 2012.

[15] K. A. Polzin, "Comprehensive review of planar pulsed inductive plasma thruster research and technology," *J. Propul. Power*, vol. 27, no. 3, pp. 513–531, 2011.

[16] C. L. Dailey, "Pulsed electromagnetic thruster," Tech. Rep., TRW Systems Group, AFRPL-TR-71-107, Redondo Beach, CA, 1971.

[17] C. L. Dailey and R. H. Lovberg, "Current sheet structure in an inductive-impulsive plasma accelerator," *AIAA Journal*, vol. 10, no. 2, pp. 125–129, 1972.

[18] C. L. Dailey and R. H. Lovberg, "Large diameter inductive plasma thrusters," in *Proceedings of 14th AIAA/DGLR International Electric Propulsion Conference, Princeton, NJ.*, IEPC-1979-2093, 1979.

[19] I. Hrbud, M. LaPointe, R. Vondra, C. L. Dailey, and R. H. Lovberg, "Status of pulsed inductive thruster research," in *Proceedings of American Institute of Physics*, vol. 608, pp. 627–632, 2002.

[20] C. L. Dailey and H. A. Davis, "Pulsed plasma propulsion technology," Tech. Rep., TRW Systems Group, AFRPL-TR-73-81, Redondo Beach, CA, 1973.

[21] D. E. Kirtley, A. D. Gallimore, J. Haas, and M. Reilly, "High density magnetized toroid formation and translation with XOCOT: An annular field reversed configuration plasma concept," Tech. Rep., Air Force Research Laboratory, AFRL-PR-ED-TP-2007-387, 2007.

[22] E. Y. Choueiri and K. A. Polzin, "Faraday acceleration with radio-frequency assisted discharge," *J. Propul. Power*, vol. 22, no. 3, pp. 611–619, 2006.

[23] K. A. Polzin, *Faraday Accelerator with Radio-Frequency Assisted Discharge (FARAD).* PhD Thesis, 3147-T, Department of Mechanical and Aerospace Engineering, Princeton Univ., Princeton, NJ, 2006.

[24] V. Josephson, "Production of high velocity shocks," *J. Appl. Phys.*, vol. 29, no. 1, pp. 30–32, 1958.

[25] R. C. Cruddace and M. Hill, "Mechanism of plasma acceleration in a conical theta-pinch gun," Tech. Rep., Culham Laboratory, CLM-M52, 1966.

[26] C. S. Niemela and D. E. Kirtley, "Initial results on an annular field reversed configuration plasma translation experiment," Tech. Rep., Air Force Research Laboratory, AFRL-RZ-ED-TP-2008-489, 2008.

[27] T. Raines, "Propellant mass scaling and decoupling and improved plasma coupling in a pulsed inductive thruster," Master's thesis, School for Engineering of Matter, Transport, and Energy, Arizona State Univ., Tempe, AZ, 2018.

[28] V. Josephson and R. W. Hales, "Parametric study of the conical shock tube," *Phys. of Fluids*, vol. 4, no. 3, pp. 373–379, 1961.

[29] P. J. Fimognari, J. T. Cassibry, and K. E. Ims, "Effects of pre-ionization and bias field on plasmoid formation and acceleration," in *Proceedings of 43rd AIAA/ASME/SAE/ASEE Joint Propulsion Conference and Exhibition, Cincinnati, OH.*, AIAA-2007-5262, 2007.

[30] R. H. Eskridge, P. J. Fimognari, A. K. Martin, and M. H. Lee, "Design and construction of the PT-1 prototype plasmoid thruster," *AIP Conf. Proc.*, vol. 813, pp. 474–483, 2006.

[31] C. L. Dailey, "Plasma properties in an inductive pulsed plasma accelerator," in *Proceedings of 6th Biennial AIAA/Northwestern University Gas Dynamics Symposium, Evanston, IL.*, AIAA-1965-0637, 1965.

[32] R. H. Lovberg, "Investigation of current sheet microstructure," *AIAA Journal*, vol. 4, no. 7, pp. 1215–1222, 1966.

[33] C. L. Dailey, "Investigation of plasma rotation in a pulsed inductive accelerator," in *Proceedings of AIAA 6th Annual Aerospace Sciences Meeting, New York, NY.*, AIAA-1968-0086, 1968.

[34] C. L. Dailey, "Investigation of plasma rotation in a pulsed inductive accelerator," *AIAA Journal*, vol. 7, no. 1, pp. 13–19, 1969.

[35] R. H. Lovberg and C. L. Dailey, "Current sheet development in a pulsed inductive accelerator," in *Proceedings of 25th AIAA/SAE/ASME/ASEE Joint Propulsion Conference, Monterey, CA.*, AIAA-1989-2266, 1989.

[36] C. L. Dailey and R. H. Lovberg, "PIT clamped discharge evolution," Tech. Rep., TRW Space and Technology Group, AFOSR-TR-89-0130, Redondo Beach, CA, 1988.

[37] R. H. Lovberg and C. L. Dailey, "Large inductive thruster performance measurement," *AIAA Journal*, vol. 20, no. 7, pp. 971–977, 1982.

[38] A. K. Hallock, A. K. Martin, K. A. Polzin, A. C. Kimberlin, and R. H. Eskridge, "Single- and repetitive-pulse conical theta-pinch inductive pulsed plasma thruster performance," *IEEE Trans. Plasma Sci.*, vol. 43, no. 1, pp. 433–443, 2015.

[39] A. K. Martin, "Performance scaling of inductive pulsed plasma thrusters with coil angle and pulse rate," *J. Appl. Phys.*, vol. 49, no. 025201, 2016.

[40] K. A. Polzin, M. F. Rose, R. Miller, S. Best, T. Owens, and J. Dankanich, "Design of a low-energy farad thruster," in *Proceedings of 43rd AIAA/ASME/SAE/ASEE Joint Propulsion Conference and Exhibition, Cincinnati, OH.*, AIAA-2007-5257, 2007.

[41] A. K. Martin, A. Dominguez, R. H. Eskridge, and K. A. Polzin, "Design and testing of a small inductive pulsed plasma thruster," in *Proceedings of 34th International Electric Propulsion Conference, Hyogo-Kobe, Japan*, IEPC-2015-50, 2015.

[42] A. K. Martin and R. H. Eskridge, "Electrical coupling efficiency of inductive plasma accelerators," *J. Appl. Phys.*, vol. 38, no. 23, pp. 4168–4179, 2005.

[43] K. A. Polzin, K. Sankaran, A. G. Ritchie, and J. P. Reneau, "Inductive pulsed plasma thruster model with time-evolution of energy and state properties," *J. Appl. Phys.*, vol. 46, no. 475201, 2013.

[44] K. A. Polzin and E. Y. Choueiri, "Performance optimization criteria for pulsed inductive plasma acceleration," *IEEE Trans. Plasma Sci.*, vol. 34, no. 3, pp. 945–954, 2006.

[45] J. H. Poylio, D. Russell, W. Goldstein, B. Jackson, R. H. Lovberg, and C. L. Dailey, "Pulsed inductive thruster: Flighscale proof of concept demonstrator," in *Proceedings of 40th AIAA/ASME/SAE/ASEE Joint Propulsion Conference and Exhibition, Fort Lauderdale, FL.*, AIAA-2004-3640, 2004.

[46] D. Russell, J. H. Poylio, W. Goldstein, B. Jackson, R. H. Lovberg, and C. L. Dailey, "The PIT mark VI pulsed inductive thruster," in *Proceedings of Space 2004 Conference, San Diego, CA.*, AIAA-2004-6054 2004.

[47] R. H. Frisbee and I. G. Mikellides, "The nuclear electric pulsed inductive thruster (NuPIT): Mission analysis for prometheus," in *Proceedings of 41st AIAA/SAE/ASME/ASEE Joint Propulsion Conference, Tucson, AZ.*, AIAA-2005-3892, 2005.

[48] C. L. Promislow and J. M. Little, "Operation and performance of a power processing unit for inductive pulsed plasma thrusters operating at high repetition rates," in review, 2022.

[49] J. D. Frieman, J. A. Walker, M. L. R. Walker, V. Khayms, and D. Q. King, "Electrical facility effects on hall thruster cathode coupling: Performance and plume properties," *J. Propul. Power*, vol. 32, no. 1, pp. 251–264, 2015.

[50] M. P. Byrne and B. A. Jorns, "Data-driven models for the effects of background pressure on the operation of hall thrusters," in *Proceedings of 36th International Electric Propulsion Conference, Vienna, Austria.*, IEPC-2019-630, 2019.

[51] M. L. R. Walker, A. D. Gallimore, C. Cai, and I. D. Boyd, "Pressure map of a facility as a function of flow rate to study facility effects," in *Proceedings of 38th AIAA/ASME/SAE/ASEE Joint Propulsion Conference & Exhibit, Indianapolis, IN.*, AIAA-2002-3815, 2002.

[52] K. A. Polzin and J. P. Reneau, "Effect of conductive walls on the performance of a pulsed inductive thruster," *IEEE Trans. Plasma Sci.*, vol. 37, no. 2, pp. 359–365, 2009.

[53] P. G. Mikellides and C. Neilly, "Modeling and performance analysis of the pulsed inductive thruster," *J. Propul. Power*, vol. 23, no. 1, pp. 51–58, 2007.

[54] D. W. Guo, M. S. Cheng, X. Yang, X. K. Li, and B. X. Che, "Development and validation of a multiphysics coupling model of the pulsed electromagnetic inductive valve for planar pulsed inductive plasma thruster," *IEEE Trans. Plasma Sci.*, vol. 47, no. 1, pp. 587–596, 2019.

[55] Y. Cheng and G. Xia, "Numerical investigation of flow properties of the pulsed inductive thruster considering plasma electrical characteristics," *J. Aerospace Engineering*, vol. 233, no. 11, pp. 4106–4114, 2018.

[56] Y. Cheng and G. Xia, "Simulation of plasma behavior for medium propellant mass and pulsed energy of small scale pulsed inductive thruster," *Chin. J. Aero.*, vol. 33, no. 1, pp. 176–190, 2020.

[57] B. X. Che, M. S. Cheng, X. K. Li, and D. W. Guo, "Physical mechanisms and factors influencing inductive pulsed plasma thruster performance: A numerical study using an extended magnetohydrodynamic model," *J. Appl. Phys.*, vol. 51, no. 36, p. 365202, 2018.

[58] J. M. Little, G. I. McCulloh, and C. W. Marsh, "Ionization and current sheet formation in inductive pulsed plasma thrusters," in review, 2022.

[59] M. A. Lieberman and A. J. Lichtenberg, *Principles of Plasma Discharges and Materials Processing*. John Wiley and Sons, Inc., 2005.

[60] S. C. Brown, *Basic Data of Plasma Physics*. New York, NY.: American Institute of Physics, 1994.

[61] D. Rapp and P. Englander-Golden, "Total cross sections for ionization and attachment in gases by electron impact," *J. Chem. Phys.*, vol. 43, no. 1464, 1965.

[62] J. S. Miller, S. H. Pullins, D. Lavandier, Y. H. Chiu, and R. A. Dressler, "Xenon charge exchange cross section for electrostatic thruster models," *J. Appl. Phys.*, vol. 91, no. 3, 2002.

[63] D. Rapp and W. E. Francis, "Charge exchange between gaseous ions and atoms," *J. Chem. Phys.*, vol. 37, no. 1, pp. 2631–2645, 1962.

[64] J. S. Halekas, D. A. Brain, S. Ruhunusiri, J. P. McFadden, D. L. Mitchell, C. Mazelle, J. E. P. Connerney, Y. Harada, T. Hara, J. R. Espley, G. A. DiBraccio, and B. M. Jakosky, "Plasma clouds and snowplows: Bulk plasma escape from Mars observed by MAVEN," *Geophys. Research Letters*, vol. 43, no. 4, pp. 1426–1434, 2016.

[65] V. S. Semenov, N. N. Volkonskaya, and H. K. Biernat, "Effect of a snow plot in bursty magnetic reconnection," *Phys. Plasmas*, vol. 5, no. 9, p. 3242, 1998.

[66] C. L. Kelly and J. M. Little, "Neutral flow interaction with a magnetic dipole plasma II. Global model," *Phys. Plasmas*, vol. 27, no. 113511, 2020.

[67] A. V. Phelps, "Cross sections and swarm coefficients for nitrogen ions and neutrals in N2 and argon: Ions and neutrals in Ar for energies from 0.1 eV to 10 keV," *J. Phys. Chem. Ref. Data*, vol. 20, no. 3, pp. 557–573, 1991.

[68] M. Suzuki, T. Taniguchi, N. Yoshimura, and H. Tagashira, "Momentum transfer cross section of xenon deduced from electron drift velocity data," *J. Appl. Phys.*, vol. 25, pp. 50–56, 1992.

[69] K. A. Polzin, C. S. Hill, P. J. Turchi, R. L. Burton, S. Messer, R. H. Lovberg, and A. K. Hallock, "Recommended practice for use of inductive magnetic field probes in electric propulsion testing," *J. Propul. Power*, vol. 33, no. 3, pp. 659–667, 2017.

[70] X. K. Li, B. X. Che, M. S. Cheng, D. W. Guo, M. G. Wang, and Y. T. Yang, "Investigation on plasma structure evolution and discharge characteristics of a single-stage planar-pulsed-inductive accelerator under ambient fill condition," *Chin. Phys. B*, vol. 29, no. 11, p. 115201, 2020.

[71] K. A. Polzin, A. D. Sivak, and J. V. Balla, "Effect of an additional, parallel capacitor on pulsed inductive plasma accelerator performance," in *Proceedings of 32nd International Electric Propulsion Conference, Wiesbaden, Germany.*, IEPC-2011-160, 2011.

[72] K. Takahashi, T. Lafleur, C. Charles, P. Alexander, and R. W. Boswell, "Electron diamagnetic effect on axial force in an expanding plasma: Experiments and theory," *Phys. Rev. Lett.*, vol. 107, no. 23, p. 235001, 2011.

Appendix A

MODEL CODE AND IMAGE PROCESSING SCRIPTS

Code for the 1D single-pulse and multi-pulse IPPT models is developed in Wolfram Mathematica versions 12.1 and 12.2. ICCD image processing scripts are written in Python. Both bodies of software can be found on the author's personal GitHub in the following repositories:

- `https://github.com/mccullohg/IPPT-Model`
- `https://github.com/mccullohg/HiPeR-PIT-ICCD-Processing`

Other developers include Professor Justin Little and PhD candidate Curtis Promislow of the University of Washington Space Propulsion and Advanced Concepts Engineering (SPACE) Lab. A brief description and set of instructions can be found in the header of most scripts. At the time of this thesis publication, development of a working IPPT model in Python for faster runtime is underway. Common errors include automatic step size adjustments made by the built-in Mathematica subfunctions and occasional diverging solutions to the inter-pulse model for poorly chosen input conditions.

Appendix B
ANCILLARY THEORETICAL RESULTS

Here, we present time-dependent solutions to our 1D PIT model that support the analysis given in the main body of the thesis. This includes state properties, timescales critical to energy dynamics, loss modes, and performance metrics. We begin by presenting additional information relevant to the backfill study in Chapter 4, then give propellant performance scaling for the baseline conditions of the single- and multi-pulse models.

Additional Time-dependent Backfill Effects

Information regarding the evolution of the fast neutral population and the effect of neutral slip is absent from the original backfill comparison since it is largely captured by the energy partitioning diagram given by Fig. 4.4. We give fast neutral velocity and density as well as slipped neutral momentum and kinetic energy in Fig. B.1 for both the backfill condition and steady-state injection.

Panel (a) shows us that v_f closely agrees with v_s by depicting model separation at $t/\tau_{LC} = 0.125$ and a near twofold difference in deceleration. This indicates that the fast neutrals see the same collisional drag force as the plasma sheet. The fast neutral density functions in (b), however, depict a much greater degree of model separation as predicted by Fig. 4.4. The steady-state solution exhibits asymptotic fast neutral excitation, leveling off at $n_f \approx 10^{20}$ m^{-3}. This is about 15% the final value of n_s at these conditions, as given by Fig. 4.1(d). Thruster operation in a backfill proffers the entrainment of nearly eight times the quantity of fast neutrals due to charge exchanges further from the coil face.

Neutral slip agrees across the two background neutral conditions, but represents a small effect relative to other time-varying processes in the plasma. All slipped neutrals appear

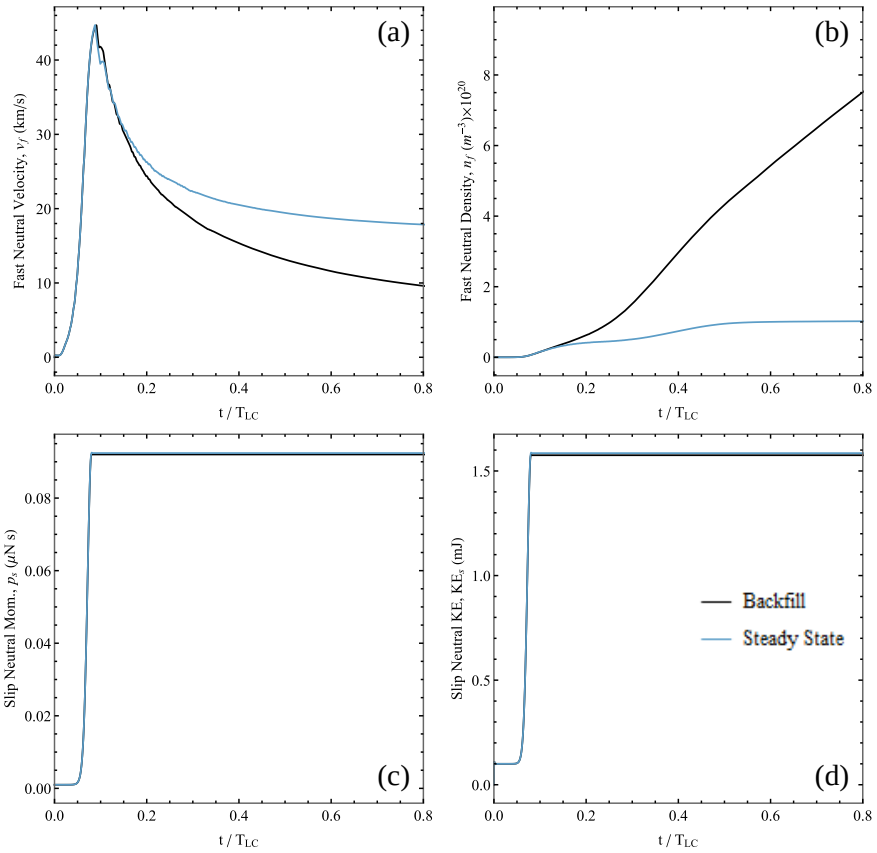

Figure B.1: Time-dependence of fast and slipped neutral population state variables under backfill and steady-state ambient neutral gas conditions. Data is generated from the baseline input conditions listed in Table 3.1 and shows the same solutions as Section 4.2.

early within the pulse at $t/\tau_{LC} \approx 0.075$, generating only ~ 0.09 μNs of momentum and ~ 1.6 mJ of kinetic energy. This is depicted as a near nonexistent energy mode in Fig. 4.4.

The electromagnetic transparency of the sheet across both conditions is given by Fig. 4.3(a), but we provide the skin depth underlying this parameter in Fig. B.2. As seen, $\delta_{s,0} \gg w_{s,0}$ due to high initial plasma resistivity from low pre-ionization. The skin depth drops significantly over the formation phase of the pulse before growing once again and depicting a broad separation between the backfill and steady-state solutions. These trends are mirrored by Θ_e to show that the AC fields of the coil can penetrate deeper into the backfill

sheet across the deceleration phase.

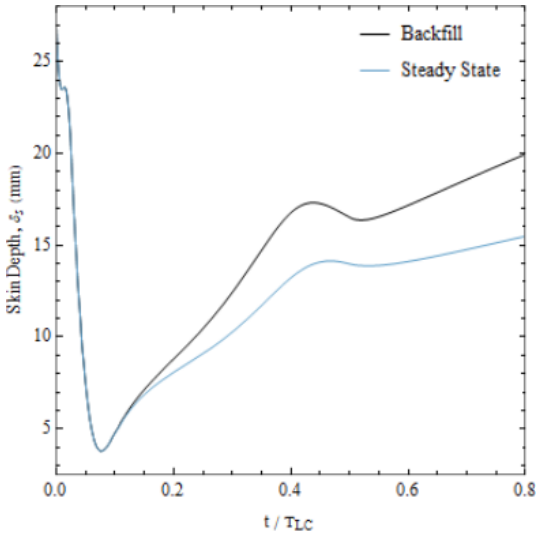

Figure B.2: Time-dependence of finite skin depth under backfill and steady-state ambient neutral gas conditions. Data is generated from the baseline input conditions listed in Table 3.1 and shows the same solution as Section 4.2.

We now proceed with a cursory formulation of three dimensionless parameters that indicate key energetic timescales over the course of a pulse. These aim to inform the partitioning study in Section 4.3 by isolating variables that underscore various processes, but the results are less insightful than those given by the transparency parameters in Fig. 4.3. First, we define an ionization timescale in terms of the angular frequency of the incident EM fields as

$$\Pi_{ion} = n_s S_{ion}/\omega. \tag{B.1}$$

Next, we can define a subsequent ionization heating fraction due to the thermal energy contained in the electron population as

$$\Pi_{hf} = n_s w_s S_{ion}/v_s. \tag{B.2}$$

Lastly, we propose a charge-exchange parameter that scales with the collisional cross section

according to

$$\Pi_{cx} = n_s w_s \sigma_{cx}. \tag{B.3}$$

Ideally, σ_{cx} is given as a function of T_e, so this parameter could be significantly more informative for a more robust propellant model. Fig. B.3 shows the time-evolved values of our proposed nondimensionalized parameters to reinforce the results and analysis in Chapter 4.

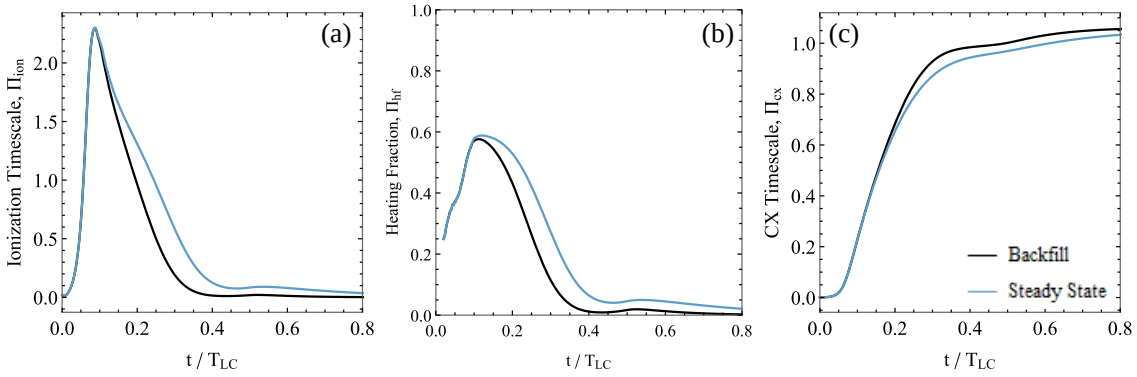

Figure B.3: Time-dependence of dimensionless parameters critical to heating and entrainment timescales under backfill and steady-state ambient neutral gas conditions. Data is generated from the baseline input conditions listed in Table 3.1 and shows the same solutions as Section 4.2.

Panel (a) tells us that the highest rate of ionization due to inductive energy transferred from the drive coil to the plasma occurs at $t/\tau_{LC} \approx 0.1$, after which both solutions see a gradual decay. This intuitively aligns with the principles of efficient PIT operation since the influence of the coil is strongest within the coupling region. Π_{ion} indicates that steady injection offers a higher rate of ionization than static neutral fill, which supports the findings of Fig.4.3(b). As a consequence, Π_{hf} shows that the steady-state equilibrium experiences a higher heating fraction due to ionization reactions than the backfill system, but the latter compensates its mass entrainment by experiencing greater CX collisions.

Lastly, we attempt to quantify the slip and ionization loss mechanisms, or at least locate

the critical moments along the time-development of sheet dynamics that maximize inefficiencies. We define the slip loss via the fast neutral population as

$$L_{slip} = n_f \Delta v_{sf} H(\Delta v_{sf}) \tag{B.4}$$

such that only the excited, mass-carrying particles contribute to de-entrainment. We define the ionization loss mechanism according to the rate at which reaction energy is emparted to the fast neutral population, given by

$$L_{ion} = n_f n_s w_s S_{ion}. \tag{B.5}$$

The units attached to both of these metrics indicate an area for improvement, as some dimensionless quantity per area per second offers little utility. Still, Fig. B.4 gives the time-dependent losses of slip and ionization, respectively.

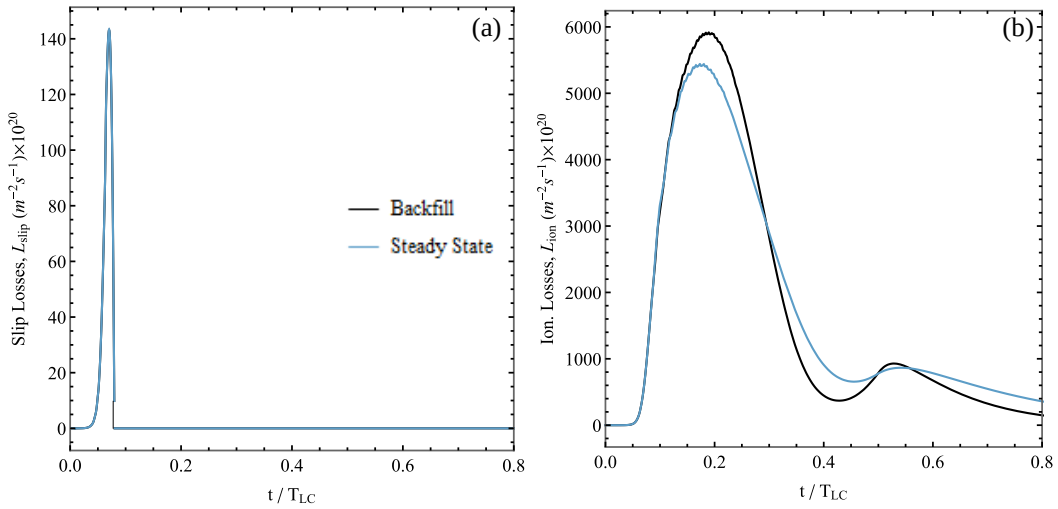

Figure B.4: Time-dependence of neutral slip and ionization loss modes under backfill and steady-state ambient neutral gas conditions. Data is generated from the baseline input conditions listed in Table 3.1 and shows the same solutions as Section 4.2.

Panel (a) indicates what we already know from Fig. B.1(c)-(d), which is that neutral slip is

an intense, transient process at $t/\tau_{LC} \approx 0.075$ for the given conditions. Fig. B.4(b), however, is a bit more informative in that it depicts a greater portion of ionization energy lost to the fast neutrals in a backfill, as well as greater loss volatility over the pulse duration. These metrics are mainly presented as grounds for future adjustment and evaluation throughout model development.

Propellant Performance Scaling

We give time-dependent propellant comparisons across the most informative state properties of the model in Sections 2.7 and 3.4 for single- and multi-pulse operation, respectively. In general, we found that reporting the performance metrics has been less critical to our study than the contingent plasma dynamics, as the nature of the backfill comparison exaggerates the mass bit by integrating the background neutral distribution across the simulation boundary.

Fig. B.5 bypasses this issue since the single-pulse model established in Chapter 2 uses the exponential form given by Eq. (2.58) to simulate pulsed gas injection. We observe the consequences of better mass utilization scaling and electromagnetic impermeability for xenon propellant in panels (c) and (d), which exhibit higher η_m and η_e for the conditions listed in Table 2.2. This results in a substantially higher recapture efficiency by a margin of almost 50%. Xenon also provides a higher I_{sp} for the same circuit architecture and coil geometry, but builds to its final asymptotic value more gradually in time. This is because, as Fig. 2.9 tells us, argon builds a much higher sheet velocity at the expense of lower plasma density.

The multi-pulse code processes higher values of m_{bit} in steady state due to the evolution of neutral density shown in Fig. 3.1. We have already observed the time-dependent performance metrics of argon across the first and final pulses in Fig. 3.5, but we now compare the same results to the steady-state values for xenon in Fig. B.6. Here, we find that the gap between propellants has grown, as mass utilization and electrical efficiency both suffer dramatically for argon, even at high pulse rates. Since xenon forms better current sheets across a single discharge, the performance gap compounds over time. The most notable difference

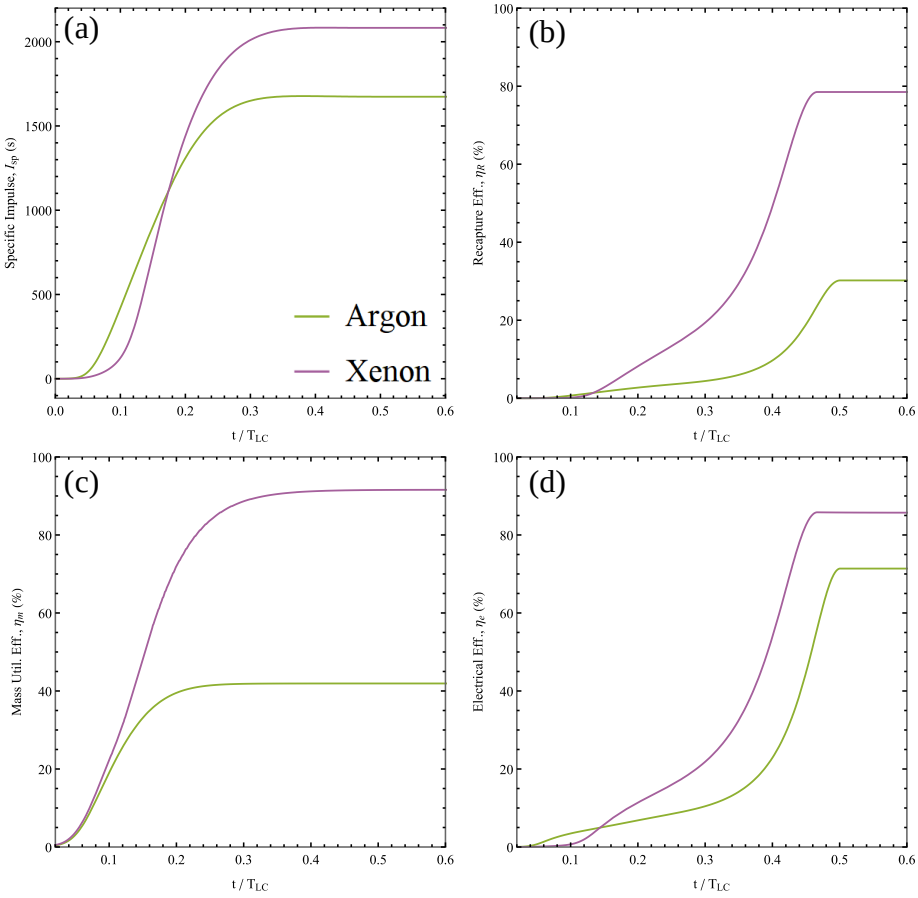

Figure B.5: Time-dependence of performance metrics for argon and xenon propellant models for single-pulse operation with inductive recapture. Data is generated from the input conditions listed in Table 2.2.

is apparent in η_e, as significantly improved impermeability to EM fields drives better kinetic energy transfer. This is communicated by Fig. 3.8(f) in Chapter 3.

The given input regime results in significantly higher specific impulse, suggesting that the use of xenon propellant could potentially be a technology-enabling design choice for future low-discharge-energy PITs. With respect to the backfill study, we conclude in Chapter 4 that the core findings of our comparison are consistent across the two propellant models. This is because $n_n(z,t)$ is the differentiating factor, so xenon also experiences similar rates

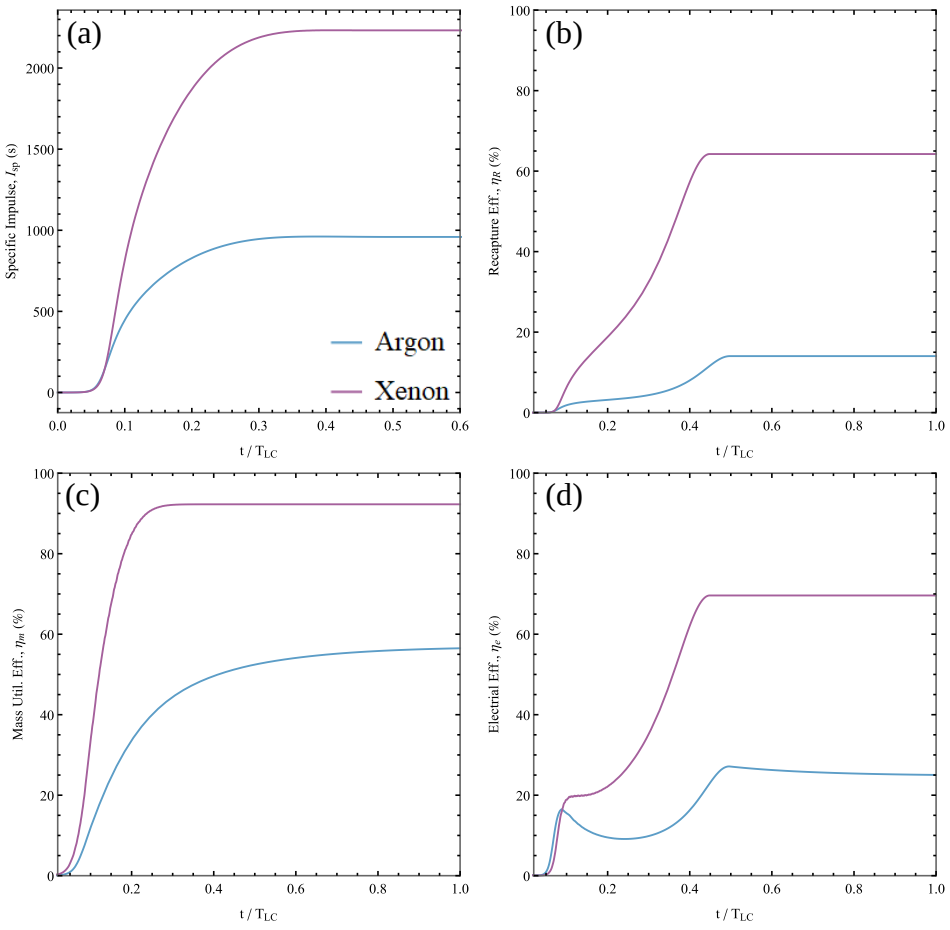

Figure B.6: Time-dependence of performance metrics for argon and xenon propellant models for multi-pulse operation using inductive recapture. Data is generated from the input conditions listed in Table 3.1.

of dissimilarity across the entrainment mechanisms and sheet dynamics of the steady-state simulation.

Appendix C

ADDITIONAL ICCD IMAGES AND DATA

For a thorough analysis of visual data from the preliminary HiPeR-PIT experiment and comparisons drawn between measured sheet parameters and the 1D PIT model, see Chapter 7. In this appendix, we provide additional ICCD data gathered across a lower voltage sweep for a pulse energy of 4 J. These results allow for a brief, qualitative comparison against those given in Figs. 7.1 and 7.2 to comment on the influence of V_0 and the varied timescales of subsequent sheet dynamics.

Fig. C.1 depicts the representative image frames for $V_0 = 2$ kV and $P_0 = 2$ mTorr across a shorter temporal span than Fig. 7.1. We still find similar phases across the evolution of the pulse, where the top row captures pre-ionization and formation, axial propagation and sheet compression occurs from $9.2 - 12.7$ μs, and a secondary sheet forms at 13.2 μs. The secondary sheet then exhibits significant snowplow losses resulting in the diffuse cloud of ionized gas in the final frame.

We find that a lower input voltage results in greater non-uniformity across the radial profile of the sheet, but also that the plasma requires less time to form and accelerate. This is in accordance with Polzin's current rise rate requirement and the proposed formation parameter because a decrease in V_0 for constant L_c will lower the amount of energy deposited in the electron population. Poorer formation reduces the residence time of the secondary, resulting in poorer overall coupling. This is evident in the lower intensity values given by Fig. C.2 relative to the 3-kV data set. Since these results reflect a slight decrease in backpressure as well, the analysis of Fig. 3.6 applies as well.

The intensity data captures asymmetric activity within the plasma sheet by giving much higher values in the northern region of each frame along $\hat{r}$. Anomalous coupling is especially

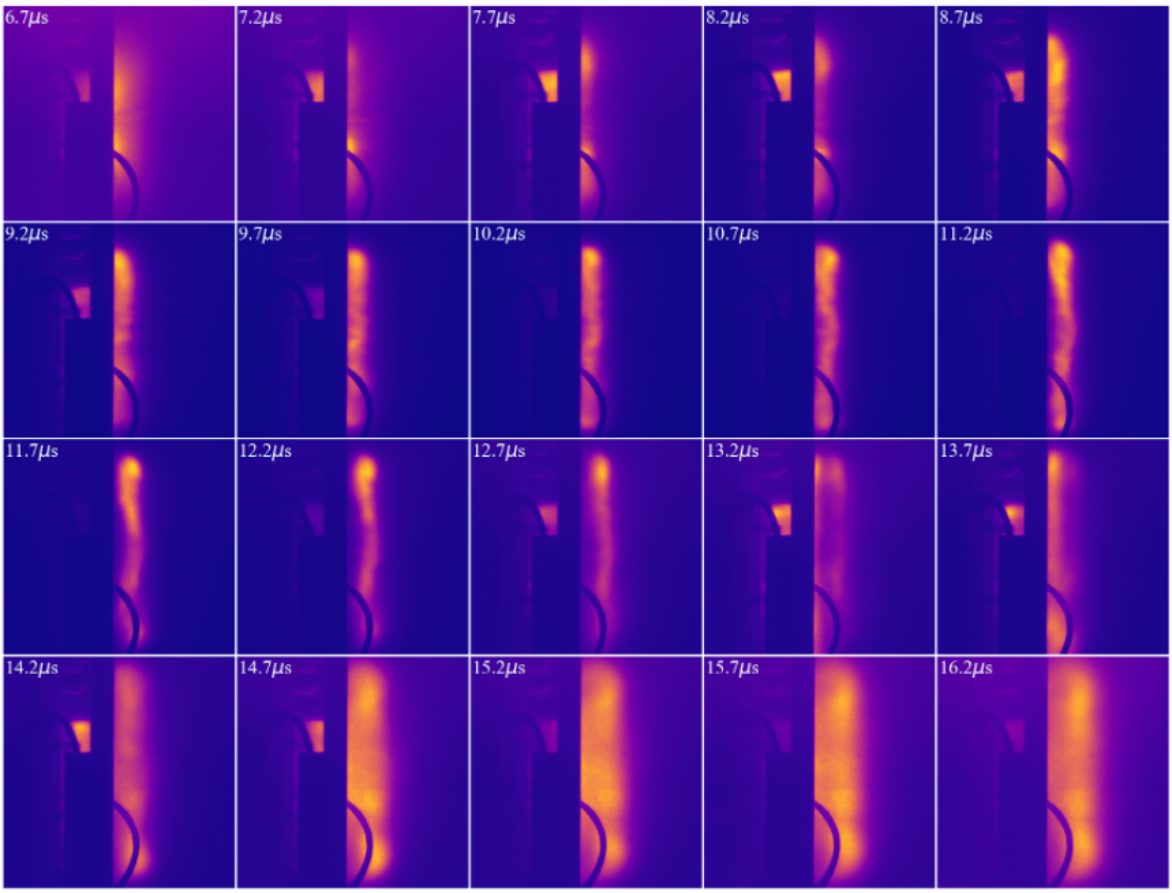

Figure C.1: Representative image frames of experimental plasma sheets at discrete time increments during the first two half-cycles of capacitor discharge for $V_0 = 2$ kV, $P_0 = 2$ mTorr. Fewer frames are shown than in Fig. 7.1 due to fewer sampled plasma shots.

evident at 11.2 μs, where Fig. C.2 gives a near threefold factor of separation between the peak intensity value and the floor of the radial spread. We note that there is less noise associated with the brightest frames. Intensity along $\hat{z}$ dissipates much faster than in Fig. 7.2, reinforcing the notion of poorer overall coupling and lower ultimate plasma density.

The secondary sheet forms at roughly the same point in time past signal generation and capacitor discharge ($\sim$ 13.7 μs), which intuitively follows from equal LC-periods. The ambient pressure is close enough to the condition given in Chapter 7 that steady gas injection

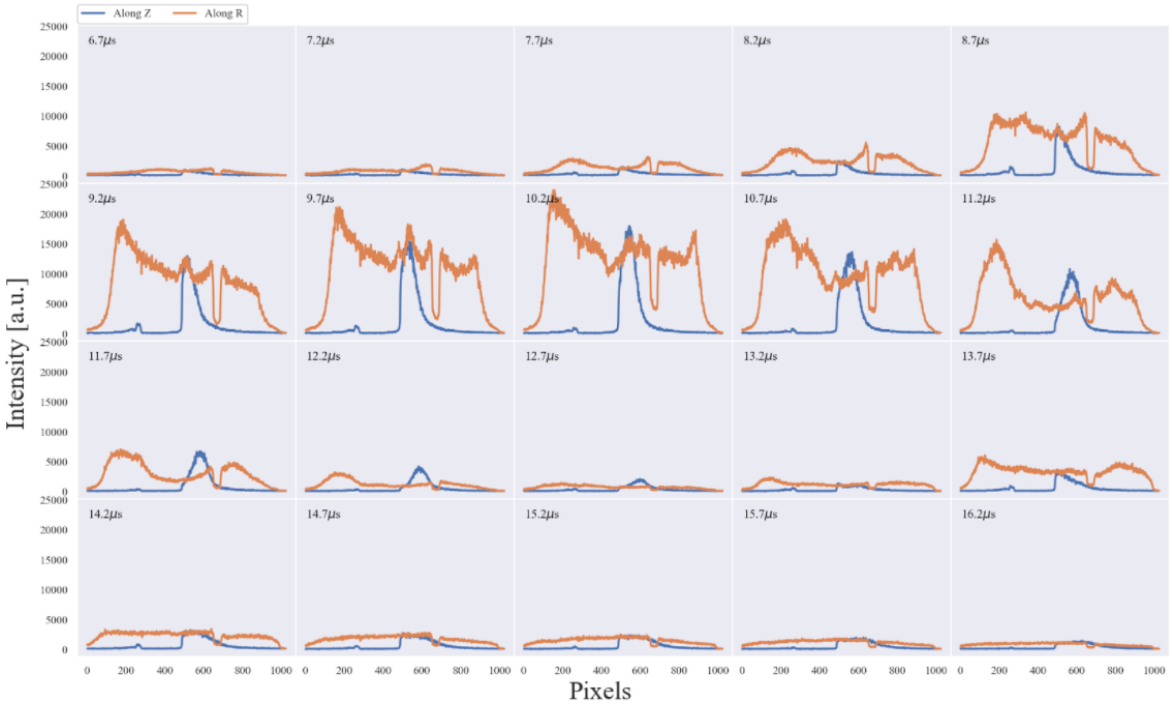

Figure C.2: Relative intensities along $\hat{z}$ and $\hat{r}$ collected by the PI-MAX 4 ICCD camera corresponding to frames from Fig. C.1 for $V_0 = 2$ kV, $P_0 = 2$ mTorr. Fewer frames are shown than in Fig. 7.2 due to fewer sampled plasma shots.

still offers sufficient neutral density at the coil face for the second half-cycle to ionize the remaining propellant. Reduction of P_0 will decrease the likelihood of this behavior, but will also result in poorer sheet formation past the critical voltage threshold, $V_0^* \approx 2.5$ kV, per Fig. 4.6.